Quantum gases in optical lattices

Sylvain Nascimbene

M2 ICFP, course *Ultracold atoms* - École Normale Supérieure

These lecture notes accompany the part of the Master 2 course *Ultracold atoms* (École Normale Supérieure, Paris) devoted to quantum gases in optical lattices.

Contents

1 Introduction: simulating electrons in a crystal with atoms in optical lattices **4**
1.1 Electrons in a crystal and atoms in an optical lattice 4
1.2 New physics in lattice structures 6
1.3 Outline of the notes 8

2 Band structure and dynamics in optical lattices **8**
2.1 Band structure in one dimension 9
2.1.1 Optical lattice potential 9
2.1.2 Bloch theorem 11
2.1.3 Free-particle spectrum in the reduced zone scheme 11
2.1.4 Solving the Schrödinger equation: the central equation 12
2.1.5 Band structures 13
2.1.6 Bloch states 14
2.2 Dynamics of a particle in an optical lattice 15
2.2.1 Kapitza-Dirac diffraction 15
2.2.2 Loading of the ground band: adiabaticity criterion 16
2.2.3 Time of flight versus band mapping 18
2.2.4 Bragg diffraction 20
2.2.5 Propagation of a wave packet: group velocity and effective mass 22
2.2.6 Action of an external force 24
2.2.7 Bloch oscillations 25
2.2.8 Landau-Zener transitions 29
2.3 Wannier functions and tight-binding limit 31
2.3.1 Wannier functions 31
2.3.2 Hamiltonian in the Wannier basis 32
2.3.3 Tight-binding limit 32

3 Complex lattices and topological bands **34**
3.1 One-dimensional superlattices and the SSH model 34
3.1.1 Two-color superlattice potential 35
3.1.2 Band structure of the SSH model 37
3.1.3 Zak phase and band topology 39
3.1.4 Measuring the Zak phase 40
3.1.5 Topological edge modes 41
3.2 Two-dimensional lattices: Dirac points and quantum Hall bands 43
3.2.1 Graphene-like honeycomb lattice 43
3.2.2 Probing Dirac points using Bloch oscillations 44
3.2.3 Optical lattices with complex tunneling amplitudes 46
3.2.4 Hofstadter model and quantum Hall effect 48

4 Superfluid to Mott insulator transition **51**
4.1 The Bose-Hubbard Hamiltonian 52
4.1.1 Tight-binding model with on-site interactions 52
4.1.2 Tunneling versus interaction 53
4.2 Superfluid–Mott insulator phase diagram 55
4.2.1 The atomic limit 55
4.2.2 Qualitative phase diagram 56
4.3 Gutzwiller variational approach 57
4.3.1 Gutzwiller ansatz 58
4.3.2 Gutzwiller energy functional 58
4.3.3 Gutzwiller ground state for unit filling 59
4.3.4 Number fluctuations 59
4.3.5 Particle-hole approximation close to a Mott state 60
4.3.6 Mott phase boundary 62
4.4 Interference experiments 64
4.4.1 Phase coherence from time-of-flight experiments 64
4.4.2 Phase coherence in the superfluid and Mott phases 65
4.4.3 Observation of the transition 66
4.4.4 Particle-hole excitations and residual coherence 68
4.4.5 Finite temperature 69
4.5 Transport experiments: superfluid critical velocity 71
4.6 Mott shell structure 72
4.6.1 Harmonic confinement from Gaussian beams 72
4.6.2 Shell structure of a trapped Mott insulator 73
4.6.3 Single-atom imaging 73
4.6.4 In situ imaging of a Mott insulator 75
4.7 Low-energy excitations 77
4.7.1 In situ observation of particle-hole pairs 77
4.7.2 Higgs amplitude mode 78

5 Fermi-Hubbard model and quantum magnetism **80**
5.1 The Fermi-Hubbard model 80
5.1.1 Hamiltonian 81
5.1.2 Non-interacting fermions: metal and band insulator 81

5.1.3 Overview of the interacting regimes 82
5.2 Attractive Fermi-Hubbard model and BEC-BCS crossover 82
5.2.1 Two-body bound state and mapping to the continuum 83
5.2.2 New features brought by the lattice 84
5.2.3 Phase diagram and experiments 85
5.3 Repulsive Fermi-Hubbard model and Mott insulator 86
5.3.1 Atomic limit and Mott gap 86
5.3.2 Mott insulators with SU(N) symmetry 87
5.4 Quantum magnetism 89
5.4.1 Toy model: superexchange in a double well 90
5.4.2 Probing superexchange interactions 92
5.4.3 Short-range antiferromagnetic correlations 93
5.4.4 Potential shaping to 'remove' entropy 95
5.4.5 Observation of a long-range antiferromagnet 96
5.4.6 Expected phase diagram 98
5.4.7 Quantum magnetism with frustration 98

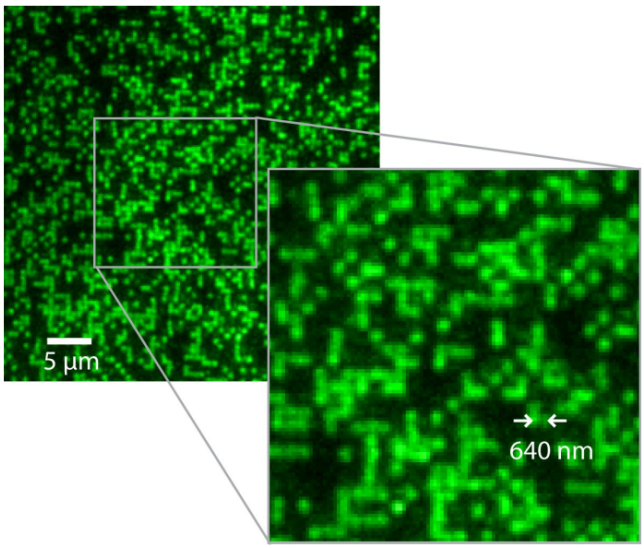


Figure 1: Fluorescence image of ultracold atoms trapped in a two-dimensional square optical lattice, recorded with a quantum gas microscope. Each bright spot is a single atom localized on a lattice site; the zoom shows the lattice spacing of 640 nm. Image from the quantum gas microscope of Ref. [1].

1 Introduction: simulating electrons in a crystal with atoms in optical lattices

These notes cover the part of the M2 ICFP course *Ultracold atoms* devoted to quantum gases in optical lattices, which was taught jointly by Fabrice Gerbier, Raphael Lopes, Sylvain Nascimbene and Aurélien Perrin. In this introductory section, we explain why ultracold atoms trapped in periodic light potentials are a natural platform to study the physics of electrons in solids, we list the new phenomena that a lattice structure brings about, and we present the organization of the notes.

1.1 Electrons in a crystal and atoms in an optical lattice

The electrons of a crystalline solid move in the periodic electrostatic potential created by the ions of the crystal, as sketched in Fig. 2a. The interplay between this periodic potential, the Pauli principle and the Coulomb interaction between electrons determines whether the material is a metal, an insulator, a magnet or a superconductor. Understanding these properties from first principles is one of the central problems of quantum many-body physics. It is notoriously difficult, because the many-body wave function lives in a Hilbert space whose dimension grows exponentially with the number of particles, and because strong correlations often invalidate the mean-field or perturbative approaches.

Following an idea formulated by Feynman [2], one may try to circumvent this difficulty by building a well-controlled quantum system that obeys the same equations as the model of interest, and by measuring its properties directly. Ultracold atoms in optical lattices provide such a *quantum simulator* [3, 4]. As shown in Fig. 2b, the ion lattice is replaced by a periodic potential created by the interference of laser beams, in which

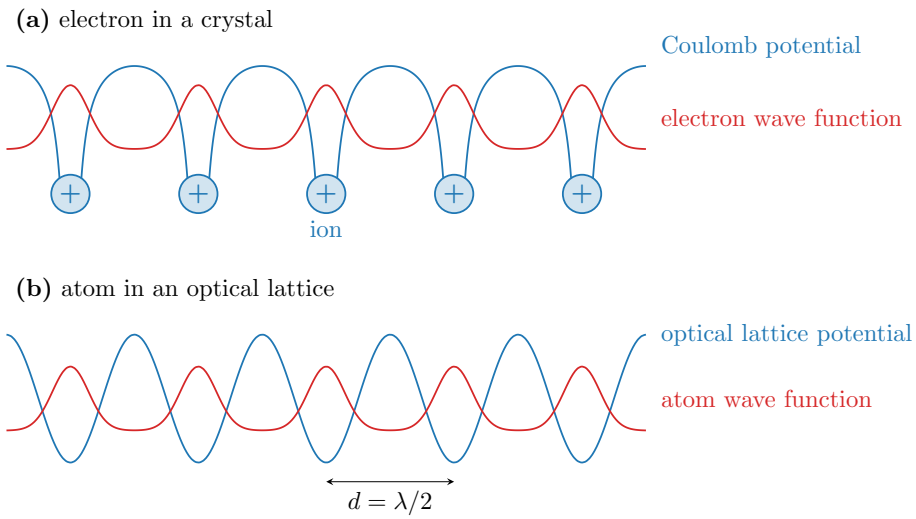


Figure 2: (a) An electron in a crystal moves in the periodic Coulomb potential created by the ions (blue), and its wave function (red) is extended over the whole crystal. (b) An atom in an optical lattice experiences a sinusoidal potential created by a laser standing wave, of period $d = \lambda/2$, and is described by the same physics of Bloch waves.

atoms play the role of the electrons. The optical potential, whose microscopic origin is discussed in section 2, has the following properties:

- The lattice spacing is set by the laser wavelength, typically $d = \lambda/2 \sim 0.5\,\mu$m, instead of a few Ångströms in a solid. The characteristic energy scale, the recoil energy $E_\mathrm{r} = \hbar^2 k_\mathrm{L}^2/2m$ with $k_\mathrm{L} = 2\pi/\lambda$, is of the order of $h\times$ a few kHz, *i.e.* $k_\mathrm{B} \times 100\,$nK. The relevant time scales are thus in the millisecond range, which allows one to follow the dynamics in real time, whereas electron dynamics in solids occurs on femtosecond time scales.

- The lattice is perfectly periodic, without defects, and it does not vibrate (there are no phonons). The lattice depth can be tuned at will, and even varied in time, by changing the laser intensity. The geometry (square, triangular, honeycomb, ...) and the dimensionality are chosen by the laser configuration.

- The atoms can be bosons or fermions, and their interactions, which are short-ranged, can often be tuned using Feshbach resonances.

- New measurement techniques are available, such as time-of-flight imaging, which gives access to the momentum distribution, and quantum gas microscopes, which resolve individual atoms on individual lattice sites (see Fig. 1).

The price to pay is that one must reach extremely low temperatures, in the nanokelvin range, for the atomic system to reach the quantum degenerate regime where the interesting physics takes place.

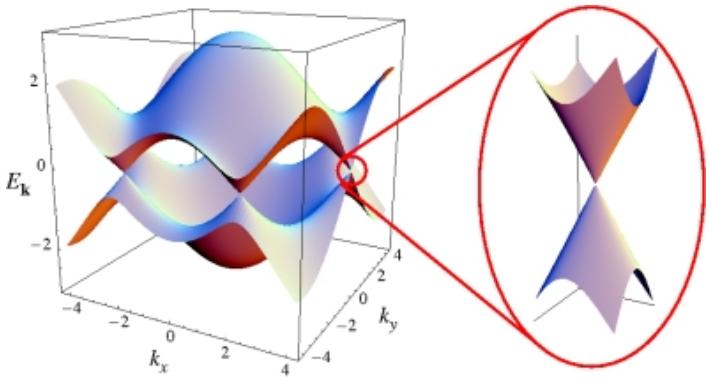


Figure 3: Band structure of graphene in the tight-binding approximation. The two bands touch at the corners of the Brillouin zone, around which the dispersion is conical, as shown in the zoom (Dirac cones). Image taken from Ref. [5].

1.2 New physics in lattice structures

Compared with a gas in free space, the presence of a lattice potential gives rise to a variety of new phenomena, which will be discussed in these notes.

Energy bands. In a periodic potential, the motion of a particle is restricted to energy bands separated by gaps. In a weak lattice, the main effect is a modification of the dispersion relation, which can be described by an effective mass m^*, larger than the bare mass m at the bottom of the band, *i.e.* a reduction of the kinetic energy. In a strong lattice, the particles are localized in the potential wells, and their dynamics reduces to quantum tunneling between neighbouring sites with an amplitude J, see Fig. 4a. One then obtains discrete lattice models, of the type used in condensed matter physics to describe electrons in narrow bands.

Exotic band structures. Lattices with several sites per unit cell give rise to band structures with unusual features. A prominent example is the honeycomb lattice of graphene, whose two lowest bands touch at two points of the Brillouin zone, around which the dispersion relation is linear, as for relativistic massless particles (see Fig. 3) [5]. Complex lattices can also host topological bands, characterized by integer invariants and robust edge states.

Hubbard models and Mott insulators. When interactions are taken into account, the minimal model of particles in a deep lattice is the Hubbard model, which combines tunneling between neighbouring sites, of amplitude J, and an on-site interaction energy U between two particles sitting on the same site (Fig. 4b) [6]. It is the archetype of strongly-correlated models in solid-state physics. When U dominates over J at commensurate filling, the particles get localized, one per site, even if the band is not full: this is a Mott insulator, separated from the superfluid (for bosons) or metallic (for fermions) phase by a quantum phase transition [7].

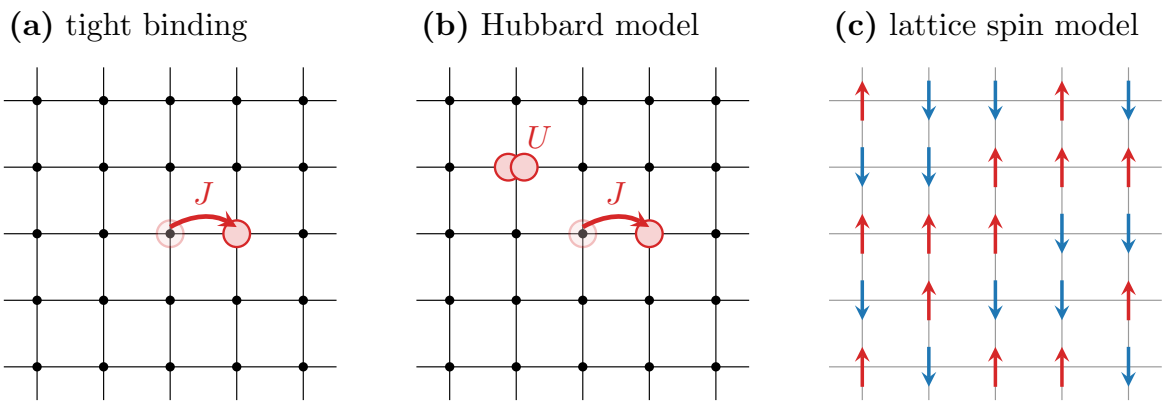


Figure 4: Lattice models studied in these notes. (a) In a deep lattice, the dynamics reduces to tunneling between neighbouring sites with an amplitude J. (b) Hubbard model, in which particles also experience an interaction energy U when they occupy the same site. (c) Lattice spin model, in which the degrees of freedom are spins localized on the lattice sites: what kind of order, if any, do they form at low temperature?

Quantum magnetism. In the Mott insulator of a two-component Fermi gas, each site is occupied by one particle carrying a spin 1/2. The remaining low-energy degrees of freedom are the spins, coupled by a superexchange interaction resulting from virtual tunneling processes. One then obtains lattice spin models, such as the Heisenberg model (Fig. 4c), and one may ask how the spins order at low temperature, and whether exotic states such as spin liquids can occur.

High-temperature superconductivity. The cuprate superconductors consist of copper-oxide planes, in which the electrons are well described by a two-dimensional Fermi-Hubbard model on a square lattice. Their phase diagram (Fig. 5) shows an antiferromagnetic Mott insulator at half filling, and a superconducting dome when holes are added by chemical doping, together with poorly understood phases such as the pseudogap phase [8]. Whether the Fermi-Hubbard model alone captures the mechanism of high-temperature superconductivity remains an open question, which motivates the efforts to realize this model with ultracold fermions.

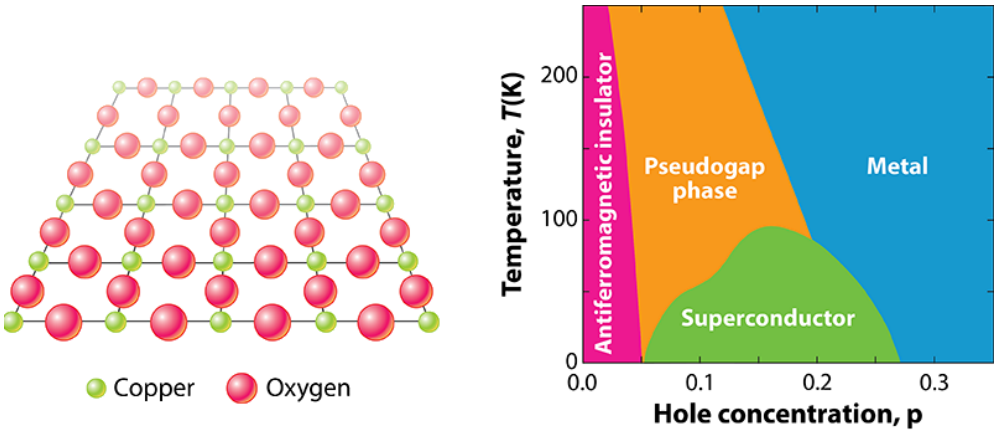


Figure 5: Left: schematic structure of a copper-oxide plane of a cuprate superconductor. Right: schematic phase diagram of hole-doped cuprates as a function of the hole concentration p per copper atom and of temperature, showing the antiferromagnetic Mott insulator, the pseudogap phase, the superconducting dome and the metallic phase (see Ref. [8] for a review).

1.3 Outline of the notes

The notes are organized as follows.

- In section 2, we study the motion of a single particle in a one-dimensional optical lattice. We derive the band structure from the Bloch theorem, and we discuss the dynamics of atoms in a lattice: Kapitza-Dirac and Bragg diffraction, adiabatic loading and band mapping, Bloch oscillations and Landau-Zener transitions. We then introduce the Wannier functions and derive the tight-binding description, including the expression of the tunnel coupling J in deep lattices.

- In section 3, we consider lattices with a more complex structure: the Su-Schrieffer-Heeger model in one dimension, which exhibits topological properties, and two-dimensional lattices such as the honeycomb lattice of graphene and lattices pierced by a magnetic flux, leading to the Hofstadter model and to quantum Hall bands.

- In section 4, we include interactions between bosons and study the Bose-Hubbard model, in particular the quantum phase transition between a superfluid and a Mott insulator, its description within the Gutzwiller approach and its experimental signatures.

- In section 5, we discuss the Fermi-Hubbard model, in its attractive and repulsive versions, the fermionic Mott insulator, and the quantum magnetism that emerges in the strongly-repulsive regime.

2 Band structure and dynamics in optical lattices

In this section we study the quantum motion of a single atom in a one-dimensional optical lattice, neglecting interactions. We first compute the band structure using the

Bloch theorem. We then discuss the dynamics of atoms in a lattice, which provides both experimental tools (diffraction, adiabatic loading, band mapping) and genuinely new phenomena (effective mass, Bloch oscillations, Landau-Zener transitions). We finally introduce the Wannier functions, which form the natural basis to describe deep lattices, and derive the tight-binding model that will be the starting point of the following sections.

2.1 Band structure in one dimension

We first derive the form of the lattice potential, and then solve the Schrödinger equation using the Bloch theorem. This leads to a simple numerical method, the central equation, which we use to compute the band structure for various lattice depths.

2.1.1 Optical lattice potential

Optical dipole potential. An atom illuminated by a laser of frequency ω close to an atomic resonance of frequency ω_0 acquires an electric dipole, which interacts with the laser field. For a two-level atom with a transition dipole d, in a field of local amplitude $E(\mathbf{r})$ (*i.e.* $\mathbf{E}(\mathbf{r},t) = E(\mathbf{r})\cos(\omega t)\,\boldsymbol{\epsilon}$), the Rabi frequency is $\Omega(\mathbf{r}) = dE(\mathbf{r})/\hbar$. If the detuning $\Delta = \omega - \omega_0$ is large compared with Ω and with the natural linewidth Γ of the excited state, the ground state is shifted by the light shift

$$V(\mathbf{r}) = \frac{\hbar\Omega(\mathbf{r})^2}{4\Delta} = \frac{d^2E(\mathbf{r})^2}{4\hbar\Delta}, \tag{2.1}$$

which acts as a potential for the atom center-of-mass motion [9]. For a red detuning ($\Delta < 0$) the atom is attracted towards the intensity maxima, while it is repelled from them for a blue detuning ($\Delta > 0$). The potential scales as I/Δ, where $I \propto E^2$ is the laser intensity, while the rate of spontaneous emission of photons scales as $\Gamma I/\Delta^2$: using large detunings and high intensities, one obtains conservative potentials with a negligible heating due to spontaneous emission.

One-dimensional optical lattice. We consider two counter-propagating laser beams of wave vector $\pm k_{\mathrm{L}}\,\hat{\mathbf{x}}$, with $k_{\mathrm{L}} = 2\pi/\lambda$, of the same frequency, polarization and amplitude E_1 (Fig. 6). They interfere and produce a standing wave, of amplitude $E(x) = 2E_1\cos(k_{\mathrm{L}}x)$. According to Eq. 2.1, the atoms experience the potential $V(x) = (d^2E_1^2/\hbar\Delta)\cos^2(k_{\mathrm{L}}x)$. For a red detuning, it can be written

$$V(x) = V_0\sin^2(k_{\mathrm{L}}x), \qquad V_0 = \frac{d^2E_1^2}{\hbar|\Delta|}, \tag{2.2}$$

up to an irrelevant constant $-V_0$. For a blue detuning, one obtains the same expression after a translation of the origin by a quarter wavelength. The lattice depth V_0 is four times the light shift of a single beam, as the interference doubles the field amplitude at the antinodes. The potential is periodic, with a lattice spacing

$$d = \frac{\lambda}{2} = \frac{\pi}{k_{\mathrm{L}}}. \tag{2.3}$$

Lattices in two or three dimensions are realized by superimposing standing waves along orthogonal directions. When their frequencies are slightly different, the interferences

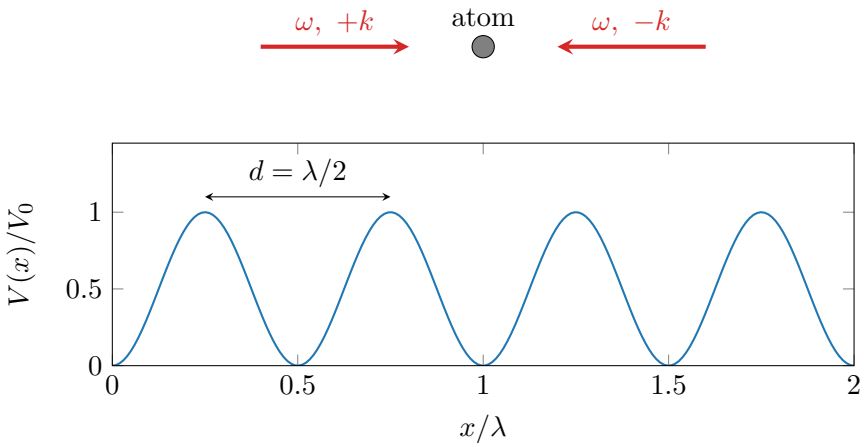


Figure 6: A one-dimensional optical lattice is formed by two counter-propagating laser beams of wave vectors $\pm k_{\mathrm{L}}$. The resulting potential $V(x) = V_0 \sin^2(k_{\mathrm{L}} x)$ has a period $d = \lambda/2$.

between different standing waves average out, and the potential is separable, $V(\mathbf{r}) = V_0[\sin^2(k_{\mathrm{L}} x) + \sin^2(k_{\mathrm{L}} y) + \sin^2(k_{\mathrm{L}} z)]$. The single-particle problem then reduces to three independent one-dimensional problems, which justifies the one-dimensional treatment of this section.

Recoil energy. The atom motion is governed by the Hamiltonian

$$\hat{H} = \frac{\hat{p}^2}{2m} + V_0 \sin^2(k_{\mathrm{L}} \hat{x}). \tag{2.4}$$

The lattice wave number defines a natural energy scale, the recoil energy

$$E_{\mathrm{r}} = \frac{\hbar^2 k_{\mathrm{L}}^2}{2m}, \tag{2.5}$$

which is the kinetic energy acquired by an atom at rest after the absorption of one photon of momentum $\hbar k_{\mathrm{L}}$. For an atom of mass $m = 100\, m_u$ and a wavelength $\lambda = 1\,\mu$m, we find $E_{\mathrm{r}} = h^2/(2m\lambda^2) \simeq h \times 2\,\mathrm{kHz} \simeq k_{\mathrm{B}} \times 100\,\mathrm{nK}$. Typical lattice depths range from a fraction of E_{r} to a few tens of E_{r}.

Mathieu equation. Using the dimensionless variables $\tilde{x} = k_{\mathrm{L}} x$, $\tilde{E} = E/E_{\mathrm{r}}$ and $\tilde{V}_0 = V_0/E_{\mathrm{r}}$, and writing $\sin^2 \tilde{x} = [1 - \cos(2\tilde{x})]/2$, the stationary Schrödinger equation takes the form

$$-\psi''(\tilde{x}) + \frac{\tilde{V}_0}{2}\,[1 - \cos(2\tilde{x})]\,\psi(\tilde{x}) = \tilde{E}\,\psi(\tilde{x}), \tag{2.6}$$

which is known as the Mathieu equation. In the reduced variables, the potential has a period π. In the following, we use dimensionless units whenever we perform explicit calculations, and we often omit the tildes, measuring energies in units of E_{r} and wave numbers in units of k_{L}.

2.1.2 Bloch theorem

The lattice potential is invariant under the translation by one lattice period, $V(x+d) = V(x)$. We introduce the translation operator $\hat{T}_d$, defined by

$$\hat{T}_d\,\psi(x) = \psi(x-d). \tag{2.7}$$

Since the kinetic energy is invariant under any translation and the potential is invariant under $\hat{T}_d$, the translation commutes with the Hamiltonian, $[\hat{T}_d, \hat{H}] = 0$. One can thus look for eigenstates of $\hat{H}$ that are also eigenstates of $\hat{T}_d$. The operator $\hat{T}_d = \mathrm{e}^{-\mathrm{i}\hat{p}d/\hbar}$ is unitary, so that its eigenvalues are complex numbers of modulus one, which we write $\mathrm{e}^{-\mathrm{i}\theta}$, with

$$\psi_\theta(x-d) = \mathrm{e}^{-\mathrm{i}\theta}\psi_\theta(x). \tag{2.8}$$

For a vanishing lattice potential, the eigenstates are plane waves $\mathrm{e}^{\mathrm{i}qx}$, which satisfy this relation with $\theta = qd$. This motivates the definition of the *quasi-momentum* $q = \theta/d$, such that

$$\psi_q(x-d) = \mathrm{e}^{-\mathrm{i}qd}\psi_q(x). \tag{2.9}$$

Equivalently, the eigenstates can be written as

$$\psi_q(x) = \mathrm{e}^{\mathrm{i}qx}u_q(x), \qquad u_q(x-d) = u_q(x), \tag{2.10}$$

i.e. as the product of a plane wave and of a function u_q with the periodicity of the lattice. This is the Bloch theorem [10]: one can look for the eigenstates in the form of *Bloch waves*.

Since θ is defined modulo 2π, the quasi-momentum is defined modulo $2\pi/d = 2k_\mathrm{L}$, the length of the reciprocal lattice vector. One can thus restrict q to the first Brillouin zone $-k_\mathrm{L} \leq q < k_\mathrm{L}$. For each value of q, the periodic function u_q is a solution of the equation

$$\left[\frac{(\hat{p}+\hbar q)^2}{2m} + V(x)\right] u_q(x) = E\,u_q(x) \tag{2.11}$$

on a single lattice period, with periodic boundary conditions. This is a problem on a compact domain, which has a discrete spectrum $E_n(q)$, labelled by the band index $n = 0, 1, 2, \ldots$ For each band n, the energy $E_n(q)$ varies continuously with q, which defines the band structure. We write $\psi_{n,q}(x) = \mathrm{e}^{\mathrm{i}qx}u_{n,q}(x)$ the corresponding Bloch states. Bloch states with different (n,q) are orthogonal, and we normalize them as $\langle\psi_{n,q}|\psi_{n',q'}\rangle = \delta_{n,n'}\delta(q-q')$.

2.1.3 Free-particle spectrum in the reduced zone scheme

Before solving the problem in the presence of the lattice, it is instructive to consider the limit $V_0 \to 0$. The eigenstates are then the plane waves $\mathrm{e}^{\mathrm{i}px/\hbar}$, of energy $p^2/2m$. Writing the momentum as $p = \hbar(q + 2jk_\mathrm{L})$, with q in the first Brillouin zone and $j \in \mathbb{Z}$, the plane wave takes the Bloch form (2.10) with $u_q(x) = \mathrm{e}^{2\mathrm{i}jk_\mathrm{L}x}$, which is indeed d-periodic. The spectrum, plotted as a function of q, consists of the parabolas

$$E(q) = E_\mathrm{r}\left(\frac{q}{k_\mathrm{L}} + 2j\right)^2, \quad j \in \mathbb{Z}, \tag{2.12}$$

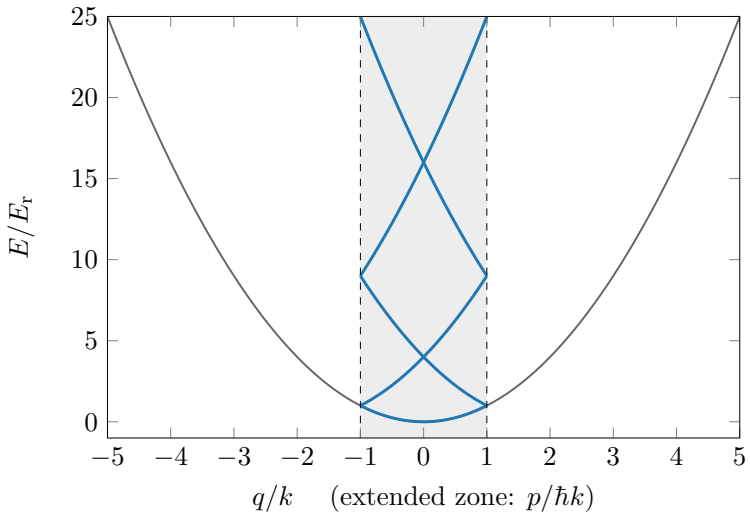


Figure 7: Free-particle spectrum $p^2/2m$ (grey line) and its folding in the first Brillouin zone $-k_\mathrm{L} \leq q < k_\mathrm{L}$ (shaded area, blue lines). The successive branches define the bands $n = 0, 1, 2, \ldots$ of the free particle in the reduced zone scheme.

folded back into the first Brillouin zone (Fig. 7). Sorting them by increasing energy defines the bands $n = 0, 1, 2, \ldots$ of the free particle. The bands touch each other at the center $q = 0$ and at the edges $q = \pm k_\mathrm{L}$ of the Brillouin zone, where two plane waves p and $p \pm 2\hbar k_\mathrm{L}$ are degenerate. We will see that the lattice potential, which couples momenta differing by $2\hbar k_\mathrm{L}$, lifts these degeneracies and opens energy gaps.

2.1.4 Solving the Schrödinger equation: the central equation

Since $u_{n,q}$ is periodic, we expand it in Fourier series, which gives for the Bloch function

$$\psi_{n,q}(\tilde{x}) = \sum_{p\in\mathbb{Z}} c_p(q)\, \mathrm{e}^{\mathrm{i}(2p+q)\tilde{x}}, \qquad -1 \leq q < 1, \tag{2.13}$$

in reduced units. The kinetic energy is diagonal in this basis, with eigenvalues $(2p+q)^2$. The lattice potential reads

$$\frac{V_0}{2}\left[1 - \cos(2\tilde{x})\right] = \frac{V_0}{2} - \frac{V_0}{4}\left(\mathrm{e}^{2\mathrm{i}\tilde{x}} + \mathrm{e}^{-2\mathrm{i}\tilde{x}}\right), \tag{2.14}$$

which couples the Fourier component p to the components $p \pm 1$: physically, the atom absorbs a photon from one beam and emits a photon in the counter-propagating beam, which changes its momentum by $\pm 2\hbar k_\mathrm{L}$. Inserting (2.13) into the Mathieu equation (2.6) and identifying the Fourier components, we obtain the *central equation*

$$\left[(2p+q)^2 + \frac{V_0}{2}\right] c_p - \frac{V_0}{4}\left(c_{p-1} + c_{p+1}\right) = E\, c_p, \qquad p \in \mathbb{Z}. \tag{2.15}$$

For each q, this is an eigenvalue problem for an infinite tridiagonal matrix. To compute the lowest bands, one truncates it to $|p| \leq p_\mathrm{max}$, with typically $p_\mathrm{max} \sim 10$. The discarded coefficients do not matter, because they correspond to momentum states of very high kinetic energy $\sim 4p^2 E_\mathrm{r}$, which are only coupled off-resonantly to the low-energy states,

and are thus negligibly populated. For instance, for $p_{\max} = 3$, the energies $E - V_0/2$ are the eigenvalues of the matrix

$$\begin{pmatrix} (q-6)^2 & -\frac{V_0}{4} & 0 & 0 & 0 & 0 & 0 \\ -\frac{V_0}{4} & (q-4)^2 & -\frac{V_0}{4} & 0 & 0 & 0 & 0 \\ 0 & -\frac{V_0}{4} & (q-2)^2 & -\frac{V_0}{4} & 0 & 0 & 0 \\ 0 & 0 & -\frac{V_0}{4} & q^2 & -\frac{V_0}{4} & 0 & 0 \\ 0 & 0 & 0 & -\frac{V_0}{4} & (q+2)^2 & -\frac{V_0}{4} & 0 \\ 0 & 0 & 0 & 0 & -\frac{V_0}{4} & (q+4)^2 & -\frac{V_0}{4} \\ 0 & 0 & 0 & 0 & 0 & -\frac{V_0}{4} & (q+6)^2 \end{pmatrix}, \tag{2.16}$$

written in the basis $p = -3, \ldots, 3$. The normalized eigenvectors (c_p), with $\sum_p |c_p|^2 = 1$, give the Bloch functions (2.13), with a periodic part $u_{n,q}$ whose mean squared modulus over a lattice period equals one.

Weak lattice: opening of gaps. The central equation allows one to understand the opening of gaps for $V_0 \ll E_\mathrm{r}$. At the edge of the Brillouin zone $q = 1$, the states $p = 0$ and $p = -1$, of momenta $\hbar k_\mathrm{L}$ and $-\hbar k_\mathrm{L}$, are degenerate, with an energy E_r, and they are directly coupled by the matrix element $-V_0/4$. The degeneracy is lifted at first order, the two eigenstates being the symmetric and antisymmetric combinations $\cos(k_\mathrm{L} x)$ and $\sin(k_\mathrm{L} x)$, and the gap between the bands $n = 0$ and $n = 1$ is

$$\Delta_{01} \simeq \frac{V_0}{2}. \tag{2.17}$$

The state $\cos(k_\mathrm{L} x)$, whose density is maximal at the potential minima $x = jd$, is the lower one. At the center of the zone $q = 0$, the states $p = \pm 1$, of momenta $\pm 2\hbar k_\mathrm{L}$ and energy $4E_\mathrm{r}$, are not directly coupled; they are coupled at second order via the state $p = 0$. Only their symmetric combination is coupled to $p = 0$, and it is shifted upwards by $2(V_0/4)^2/(4E_\mathrm{r})$, leading to the gap $\Delta_{12} \simeq V_0^2/(32E_\mathrm{r})$ between the bands $n = 1$ and $n = 2$. More generally, the gap between the bands $n - 1$ and n opens at order n in V_0.

2.1.5 Band structures

We show in Fig. 8 the band structures obtained by numerical diagonalization of the central equation for $V_0 = 2$, 4 and $10\,E_\mathrm{r}$. They interpolate between two limits.

- For a weak lattice ($V_0 = 2\,E_\mathrm{r}$), the band structure resembles the folded free-particle spectrum of Fig. 7, with small gaps opened at the degeneracy points. We find a gap $\Delta_{01} \simeq 1.0\,E_\mathrm{r}$ at the zone edge, in agreement with the estimate $V_0/2$, and a gap $\Delta_{12} \simeq 0.12\,E_\mathrm{r}$ at the zone center, close to $V_0^2/(32E_\mathrm{r}) = 0.125\,E_\mathrm{r}$.

- For a deep lattice ($V_0 = 10\,E_\mathrm{r}$), the lowest bands lying below the potential maximum V_0 become very flat: the width of the ground band is only $0.077\,E_\mathrm{r}$, and it is separated from the first excited band by a gap of about $4.6\,E_\mathrm{r}$. In this regime, each well can be approximated by a harmonic potential $V(x) \simeq V_0 k_\mathrm{L}^2 x^2$ near its minimum, of frequency ω_ho given by

$$\hbar\omega_\mathrm{ho} = 2\sqrt{V_0 E_\mathrm{r}}. \tag{2.18}$$

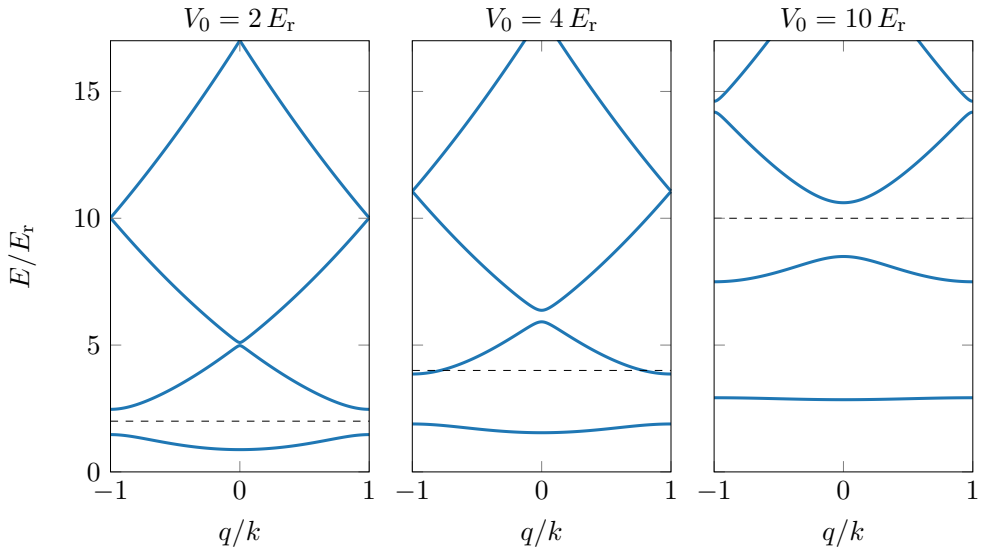


Figure 8: Band structure of the lattice $V(x) = V_0 \sin^2(k_\mathrm{L} x)$ for $V_0 = 2$, 4 and $10\,E_\mathrm{r}$, computed from the central equation (2.15) with $p_\mathrm{max} = 12$. The dashed line indicates the maximum V_0 of the potential. Energies are counted from the potential minimum.

The low-lying bands are then close to the discrete levels $\hbar\omega_\mathrm{ho}(n + 1/2)$ of the harmonic wells, broadened by tunneling between the wells. For $V_0 = 10\,E_\mathrm{r}$ we have $\hbar\omega_\mathrm{ho} \simeq 6.3\,E_\mathrm{r}$; the actual band spacing is smaller, because the sinusoidal wells are softer than their harmonic approximation (anharmonicity).

The bands above the potential maximum remain close to the free-particle parabolas.

2.1.6 Bloch states

We plot in Fig. 9 the probability density of the Bloch state $q = 0$ of the ground band, for the same three lattice depths. Being a Bloch state, it extends over the whole lattice, with a density modulated with the lattice period. For a weak lattice, the modulation is weak, and the state is close to the uniform plane wave $p = 0$. For a deep lattice, the density is concentrated near the potential minima, where it is close to the Gaussian ground state of the harmonic approximation, of width

$$\sigma = \sqrt{\frac{\hbar}{m\omega_\mathrm{ho}}} = \frac{1}{k_\mathrm{L}} \left(\frac{E_\mathrm{r}}{V_0}\right)^{1/4}. \tag{2.19}$$

For $V_0 = 10\,E_\mathrm{r}$ we get $\sigma \simeq 0.18\,d$, so that the density almost vanishes at the potential maxima.

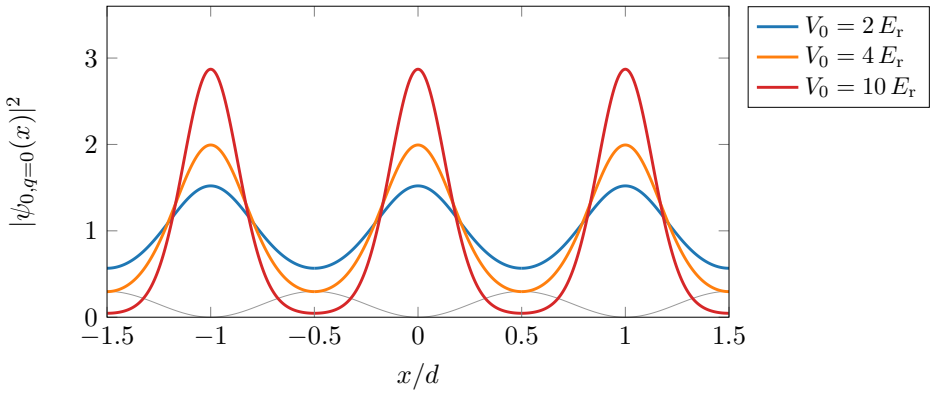


Figure 9: Probability density of the Bloch state $q = 0$ of the ground band for $V_0 = 2$, 4 and $10\,E_\mathrm{r}$, normalized such that its average over one lattice period equals one. The thin grey line indicates the shape of the lattice potential.

2.2 Dynamics of a particle in an optical lattice

We now study the time evolution of atoms in a lattice. The lattice potential can be switched on suddenly or slowly, it can be set in motion, and an additional force can be applied. These situations lead to a variety of phenomena: diffraction of matter waves, adiabatic transfer into Bloch states, mapping of quasi-momenta onto momenta, Bloch oscillations and interband transitions. Most of them are routinely used as tools in cold-atom experiments.

2.2.1 Kapitza-Dirac diffraction

We first consider an atom initially at rest, in the momentum state $|p = 0\rangle$, on which the lattice potential is suddenly switched on. Since the potential couples momenta differing by $2\hbar k_\mathrm{L}$, the atom is diffracted into the momentum states $p = 2j\hbar k_\mathrm{L}$, $j \in \mathbb{Z}$. This is the matter-wave analogue of the diffraction of light by a grating, the role of the grating being played by the light standing wave; it was predicted by Kapitza and Dirac for electrons diffracted by a standing light wave [11].

Raman-Nath regime. For short pulses, one can neglect the kinetic energy during the pulse, *i.e.* neglect the motion of the atom during the interaction. The wave function then simply acquires a position-dependent phase, as for a thin phase grating,

$$\begin{aligned}\psi(x,t) = \mathrm{e}^{-\mathrm{i}V(x)t/\hbar} &= \mathrm{e}^{-\mathrm{i}V_0 t/2\hbar} \exp\left[\mathrm{i}\frac{V_0 t}{2\hbar}\cos(2k_\mathrm{L}x)\right] \\ &= \mathrm{e}^{-\mathrm{i}V_0 t/2\hbar} \sum_{j\in\mathbb{Z}} \mathrm{i}^j \mathcal{J}_j\left(\frac{V_0 t}{2\hbar}\right) \mathrm{e}^{2\mathrm{i}jk_\mathrm{L}x}, \end{aligned} \tag{2.20}$$

where we used the Jacobi-Anger expansion, $\mathcal{J}_j$ denoting the Bessel function of the first kind. The population of the diffraction order j, of momentum $2j\hbar k_\mathrm{L}$, is thus

$$P_j(t) = \mathcal{J}_j^2\left(\frac{V_0 t}{2\hbar}\right). \tag{2.21}$$

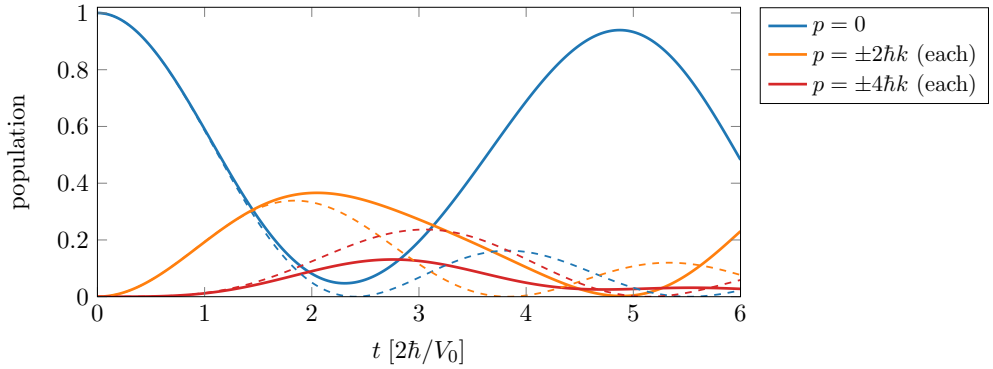


Figure 10: Kapitza-Dirac diffraction of an atom initially at rest, on which a lattice of depth $V_0 = 20\,E_\mathrm{r}$ is suddenly switched on. We show the populations of the momentum states 0, $\pm 2\hbar k_\mathrm{L}$ and $\pm 4\hbar k_\mathrm{L}$ as a function of the pulse duration. Solid lines: exact numerical solution. Dashed lines: Raman-Nath approximation (2.21).

The natural time unit is $2\hbar/V_0$, and the number of significantly populated orders grows linearly with $V_0 t/2\hbar$. This approximation is valid as long as the atom does not move significantly during the pulse, *i.e.* for times short compared with the oscillation period in a well, $t \ll 1/\omega_\mathrm{ho} = \hbar/(2\sqrt{V_0 E_\mathrm{r}})$. Equivalently, the kinetic energy $4j^2 E_\mathrm{r}$ of the populated orders must not induce a significant phase during the pulse.

We compare in Fig. 10 this prediction with the exact solution of the Schrödinger equation, obtained by integrating the evolution in the momentum basis (2.15) with $q = 0$, for $V_0 = 20\,E_\mathrm{r}$. The two agree at short times, $t \lesssim 2\hbar/V_0$, while at longer times the kinetic energy modifies the dynamics, and the populations oscillate instead of spreading to ever higher orders.

Experimental observation. Kapitza-Dirac diffraction of atoms was observed by Gould *et al.* [12], well before the advent of Bose-Einstein condensates. A collimated beam of sodium atoms crossed a near-resonant standing light wave, and the transverse momentum distribution of the atoms was measured downstream. As shown in Fig. 11, it exhibits peaks at even multiples of $\hbar k_\mathrm{L}$, the relative weights of which change with the light intensity, in agreement with the theory.

2.2.2 Loading of the ground band: adiabaticity criterion

To prepare atoms in the ground band of the lattice, one starts with a Bose-Einstein condensate, *i.e.* essentially in the state $p = 0$, which coincides with the Bloch state $q = 0$ of the ground band of the vanishing lattice. One then raises the lattice depth slowly, to adiabatically follow the ground state, using for instance a linear ramp

$$V_0(t) = V_0^\mathrm{f} \frac{t}{\tau}, \qquad 0 \leq t \leq \tau. \tag{2.22}$$

Quasi-momentum is conserved during the ramp, since the Hamiltonian is periodic at all times. The question is to determine how slow the ramp must be.

For moderate lattice depths, the ground state at $q = 0$ is obtained by first-order perturbation theory in the coupling $-V_0/4$ between $p = 0$ and the states $\pm 2\hbar k_\mathrm{L}$, with an

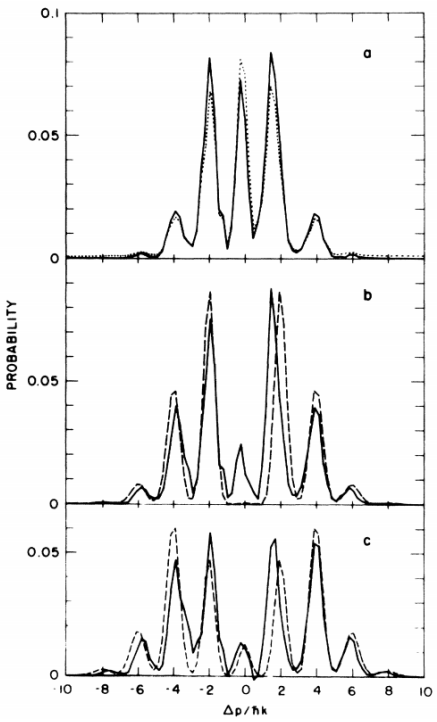


Figure 11: Transverse momentum distribution of a sodium atomic beam after crossing a standing light wave, for three values of the light intensity (a–c). The distribution shows diffraction peaks at even multiples of the photon momentum $\hbar k$. Dashed and dotted lines are theoretical predictions. Figure taken from Ref. [12].

energy denominator $-4E_\mathrm{r}$,

$$|\psi_0\rangle \simeq |p=0\rangle + \frac{V_0}{16E_\mathrm{r}}\left(|p=2\hbar k_\mathrm{L}\rangle + |p=-2\hbar k_\mathrm{L}\rangle\right). \tag{2.23}$$

The ramp can only couple this state to excited states of the same quasi-momentum $q=0$ and of the same parity, the Hamiltonian being even at all times. Among the two states built from $|p=\pm 2\hbar k_\mathrm{L}\rangle$, the odd combination $(|2\hbar k_\mathrm{L}\rangle - |-2\hbar k_\mathrm{L}\rangle)/\sqrt{2}$, which belongs to the band $n=1$, is therefore not coupled. The relevant excited state is the even combination

$$|\psi_2\rangle \simeq \frac{1}{\sqrt{2}}\left(|p=2\hbar k_\mathrm{L}\rangle + |p=-2\hbar k_\mathrm{L}\rangle\right), \tag{2.24}$$

which belongs to the band $n=2$, with an energy difference $\Delta E \simeq 4E_\mathrm{r}$. The adiabaticity criterion requires the non-adiabatic coupling to remain small compared with the energy gap,

$$\hbar\left|\langle\psi_2|\frac{\mathrm{d}}{\mathrm{d}t}|\psi_0\rangle\right| \ll \Delta E. \tag{2.25}$$

With $\langle\psi_2|\frac{\mathrm{d}}{\mathrm{d}t}|\psi_0\rangle = \sqrt{2}\,\dot{V}_0/(16E_\mathrm{r})$ and $\dot{V}_0 = V_0^\mathrm{f}/\tau$, we obtain

$$\tau \gg \frac{1}{32\sqrt{2}}\frac{V_0^\mathrm{f}}{E_\mathrm{r}}\frac{\hbar}{E_\mathrm{r}}. \tag{2.26}$$

This criterion is derived for $V_0 \lesssim E_\mathrm{r}$; at larger depths, the gap to the band $n=2$ increases, so that the beginning of the ramp is the most critical. In practice, ramps of a few hundred microseconds are sufficient for typical recoil energies $E_\mathrm{r} \sim h\times$ a few kHz. The adiabatic loading is much more demanding for states at the edge of the Brillouin zone, where the gap $\Delta_{01} \simeq V_0/2$ vanishes at the beginning of the ramp. In an interacting Bose gas, the loading must moreover be slow compared with the much longer time scales associated with interactions and with the redistribution of atoms in the external trap.

Experimental test. The adiabaticity of the loading was studied by Denschlag *et al.* [13] with a sodium Bose-Einstein condensate. The lattice depth was ramped up linearly and then down symmetrically, and the population remaining in the momentum state $p=0$ was measured. As shown in Fig. 12, short ramps lead to a significant transfer of population to the momentum states $\pm 2\hbar k_\mathrm{L}$, which oscillates with the ramp duration, while for ramps longer than about $15\,\mu$s almost the whole condensate returns to $p=0$, a signature of adiabatic following.

2.2.3 Time of flight versus band mapping

Accessing the *in situ* density distribution of atoms in a lattice is difficult, as it requires an optical resolution below the lattice spacing; it is nevertheless possible with quantum gas microscopes (Fig. 1). More commonly, one accesses the momentum or quasi-momentum distribution using two different methods.

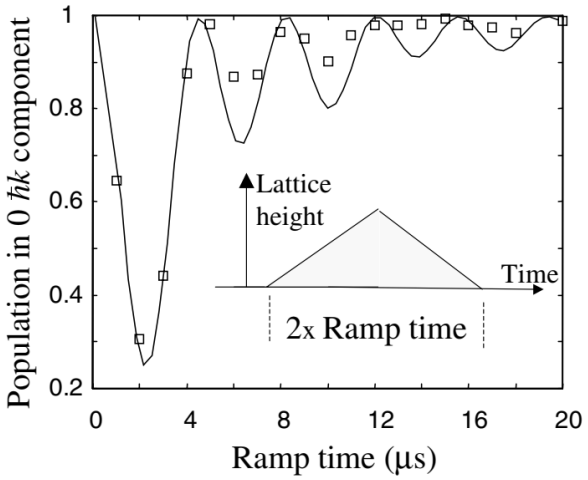


Figure 12: Test of the adiabatic loading of a Bose-Einstein condensate in the ground band of a lattice. The lattice depth is increased and decreased linearly (inset), and the fraction of atoms ending in the momentum state $p = 0$ is measured as a function of the ramp duration (squares). The solid line is the result of a numerical integration of the Schrödinger equation. Figure taken from Ref. [13].

Time of flight. When all potentials are suddenly switched off, the atoms expand freely. After a long expansion time t, the wave function is given by the free propagator in the far-field limit,

$$\psi(\mathbf{r}, t) \simeq \left(\frac{m}{\mathrm{i}t}\right)^{3/2} \tilde{\psi}_0\left(\mathbf{p} = \frac{m\mathbf{r}}{t}\right) \mathrm{e}^{\mathrm{i}mr^2/(2\hbar t)}, \tag{2.27}$$

where $\tilde{\psi}_0(\mathbf{p})$ is the initial wave function in momentum space, normalized as $\int |\tilde{\psi}_0(\mathbf{p})|^2 \mathrm{d}^3p = 1$. This expression holds for $t \gg mR^2/\hbar$, where R is the initial size of the sample. The density after time of flight, $n(\mathbf{r}, t) = (m/t)^3 |\tilde{\psi}_0(m\mathbf{r}/t)|^2$, thus maps the initial momentum distribution (neglecting interactions during the expansion). For a Bloch state $\psi_{n,q}$, the momentum distribution consists of peaks at $p = \hbar(q + 2jk_\mathrm{L})$, with weights $|c_j(q)|^2$: this is the origin of the interference pattern observed when releasing a condensate from a lattice, which will be discussed in section 4.

Band mapping. Alternatively, one can switch off the lattice slowly, adiabatically with respect to the band gaps, but fast compared with the other time scales (tunneling dynamics in the external trap, interactions). Quasi-momentum is conserved during this process, and a Bloch state of the band n and quasi-momentum q is adiabatically connected to the free-particle state of the same quasi-momentum and same band index in Fig. 7, *i.e.* to the momentum $p = \hbar(q + 2jk_\mathrm{L})$ lying in the $(n + 1)$-th Brillouin zone, defined by $n\hbar k_\mathrm{L} \leq |p| < (n + 1)\hbar k_\mathrm{L}$. A subsequent time of flight then measures the population of each band as a function of quasi-momentum. For instance, a gas uniformly filling the ground band, such as a band insulator of fermions or a thermal gas at a temperature larger than the band width but smaller than the gap, produces a uniformly filled first Brillouin zone after band mapping. This is shown in Fig. 13 for a two-dimensional square lattice, where the first Brillouin zone is a square of side $2\hbar k_\mathrm{L}$ [14].

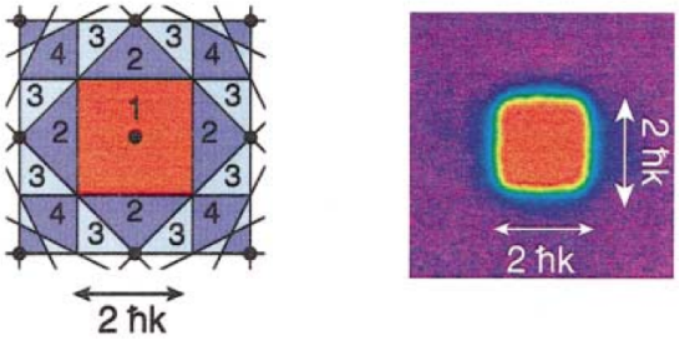


Figure 13: Band mapping in a two-dimensional square lattice. Left: Brillouin zones of the square lattice in momentum space (the numbers label the zones). Right: momentum distribution measured after an adiabatic switch-off of the lattice, for a gas populating uniformly the lowest band: the first Brillouin zone appears as a uniformly filled square of side $2\hbar k$. Figure taken from Ref. [14].

2.2.4 Bragg diffraction

A lattice switched on for a long time with a weak depth does not diffract an atom into many orders, as in the Kapitza-Dirac regime, but resonantly couples two momentum states only. This is the Bragg regime, which we discuss now.

Static lattice. The lattice couples the momentum states $|p\rangle$ and $|p + 2\hbar k_{\mathrm{L}}\rangle$. For a weak and long pulse, the transfer is efficient only if the two states are resonant, $p^2 = (p + 2\hbar k_{\mathrm{L}})^2$, which is fulfilled for $p = -\hbar k_{\mathrm{L}}$ only (Fig. 14a). The momenta $\pm\hbar k_{\mathrm{L}}$ are those of the edge of the Brillouin zone, at which the gap opens: Bragg diffraction and the opening of gaps are two facets of the same physics. At resonance, the two states undergo Rabi oscillations at the frequency $V_0/(2\hbar)$, the coupling being $V_0/4$. A pulse of duration $2\pi\hbar/V_0$ (a π pulse) transfers the atom from $-\hbar k_{\mathrm{L}}$ to $+\hbar k_{\mathrm{L}}$, which realizes a mirror for matter waves, while a $\pi/2$ pulse realizes a coherent beam splitter.

Resonant Bragg diffraction in a moving lattice. In order to diffract atoms of arbitrary momentum, in particular a condensate at rest, one uses two beams of slightly different frequencies ω and $\omega' = \omega - \delta$. The interference pattern

$$V(x,t) = V_0 \sin^2\!\left(k_{\mathrm{L}} x - \frac{\delta}{2} t\right) \tag{2.28}$$

is a lattice moving at the velocity $v = \delta/(2k_{\mathrm{L}})$. In the absorption of a photon from the beam ω followed by the stimulated emission of a photon into the beam ω', the atom gains the momentum $2\hbar k_{\mathrm{L}}$ and the energy $\hbar\delta$. The resonance condition reads

$$\frac{p^2}{2m} + \hbar\delta = \frac{(p + 2\hbar k_{\mathrm{L}})^2}{2m}, \tag{2.29}$$

which is fulfilled for an atom at rest $p = 0$ when $\hbar\delta = 4E_{\mathrm{r}}$ (Fig. 14b). This can be understood in the frame moving with the lattice, in which the atom has a momentum $p - mv$: the resonance condition of the static case, $p - mv = -\hbar k_{\mathrm{L}}$, gives $p = 0$

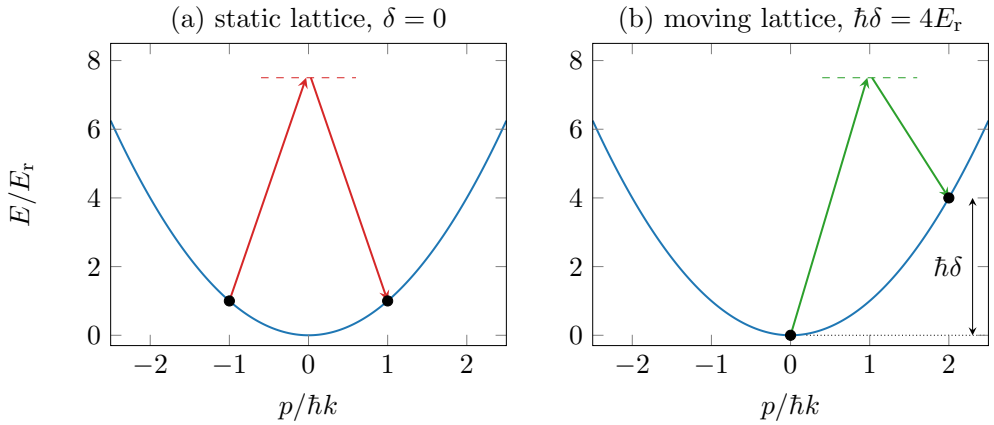


Figure 14: Bragg diffraction as a two-photon transition between free-particle states. (a) In a static lattice, the momenta $-\hbar k_\mathrm{L}$ and $+\hbar k_\mathrm{L}$ are resonantly coupled. (b) In a lattice moving at the velocity $\delta/(2k_\mathrm{L})$, the two-photon transition carries an energy $\hbar\delta$; for $\hbar\delta = 4E_\mathrm{r}$, an atom at rest is resonantly coupled to the momentum $2\hbar k_\mathrm{L}$.

for $v = \hbar k_\mathrm{L}/m$, *i.e.* $\delta = 2\hbar k_\mathrm{L}^2/m = 4E_\mathrm{r}/\hbar$. More generally, using beams that are not counter-propagating, one transfers a momentum $\hbar K$ smaller than $2\hbar k_\mathrm{L}$, with an energy $\hbar\delta$ chosen at will. The narrow resonance condition makes Bragg diffraction a velocity-selective process, which can be used for high-resolution momentum spectroscopy.

Momentum spectroscopy of a BEC. Bragg diffraction of a sodium Bose-Einstein condensate was demonstrated by Kozuma *et al.* [15]. Using laser pulses of controlled frequency difference and direction, a fraction of the condensate was coherently transferred into well-defined momentum states, which separate from the initial condensate during the time of flight (Fig. 15). The momentum width of the condensate, measured from the frequency width of the Bragg resonance, was found to be much smaller than the photon recoil, as expected for a coherent matter wave.

Application 1: spectroscopy of Bogoliubov excitations. When the momentum $\hbar K$ and the energy $\hbar\delta$ transferred by the Bragg beams are varied independently, the resonance condition measures the dispersion relation of the excitations of the gas. For a weakly-interacting Bose-Einstein condensate, the excitations are described by the Bogoliubov dispersion relation

$$\hbar\omega(K) = \sqrt{\hbar^2 c^2 K^2 + \left(\frac{\hbar^2 K^2}{2m}\right)^2}, \tag{2.30}$$

where $c = \sqrt{gn/m}$ is the speed of sound, n the density and $g = 4\pi\hbar^2 a/m$ the interaction parameter. It is linear (phonon-like) for $K \ll 1/\xi$, and quadratic (particle-like, shifted by the mean-field energy gn) for $K \gg 1/\xi$, where $\xi = \hbar/(\sqrt{2}mc)$ is the healing length. This dispersion relation was measured over a broad range of momenta by Steinhauer *et al.* [16], by varying the angle between the Bragg beams (Fig. 16, left), in good agreement with the Bogoliubov prediction.

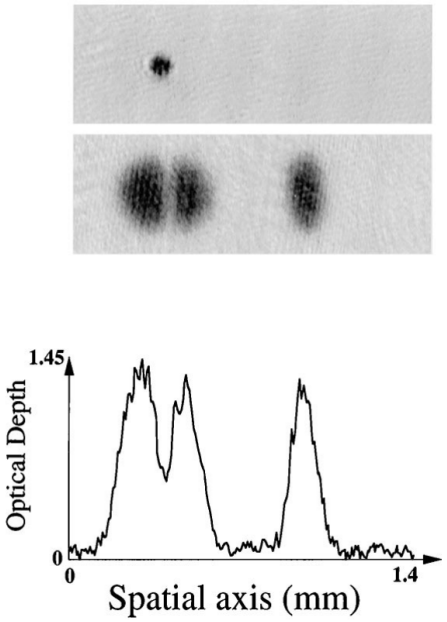


Figure 15: Bragg diffraction of a sodium Bose-Einstein condensate. Top: absorption image of the condensate after time of flight without Bragg pulse. Middle: after Bragg pulses, atoms transferred to other momentum states appear as separate clouds. Bottom: corresponding optical-depth profile. Figure taken from Ref. [15].

Application 2: quantum depletion of a BEC. Even at zero temperature, interactions deplete the condensate, a fraction of the atoms occupying non-zero momentum states. For a homogeneous gas, Bogoliubov theory predicts the condensed fraction [17]

$$\frac{n_0}{n} = 1 - \frac{8}{3\sqrt{\pi}}\sqrt{na^3}. \tag{2.31}$$

Lopes *et al.* [18] measured this quantum depletion with a potassium condensate in a uniform box potential, varying the scattering length with a Feshbach resonance. Bragg diffraction, being velocity-selective, was used to diffract only the condensed atoms, and thus to separate them from the depleted ones. The measured condensed fraction decreases linearly with $\sqrt{na^3}$ (Fig. 16, right), with a slope in agreement with the prediction $8/(3\sqrt{\pi}) \simeq 1.5$.

2.2.5 Propagation of a wave packet: group velocity and effective mass

Group velocity. We consider a wave packet within the ground band,

$$\psi(x,0) = \int_{-k_\mathrm{L}}^{k_\mathrm{L}} c(q)\, \psi_{0,q}(x)\, \mathrm{d}q, \tag{2.32}$$

with an amplitude $c(q)$ peaked around q_0, of width $\delta q \ll k_\mathrm{L}$. Its time evolution reads

$$\psi(x,t) = \int c(q)\, \mathrm{e}^{\mathrm{i}qx} u_{0,q}(x)\, \mathrm{e}^{-\mathrm{i}E_0(q)t/\hbar}\, \mathrm{d}q. \tag{2.33}$$

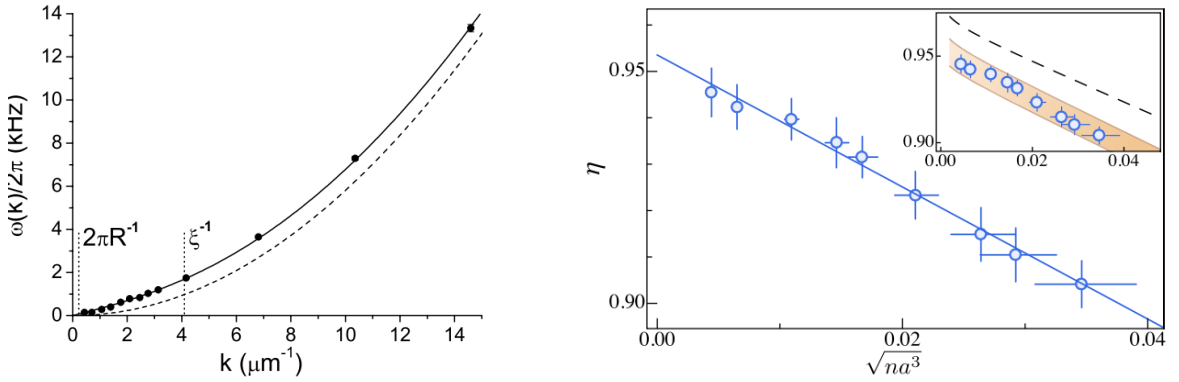


Figure 16: Left: dispersion relation of the excitations of a ^{87}Rb condensate measured by Bragg spectroscopy (points), compared with the Bogoliubov prediction (solid line) and with the free-particle dispersion (dashed line). Figure taken from Ref. [16]. Right: condensed fraction η of a homogeneous ^{39}K condensate as a function of $\sqrt{na^3}$, showing the quantum depletion of the condensate. Figure taken from Ref. [18].

We expand the dispersion relation to first order, $E_0(q) \simeq E_0(q_0) + \hbar v_\mathrm{g}(q-q_0)$, and neglect the variation of $u_{0,q}$ over the width δq, writing $u_{0,q} \simeq u_{0,q_0}$. We obtain

$$\psi(x,t) \simeq \mathrm{e}^{-\mathrm{i}\omega_0 t}\, u_{0,q_0}(x) \int c(q)\, \mathrm{e}^{\mathrm{i}q(x-v_\mathrm{g}t)}\, \mathrm{d}q, \tag{2.34}$$

with

$$v_\mathrm{g} = \frac{1}{\hbar}\left.\frac{\mathrm{d}E_0(q)}{\mathrm{d}q}\right|_{q=q_0}, \qquad \omega_0 = \frac{E_0(q_0)}{\hbar} - q_0 v_\mathrm{g}. \tag{2.35}$$

The envelope of the wave packet thus moves at the group velocity v_g, while the periodic modulation $u_{0,q_0}(x)$ remains attached to the lattice: $\psi(x,t) \simeq \mathrm{e}^{-\mathrm{i}\omega_0 t}\psi(x - v_\mathrm{g}t, 0)$ holds exactly when $v_\mathrm{g}t$ is a multiple of d, and up to the shape of the modulation otherwise. This expression neglects the spreading of the wave packet, which results from the second-order term of the expansion. The group velocity is plotted in Fig. 17a. For a free particle it is the usual velocity $v_\mathrm{g} = \hbar q/m$; in the lattice it is reduced, and it vanishes both at the center $q = 0$ and at the edge $q = \pm k_\mathrm{L}$ of the Brillouin zone, where the dispersion relation is flat. For deep lattices, the group velocity is strongly suppressed over the whole zone.

Effective mass. Near the extrema of the dispersion relation, $q_0 = 0$ and $q_0 = k_\mathrm{L}$, the second-order expansion

$$E_0(q) \simeq E_0(q_0) + \frac{\hbar^2(q-q_0)^2}{2m^*}, \qquad \frac{1}{m^*} = \frac{1}{\hbar^2}\left.\frac{\mathrm{d}^2E_0}{\mathrm{d}q^2}\right|_{q_0}, \tag{2.36}$$

defines an effective mass m^*, with which the wave packet moves as a free particle. The effective mass is plotted in Fig. 17b as a function of the lattice depth. At the zone center, $m^* > m$: the lattice slows down the atoms. For a weak lattice, second-order perturbation theory gives $E_0(q) = q^2 + V_0/2 - (V_0^2/32)/(1-q^2)$ in reduced units, *i.e.* $m^*/m \simeq 1 + V_0^2/(32E_\mathrm{r}^2)$; for a deep lattice, the effective mass increases exponentially with V_0, following the decrease of the tunnel coupling (see section 2.3). At the zone

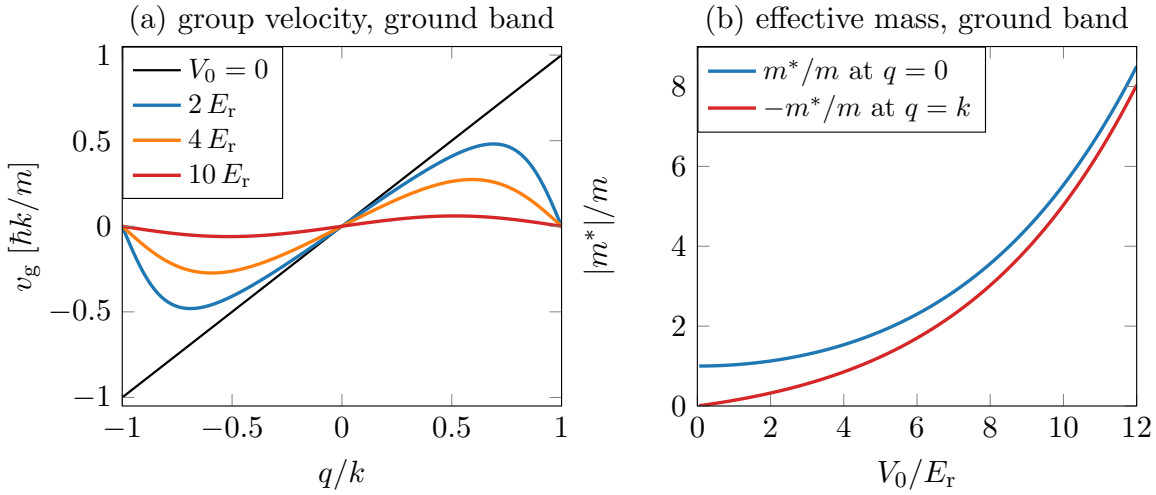


Figure 17: (a) Group velocity in the ground band as a function of quasi-momentum, for $V_0 = 0$, 2, 4 and $10\,E_\mathrm{r}$. (b) Effective mass at the center ($q = 0$) and at the edge ($q = k_\mathrm{L}$, where $m^* < 0$) of the Brillouin zone, as a function of the lattice depth.

edge, the effective mass is negative: the two-level model of the gap opening gives $m^*/m \simeq -V_0/(8E_\mathrm{r})$ for a weak lattice. A negative effective mass means that the atom accelerates in the direction opposite to an applied force. For a Bose-Einstein condensate with repulsive interactions, it is equivalent to attractive interactions with a positive mass, and it leads to a dynamical (modulational) instability of the condensate prepared at the band edge [19].

2.2.6 Action of an external force

We now consider the effect of a uniform force F, due for instance to gravity, or to an acceleration of the lattice, on the atom dynamics, described by the Hamiltonian

$$\hat{H} = \frac{\hat{p}^2}{2m} + V_0 \sin^2(k_\mathrm{L}\hat{x}) - F\hat{x}. \tag{2.37}$$

The linear potential breaks the discrete translation symmetry, so that the Bloch theorem does not apply. For $V_0 = 0$, the momentum of a classical particle evolves as $p(t) = p(0) + Ft$, which suggests to perform a gauge transformation to a frame in which the momentum is shifted by Ft. We use the time-dependent unitary transformation $\hat{U}(t) = \mathrm{e}^{-\mathrm{i}Ft\hat{x}/\hbar}$, under which the Hamiltonian becomes

$$\hat{H}' = \hat{U}\hat{H}\hat{U}^\dagger + \mathrm{i}\hbar\,(\partial_t\hat{U})\,\hat{U}^\dagger. \tag{2.38}$$

We have $\hat{U}\hat{p}\,\hat{U}^\dagger = \hat{p} + Ft$ and $\mathrm{i}\hbar(\partial_t\hat{U})\hat{U}^\dagger = F\hat{x}$, which cancels the linear potential, so that

$$\hat{H}' = \frac{(\hat{p} + Ft)^2}{2m} + V_0 \sin^2(k_\mathrm{L}\hat{x}). \tag{2.39}$$

The Hamiltonian $\hat{H}'$ is time-dependent, but it is invariant under lattice translations at all times: it conserves the quasi-momentum. A Bloch state $\psi'(x,0) = \mathrm{e}^{\mathrm{i}q_\mathrm{i}x}u(x,0)$ thus

remains a Bloch state of the same quasi-momentum q_i in the transformed frame. Coming back to the laboratory frame, $\psi(x,t) = \mathrm{e}^{\mathrm{i}Ftx/\hbar}\psi'(x,t)$, we find that

$$\psi(x,0) = \mathrm{e}^{\mathrm{i}q_\mathrm{i}x}u(x,0) \quad \longrightarrow \quad \psi(x,t) = \mathrm{e}^{\mathrm{i}q(t)x}u(x,t), \qquad q(t) = q_\mathrm{i} + \frac{Ft}{\hbar}. \tag{2.40}$$

The quasi-momentum thus evolves linearly in time, according to the 'acceleration theorem' $\hbar\dot{q} = F$, which is the analogue of Newton's law, the lattice force being absorbed in the band structure. Note that the periodic function $u(x,t)$ is not necessarily the periodic part of a Bloch state of a given band: the force can induce transitions between bands, as discussed in section 2.2.8.

2.2.7 Bloch oscillations

Principle. If the force is weak enough, the atom stays in the ground band, and its state is at all times the Bloch state $\psi_{0,q(t)}$, with $q(t) = q_\mathrm{i} + Ft/\hbar$. Since the band structure is periodic in q, with period $2k_\mathrm{L}$, the evolution is periodic, of period

$$T_\mathrm{B} = \frac{2\hbar k_\mathrm{L}}{F} = \frac{h}{Fd}. \tag{2.41}$$

This is the phenomenon of Bloch oscillations, predicted for electrons in crystals but never observed in natural solids, where the scattering of electrons on defects and phonons occurs on time scales much shorter than T_B. It was first observed with cold atoms by Ben Dahan *et al.* [20], using cesium atoms in an accelerated optical lattice (Fig. 18). The momentum distribution measured at different times shows a peak drifting linearly towards $+\hbar k_\mathrm{L}$, then disappearing while a peak reappears at $-\hbar k_\mathrm{L}$, before drifting back to its initial value after one Bloch period.

Interpretation in terms of Bragg reflection. In a weak lattice, Bloch oscillations can be understood in terms of the free-particle dispersion relation (Fig. 19). The atom momentum increases linearly under the action of the force, until it reaches the value $\hbar k_\mathrm{L}$, where the Bragg resonance condition is fulfilled. The atom is then Bragg reflected to $-\hbar k_\mathrm{L}$, and it is accelerated again. The Bragg reflection is efficient if the atom spends enough time near resonance, which is the condition for staying in the ground band.

Amplitude in real space. The center of mass of a wave packet in the ground band moves at the group velocity (2.35), evaluated at the instantaneous quasi-momentum,

$$\frac{\mathrm{d}\bar{x}}{\mathrm{d}t} = v_\mathrm{g}(q(t)) = \frac{1}{\hbar}\left.\frac{\mathrm{d}E_0(q)}{\mathrm{d}q}\right|_{q(t)}. \tag{2.42}$$

Using $\mathrm{d}q = F\,\mathrm{d}t/\hbar$, we obtain

$$\bar{x}(t) - \bar{x}(0) = \frac{1}{\hbar}\int_0^t \left.\frac{\mathrm{d}E_0}{\mathrm{d}q}\right|_{q(t')} \mathrm{d}t' = \frac{1}{F}\left[E_0(q(t)) - E_0(q_\mathrm{i})\right]. \tag{2.43}$$

This expresses energy conservation: the potential energy $-F\bar{x}$ lost by the atom is converted into band energy. The motion in real space is thus an oscillation, whose

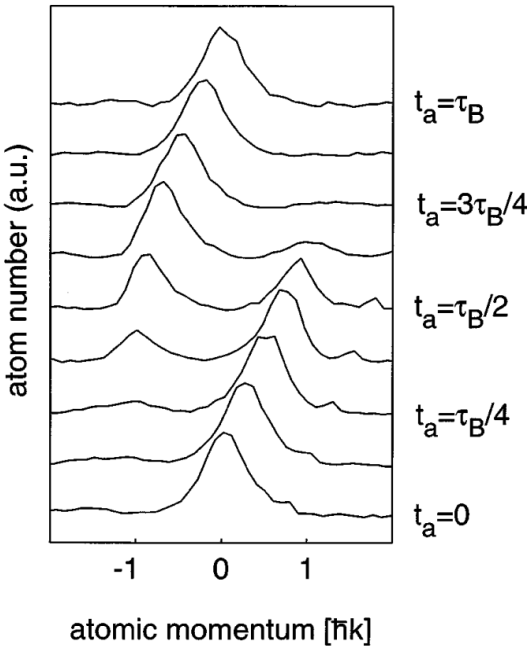


Figure 18: Observation of Bloch oscillations of cold cesium atoms in an accelerated optical lattice. The momentum distribution, measured at successive times t_a during one Bloch period τ_B, drifts linearly and is Bragg reflected from $+\hbar k$ to $-\hbar k$ at the zone edge. Figure taken from Ref. [20].

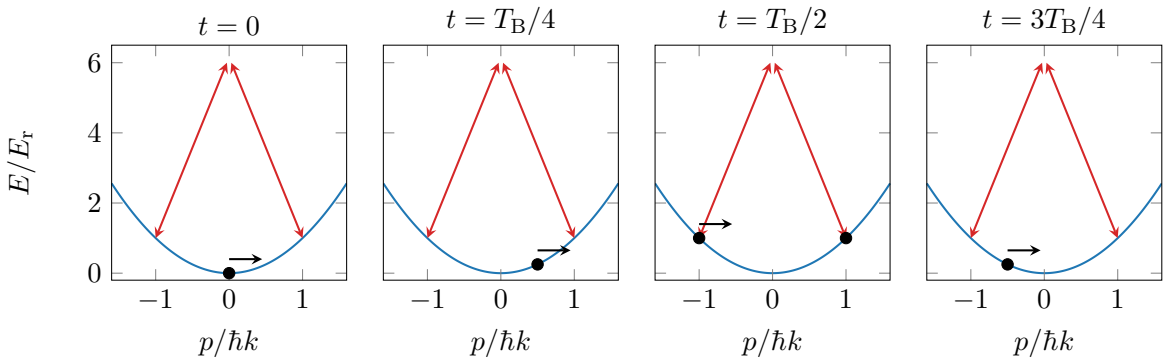


Figure 19: Interpretation of Bloch oscillations in a weak lattice. The momentum of the atom (black dot) increases under the action of the force (black arrow); when it reaches $\hbar k_\mathrm{L}$, the atom is Bragg reflected to $-\hbar k_\mathrm{L}$ by the two-photon process indicated by the red arrows.

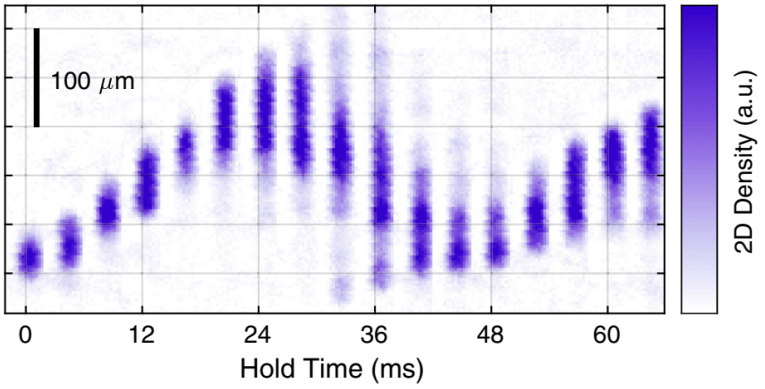


Figure 20: Bloch oscillations observed in real space: in situ density of an ultracold gas in a tilted lattice, as a function of the hold time. Figure taken from Ref. [21].

amplitude (peak to peak) is W/F, where W is the width of the ground band. In particular, the atom does not drift under the action of a constant force, as long as it stays in the ground band. For deep lattices, the band is almost flat and the real-space oscillation is small compared with the lattice spacing, while in shallow lattices and for weak forces it can reach macroscopic values, as observed by Geiger *et al.* [21] with an amplitude of about $100\,\mu$m (Fig. 20). The breathing of the wave packet also visible in the figure results from the dependence of the oscillation on the initial quasi-momentum.

Metrology based on Bloch oscillations. The Bloch period $T_\mathrm{B} = h/(Fd)$ only depends on Planck's constant and on the lattice spacing, which is known from the laser wavelength. Measuring T_B is thus a very efficient way to measure a force with high precision. This idea was applied by Poli *et al.* [22] to measure the gravitational acceleration g with ^{88}Sr atoms in a vertical lattice of spacing $d = 266\,$nm, for which $T_\mathrm{B} = h/(mgd) \simeq 1.7\,$ms. Thanks to the very weak interactions and the insensitivity of ^{88}Sr to magnetic fields, the oscillations could be followed over more than ten seconds (Fig. 21, top), *i.e.* up to 10^4 oscillations, leading to a relative uncertainty $\Delta g/g \sim 10^{-7}$.

Bloch oscillations in an accelerated lattice. The interference between two counter-propagating beams of frequencies ω and ω' produces a moving lattice $V(x,t) = V_0 \sin^2[k_\mathrm{L}x - (\omega - \omega')t/2]$, as seen above. Sweeping linearly the frequency difference produces a uniformly accelerated lattice, of acceleration $a = (\mathrm{d}(\omega - \omega')/\mathrm{d}t)/(2k_\mathrm{L})$. In the lattice frame of reference, the atoms experience the inertial force $F = -ma$, and they undergo Bloch oscillations. Each Bloch oscillation corresponds to a Bragg reflection, in which the atom gains a momentum $2\hbar k_\mathrm{L}$ in the laboratory frame: the atoms are coherently accelerated with the lattice. Performing many cycles thus transfers a large and precisely known number of photon momenta. Measuring the corresponding change of velocity, $2N\hbar k_\mathrm{L}/m$ after N oscillations, by atom interferometry gives access to the ratio h/m with high precision. Combined with the known values of the Rydberg constant and of the atomic and electron masses, this gives a determination of the fine-structure constant. Morel *et al.* [23] obtained in this way $\alpha^{-1} = 137.035\,999\,206(11)$, with a relative uncertainty of 8×10^{-11} (Fig. 21, bottom).

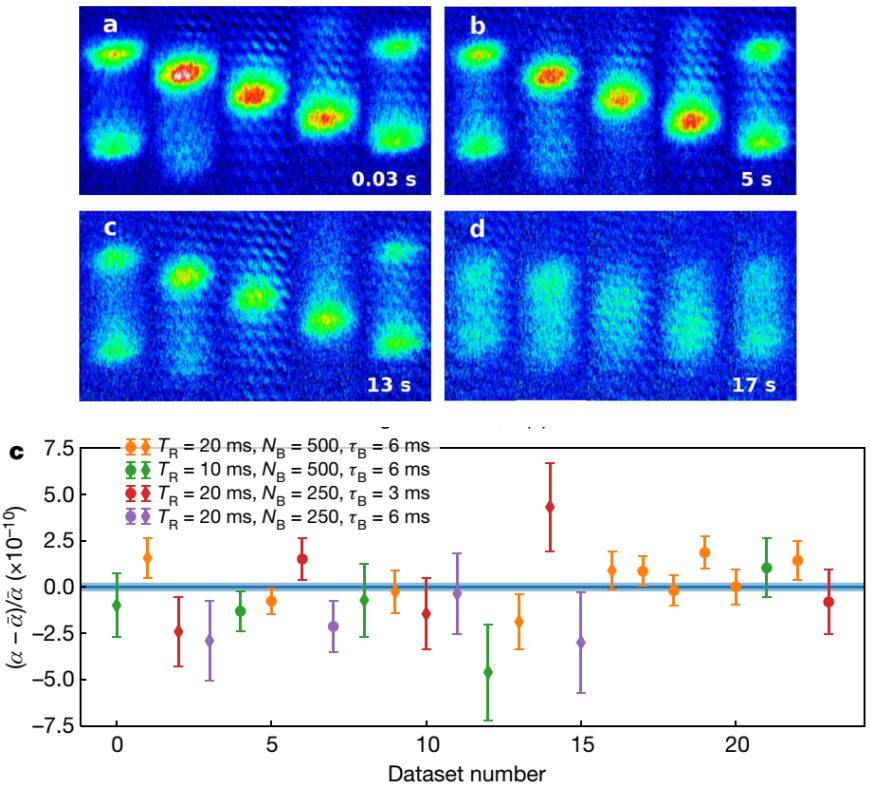


Figure 21: Top: Bloch oscillations of ^{88}Sr atoms in a vertical lattice under the action of gravity. Each panel shows the momentum distribution at different times within a Bloch period, after holding times from 0.03 s to 17 s. Figure taken from Ref. [22]. Bottom: series of measurements of the fine-structure constant α using Bloch oscillations in an accelerated lattice, for different experimental parameters. Figure taken from Ref. [23].

2.2.8 Landau-Zener transitions

If the force is too large, the system does not remain in the ground band. As shown in Fig. 22, the quasi-momentum scans the band structure at a rate $F/\hbar$. For a weak force, the atom follows the ground band adiabatically when crossing the avoided crossing at the zone edge, which leads to Bloch oscillations. For a strong force, the avoided crossing is crossed diabatically, and the atom follows the free-particle parabola, *i.e.* it is accelerated as if there was no lattice. For an intermediate force, the atom ends in a coherent superposition of both possibilities.

The transition probability is given by the Landau-Zener formula [24]. For a weak lattice, we restrict the dynamics near the zone edge to the two states $|\hbar q\rangle$ and $|\hbar(q-2k_\mathrm{L})\rangle$, coupled by the matrix element $V_0/4$. Their energy difference

$$\frac{\hbar^2 q^2}{2m} - \frac{\hbar^2 (q-2k_\mathrm{L})^2}{2m} = \frac{2\hbar^2 k_\mathrm{L}}{m}(q-k_\mathrm{L}) \tag{2.44}$$

varies linearly in time at the rate $\alpha = 2\hbar k_\mathrm{L} F/m$. For a two-level system with a coupling V and an energy difference varying at the rate α, the probability of a diabatic transition is $P = \exp(-2\pi V^2/\hbar\alpha)$. With $V = V_0/4$, we obtain the probability of a transition to the first excited band at each passage through the zone edge,

$$P_\mathrm{LZ} = \exp\left(-\frac{\pi}{32}\,\frac{V_0^2}{E_\mathrm{r}\,F/k_\mathrm{L}}\right) = \exp\left(-\frac{\pi^2}{32}\,\frac{V_0^2}{E_\mathrm{r}\,Fd}\right). \tag{2.45}$$

The force must thus be small compared with $V_0^2/(E_\mathrm{r} d)$ for the atom to remain in the ground band. We checked this formula against a numerical integration of the Schrödinger equation (in the momentum basis of the central equation, with a time-dependent quasi-momentum): for $V_0 = E_\mathrm{r}$ and $F = 0.05\,E_\mathrm{r} k_\mathrm{L}$, both give $P_\mathrm{LZ} \simeq 0.14$. For deeper lattices, the two-level description fails and the gap must be computed numerically, but the transition probability remains exponentially small as long as the force is weak enough, $Fd \ll \Delta_{01}^2/E_\mathrm{r}$.

Experimental observation. Anderson and Kasevich [25] loaded a rubidium Bose-Einstein condensate in a vertical optical lattice, in which the atoms performed Bloch oscillations under the action of gravity. Each time the atoms reached the zone edge, a small fraction underwent a Landau-Zener transition to the excited bands, which are not bound for this shallow lattice, and fell freely. The atoms were thus released as a train of pulses, separated by the Bloch period (Fig. 23). The pulses are coherent with each other, as they originate from the same condensate, and they interfere: this was interpreted as a pulsed, mode-locked atom laser.

Landau-Zener transitions also offer other possibilities: an intermediate force can be used to prepare a coherent superposition of Bloch bands, and when the avoided crossing is passed twice, the two paths interfere, giving rise to Stückelberg oscillations of the final band populations.

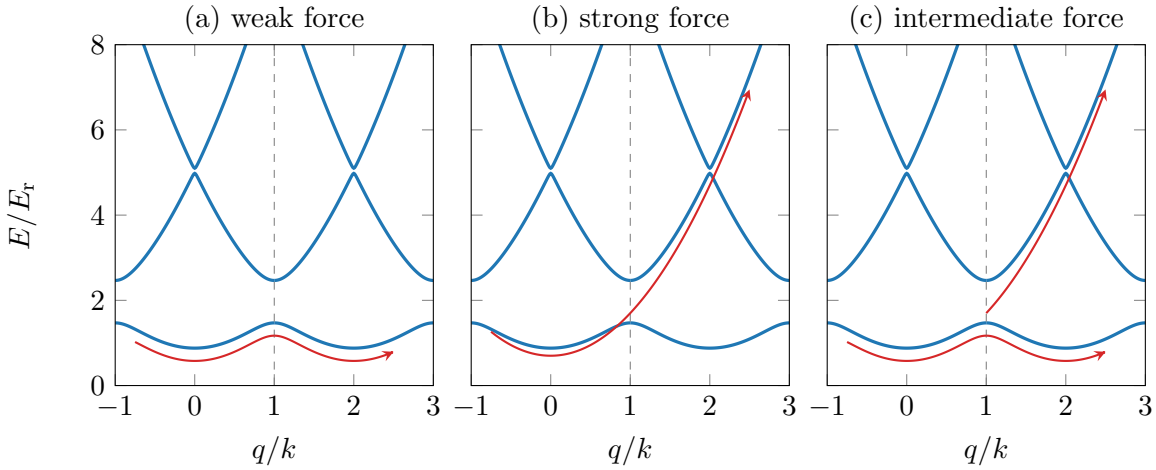


Figure 22: Band structure for $V_0 = 2\,E_\mathrm{r}$, represented over two Brillouin zones, and evolution of the quasi-momentum under the action of a force (red arrows). (a) For a weak force, the atom remains in the ground band (Bloch oscillation). (b) For a strong force, it follows the free-particle parabola. (c) For an intermediate force, it undergoes a Landau-Zener transition with a probability (2.45), and ends in a superposition of both bands.

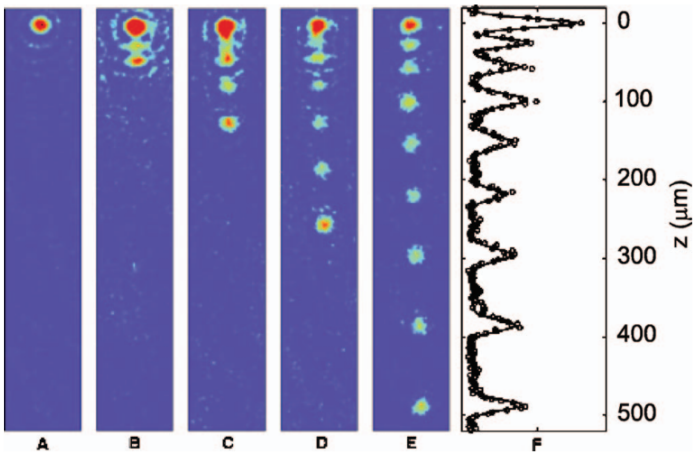


Figure 23: (A–E) Absorption images of a rubidium condensate held in a vertical optical lattice for increasing times: at each Bloch oscillation, a fraction of the atoms undergoes a Landau-Zener transition and falls under gravity, forming a train of pulses. (F) Density profile of the pulse train. Figure taken from Ref. [25].

2.3 Wannier functions and tight-binding limit

Bloch states are extended over the whole lattice, which is not convenient to describe deep lattices, in which atoms are localized in individual wells and move by tunneling. In this section we introduce the Wannier functions, which are localized states spanning a given Bloch band, and we use them to derive the tight-binding description of the lattice.

2.3.1 Wannier functions

Bloch functions are the equivalent of plane waves in a lattice potential. We want to define the equivalent of 'position eigenstates' within a given Bloch band, *i.e.* the states of the band that are the most localized around a given lattice site $x_j = jd$, $j \in \mathbb{Z}$. They are given by the Wannier functions, defined as

$$w_{n,j}(x) = \frac{1}{\sqrt{2k_\mathrm{L}}} \int_{-k_\mathrm{L}}^{k_\mathrm{L}} \psi_{n,q}(x)\, \mathrm{e}^{-\mathrm{i}qx_j}\, \mathrm{d}q, \tag{2.46}$$

with the Bloch states normalized as $\langle \psi_{n,q} | \psi_{n',q'} \rangle = \delta_{n,n'} \delta(q - q')$. The inverse relation reads

$$\psi_{n,q}(x) = \frac{1}{\sqrt{2k_\mathrm{L}}} \sum_{j \in \mathbb{Z}} \mathrm{e}^{\mathrm{i}qx_j} w_{n,j}(x), \tag{2.47}$$

as can be checked using $\sum_j \mathrm{e}^{\mathrm{i}(q-q')jd} = 2k_\mathrm{L}\, \delta(q - q')$ for q, q' in the first Brillouin zone. These functions have the following properties.

- Using the Bloch condition (2.9), $\psi_{n,q}(x) = \mathrm{e}^{\mathrm{i}qx_j} \psi_{n,q}(x - x_j)$, the Wannier functions of the same band are related by translation,

$$w_{n,j}(x) = w_n(x - x_j), \qquad w_n \equiv w_{n,0}. \tag{2.48}$$

- They form an orthonormal basis of the band n,

$$\int w^*_{n,j}(x)\, w_{n',j'}(x)\, \mathrm{d}x = \delta_{n,n'} \delta_{j,j'}, \tag{2.49}$$

  which follows from the orthonormality of the Bloch states and from the relation

$$\frac{1}{2k_\mathrm{L}} \int_{-k_\mathrm{L}}^{k_\mathrm{L}} \mathrm{e}^{\mathrm{i}q(x_j - x_{j'})} \mathrm{d}q = \delta_{j,j'}. \tag{2.50}$$

  The Wannier functions of all bands thus form an orthonormal basis of the single-particle Hilbert space.

- The Bloch states are defined up to a q-dependent phase, which affects the Wannier functions. For the ground band of a simple lattice, the most localized Wannier function is obtained by choosing the phases such that $\psi_{0,q}(0)$ is real and positive for all q [26]. The Wannier function is then real, even, and it decays exponentially at large distance.

We plot in Fig. 24 the Wannier function of the ground band, computed numerically from (2.46) for various lattice depths. For $V_0 = 0$, it reduces to the function $w_0(x) = d^{-1/2} \sin(\pi x/d)/(\pi x/d)$, which spreads over many sites with slowly decaying oscillations. For $V_0 \gg E_\mathrm{r}$, the Wannier function is mostly localized within a single lattice well, its shape being close to the Gaussian ground state of the harmonic approximation of the well bottom, of width σ given by (2.19). Small oscillations remain in the neighbouring wells, which ensure the orthogonality between Wannier functions of different sites.

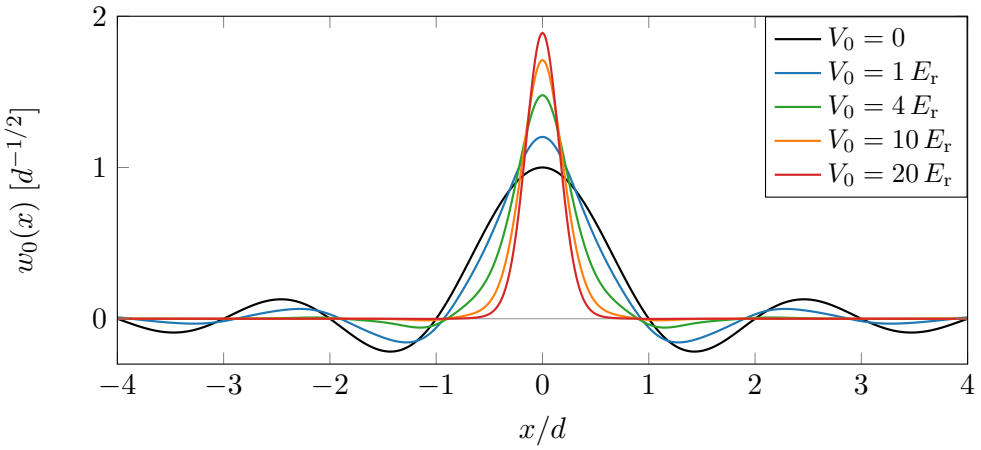


Figure 24: Wannier function $w_0(x)$ of the ground band, for lattice depths $V_0 = 0$, 1, 4, 10 and 20 E_r. It is normalized as $\int |w_0|^2 \mathrm{d}x = 1$.

2.3.2 Hamiltonian in the Wannier basis

We now express the single-particle Hamiltonian in second quantization in the Wannier basis. We denote by $\hat{a}_{n,j}$ the operator annihilating a particle in the Wannier state $w_{n,j}$. The Hamiltonian reads

$$\hat{H} = \sum_n \sum_{j,j'} J_n(j-j')\, \hat{a}^\dagger_{n,j} \hat{a}_{n,j'}, \tag{2.51}$$

where the matrix element

$$J_n(j) = \int w^*_{n,j}(x) \left[-\frac{\hbar^2}{2m} \frac{\mathrm{d}^2}{\mathrm{d}x^2} + V(x) \right] w_{n,0}(x)\, \mathrm{d}x \tag{2.52}$$

only depends on the distance j between the two sites, by translation invariance. The Hamiltonian does not couple different bands, since each band is a stable subspace of $\hat{H}$, but within a band it couples a priori all Wannier states: $J_n(j-j')$ is the tunneling amplitude between the sites j' and j. Inserting the definition (2.46) into (2.52), we find that the tunneling amplitudes are the Fourier coefficients of the dispersion relation,

$$J_n(j) = \frac{1}{2k_\mathrm{L}} \int_{-k_\mathrm{L}}^{k_\mathrm{L}} E_n(q)\, \mathrm{e}^{\mathrm{i}qjd}\, \mathrm{d}q, \qquad E_n(q) = \sum_{j\in\mathbb{Z}} J_n(j)\, \mathrm{e}^{-\mathrm{i}qjd}. \tag{2.53}$$

Since $E_n(q) = E_n(-q)$ for our symmetric lattice, the coefficients $J_n(j) = J_n(-j)$ are real. The relation (2.53) provides a convenient way to compute the tunneling amplitudes from the band structure, which we used for the numerical results below.

2.3.3 Tight-binding limit

For $V_0 \gg E_\mathrm{r}$, the Wannier functions are strongly localized in a given well, and the overlap between distant Wannier functions decreases exponentially. We then have the following properties.

- The tunneling between nearest neighbours dominates over longer-range tunneling. We define the tunnel coupling J as

$$J \equiv -J_0(1) > 0, \tag{2.54}$$

the minus sign ensuring that J is positive for the ground band. As shown in Fig. 25, the next-nearest-neighbour tunneling $J_0(2)$ is already twenty times smaller than J for $V_0 = 5\,E_\mathrm{r}$, and the ratio decreases quickly with V_0.

- Keeping only the nearest-neighbour terms, the dynamics in the lowest band is described by the tight-binding Hamiltonian

$$\hat{H} = -J \sum_j \left(\hat{a}_{j+1}^\dagger \hat{a}_j + \hat{a}_j^\dagger \hat{a}_{j+1} \right), \tag{2.55}$$

  where $\hat{a}_j \equiv \hat{a}_{0,j}$, and where we dropped the constant on-site energy $J_0(0)$. According to (2.53), the corresponding dispersion relation is

$$E_0(q) = -2J \cos(qd), \tag{2.56}$$

  so that the tunnel coupling is directly related to the band width $W = 4J$. The effective mass at the bottom of the band is $m^* = \hbar^2/(2Jd^2)$. For $V_0 = 10\,E_\mathrm{r}$, the exact ground band differs from (2.56) by about 1% of its width.

- In the limit $V_0 \gg E_\mathrm{r}$, the tunnel coupling takes the asymptotic form

$$J \simeq \frac{4}{\sqrt{\pi}} E_\mathrm{r} \left(\frac{V_0}{E_\mathrm{r}} \right)^{3/4} \exp\left[-2 \left(\frac{V_0}{E_\mathrm{r}} \right)^{1/2} \right]. \tag{2.57}$$

  This expression follows from the asymptotic behaviour of the characteristic values of the Mathieu equation. Writing (2.6) in the standard form $y'' + (a - 2\eta \cos 2v) y = 0$, with $\eta = -V_0/(4E_\mathrm{r})$ and $a = (E - V_0/2)/E_\mathrm{r}$, the width of the lowest band is the difference between the characteristic values a_0 and b_1 associated with the periodic ($q = 0$) and antiperiodic ($q = k_\mathrm{L}$) solutions, for which [27]

$$|b_1 - a_0| \simeq 32 \sqrt{\frac{2}{\pi}}\, |\eta|^{3/4}\, \mathrm{e}^{-4\sqrt{|\eta|}}. \tag{2.58}$$

  With $|\eta| = V_0/(4E_\mathrm{r})$, we obtain $W = (16/\sqrt{\pi})\, E_\mathrm{r}\, (V_0/E_\mathrm{r})^{3/4} \exp[-2(V_0/E_\mathrm{r})^{1/2}]$, and $J = W/4$ gives (2.57). The exponential suppression is typical of quantum tunneling through a barrier: the factor $2\sqrt{V_0/E_\mathrm{r}}$ is the WKB action $\int \sqrt{2mV(x)}\,\mathrm{d}x/\hbar$ across one potential barrier, evaluated at the bottom of the well. We compared (2.57) with the exact numerical value: it overestimates J by 31% at $V_0 = 5\,E_\mathrm{r}$, 18% at $10\,E_\mathrm{r}$, 12% at $20\,E_\mathrm{r}$ and 7% at $50\,E_\mathrm{r}$, the relative error decreasing slowly, as $(V_0/E_\mathrm{r})^{-1/2}$. For quantitative purposes, one should thus use the numerical value of J.

We also show in Fig. 25 the tunneling amplitude $J_1(1)$ in the first excited band. It is much larger than J, since the excited Wannier functions are less localized; it is positive, the first excited band having its maximum at the zone center. For $V_0 \gtrsim 5\,E_\mathrm{r}$, the ground-band dynamics is thus well described by the tight-binding Hamiltonian (2.55), provided the energy scales involved (temperature, interactions, external potentials) remain small compared with the band gap. This Hamiltonian, supplemented by the on-site interactions, leads to the Hubbard models studied in sections 4 and 5. The same construction applies to lattices with several sites per unit cell, which are discussed in section 3. We note that the tunneling amplitude is denoted t in some references, including the notes *Advanced quantum mechanics*; we use here the notation J, common in the cold-atom literature.

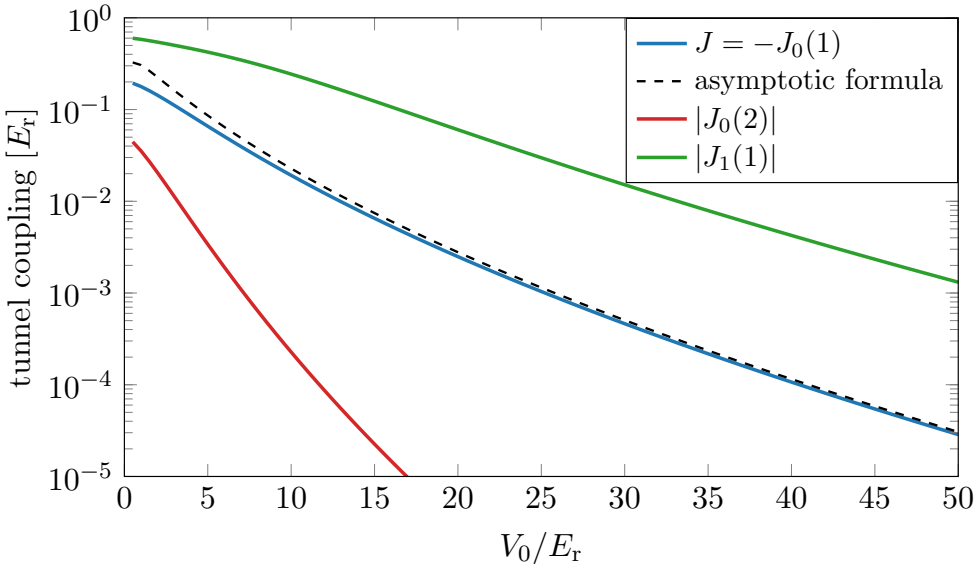


Figure 25: Tunneling amplitudes as a function of the lattice depth, computed from the band structure using (2.53): nearest-neighbour tunnel coupling $J = -J_0(1)$ in the ground band (blue) compared with the asymptotic formula (2.57) (dashed), next-nearest-neighbour tunneling $J_0(2)$ in the ground band (red), and nearest-neighbour tunneling $J_1(1)$ in the first excited band (green).

3 Complex lattices and topological bands

So far we considered the simplest optical lattices, obtained with a single standing wave along each direction, whose lowest band is described by a tight-binding model with a single site per unit cell and real tunneling amplitudes (see section 2). Optical lattices can be made much richer by superimposing several standing waves, by using non-orthogonal or non-separable laser configurations, or by modulating the potential in time. In this section we show that such 'complex' lattices give access to band structures with several sites per unit cell, to Dirac points, and to tunneling amplitudes carrying a complex phase that mimics the effect of a magnetic field on charged particles.

A new ingredient then appears: the Bloch states of a given band can acquire a non-trivial geometry, characterized by Berry phases and Berry curvatures in momentum space. Some of these geometric quantities are quantized and cannot change without closing an energy gap: they define *topological* invariants. We illustrate these ideas on two paradigmatic examples, the one-dimensional Su-Schrieffer-Heeger (SSH) model, characterized by its Zak phase, and the two-dimensional Hofstadter model, whose bands carry a Chern number related to the quantum Hall effect. In both cases we describe experiments in which these topological properties have been measured with ultracold atoms.

3.1 One-dimensional superlattices and the SSH model

We start with the simplest extension of a one-dimensional lattice, obtained by superimposing two standing waves of commensurate wavelengths. This 'superlattice' contains two

sites per unit cell. We first describe its realization and an application to the preparation of density patterns, before studying the band structure of the corresponding tight-binding model, the SSH model, and its topological properties.

3.1.1 Two-color superlattice potential

A one-dimensional superlattice is obtained by superimposing two standing waves of wavelengths λ_l (long lattice) and $\lambda_\mathrm{s} = \lambda_\mathrm{l}/2$ (short lattice), typically produced by two lasers of frequencies differing by a factor two and retro-reflected on the same mirror. Writing $k = 2\pi/\lambda_\mathrm{l}$, the potential reads

$$V(x) = V_\mathrm{l} \sin^2(kx) + V_\mathrm{s} \sin^2(2kx + \phi), \tag{3.1}$$

where V_l and V_s are the depths of the two lattices. The potential is periodic with the period

$$a = \frac{\pi}{k} = \frac{\lambda_\mathrm{l}}{2}, \tag{3.2}$$

and, for a short lattice deeper than the long one, each period contains two minima separated by approximately $a/2 = \lambda_\mathrm{s}/2$. The relative phase ϕ between the two standing waves, which can be tuned for instance by slightly changing the frequency of one of the lasers, controls the shape of the unit cell, as shown in Fig. 26:

- For $\phi = \pi/2$, the short-lattice term becomes $V_\mathrm{s} \cos^2(2kx)$, whose minima are located at $x = \pm a/4$, symmetrically around the minimum $x = 0$ of the long lattice. Both sites of the unit cell then have the same energy, but the barriers between them alternate: the barrier at $x = 0$ has a height V_s, while the barrier at $x = a/2$ reaches $V_\mathrm{l} + V_\mathrm{s}$. The superlattice then forms a chain of symmetric double wells, with alternating tunneling amplitudes. This configuration is the analog of the polyacetylene molecule, a chain of carbon atoms with alternating single and double bonds, which motivated the introduction of the SSH model [28].

- For $\phi = 0$, a minimum of the short lattice coincides with the minimum of the long lattice at $x = 0$, while the next one, at $x = a/2$, sits on a maximum of the long lattice. Neighbouring sites then have the same barrier height but alternating energies, with an energy offset $\simeq V_\mathrm{l}$ between the two sites of the unit cell.

Intermediate values of ϕ realize both an alternation of the tunneling amplitudes and of the on-site energies.

Application: imprinting and monitoring a density pattern. The possibility to switch dynamically between different superlattice configurations allows one to prepare non-equilibrium states with a well-defined density pattern, and to probe their evolution with a site-resolved readout. This strategy was used in Ref. [29] to study the relaxation of a strongly-interacting one-dimensional Bose gas, following the protocol shown in Fig. 27:

1. *Preparation.* Using a superlattice with staggered energy offsets, ^{87}Rb atoms are prepared in a period-two density wave $|\ldots, 1, 0, 1, 0, \ldots\rangle$, with one atom on every even site of the short lattice and empty odd sites, in an array of independent one-dimensional tubes.

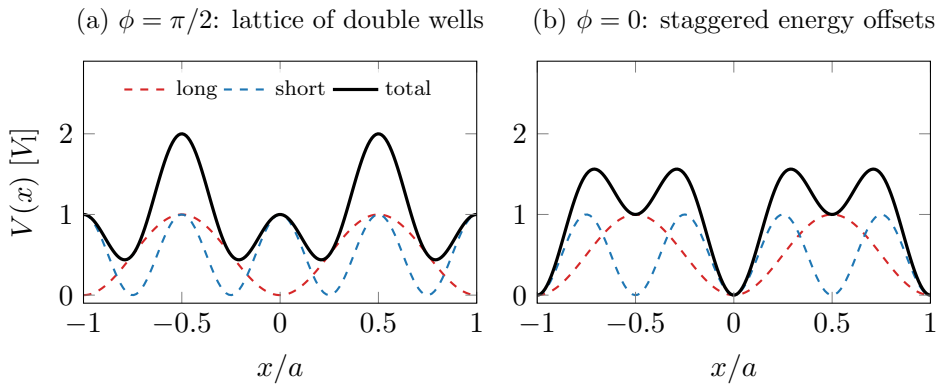


Figure 26: Superlattice potential (3.1) (black line), sum of a long lattice (red dashed line) and a short lattice (blue dashed line), plotted for $V_l = V_s$. (a) For $\phi = \pi/2$ one obtains a chain of symmetric double wells, with alternating barrier heights. (b) For $\phi = 0$ neighbouring sites have alternating energies.

2. *Evolution.* The long lattice is suddenly switched off, which leaves a simple lattice of depth adjusted to choose the ratio U/J. The density wave is not an eigenstate of the Bose-Hubbard Hamiltonian and evolves under the effect of tunneling and interactions.

3. *Readout.* After a variable evolution time, the superlattice is switched on again and used to map the populations of even and odd sites onto different Bloch bands, which are distinguished by a band-mapping measurement (see section 2). This gives the mean occupation n_{odd} of odd sites.

The evolution can be computed exactly in two limiting cases. For non-interacting bosons, each particle initially located on the site j_0 spreads independently. Solving the Schrödinger equation $\mathrm{i}\hbar\dot{c}_j = -J(c_{j+1} + c_{j-1})$ for the amplitude $c_j(t)$ on site j, with $c_j(0) = \delta_{j,j_0}$, one finds

$$c_j(t) = \mathrm{i}^{j-j_0} \mathcal{J}_{j-j_0}\left(\frac{2Jt}{\hbar}\right), \tag{3.3}$$

where $\mathcal{J}_m$ is the Bessel function of the first kind (as can be checked from the recurrence relation $2\mathcal{J}'_m = \mathcal{J}_{m-1} - \mathcal{J}_{m+1}$). Since the initial state is a Fock state, the mean densities originating from different initial sites simply add up, and the occupation of odd sites is

$$n_{\mathrm{odd}}(t) = \sum_{m \text{ odd}} \mathcal{J}_m^2\left(\frac{2Jt}{\hbar}\right) = \frac{1}{2}\left[1 - \mathcal{J}_0\left(\frac{4Jt}{\hbar}\right)\right], \tag{3.4}$$

where we used the identities $\sum_m \mathcal{J}_m^2(x) = 1$ and $\sum_m (-1)^m \mathcal{J}_m^2(x) = \mathcal{J}_0(2x)$. The same result holds for infinitely repulsive (hard-core) bosons, which can be mapped onto non-interacting fermions with the same density distribution. The odd-site occupation thus exhibits damped oscillations, with a first maximum at $4Jt/h \simeq 0.6$, and relaxes towards the homogeneous value $1/2$ on a timescale of a few tunneling times $\hbar/J$. For intermediate interactions no analytical solution is available, and the measurements were compared with numerical simulations of the Bose-Hubbard dynamics (time-dependent density-matrix renormalization group), without any adjustable parameter. As shown

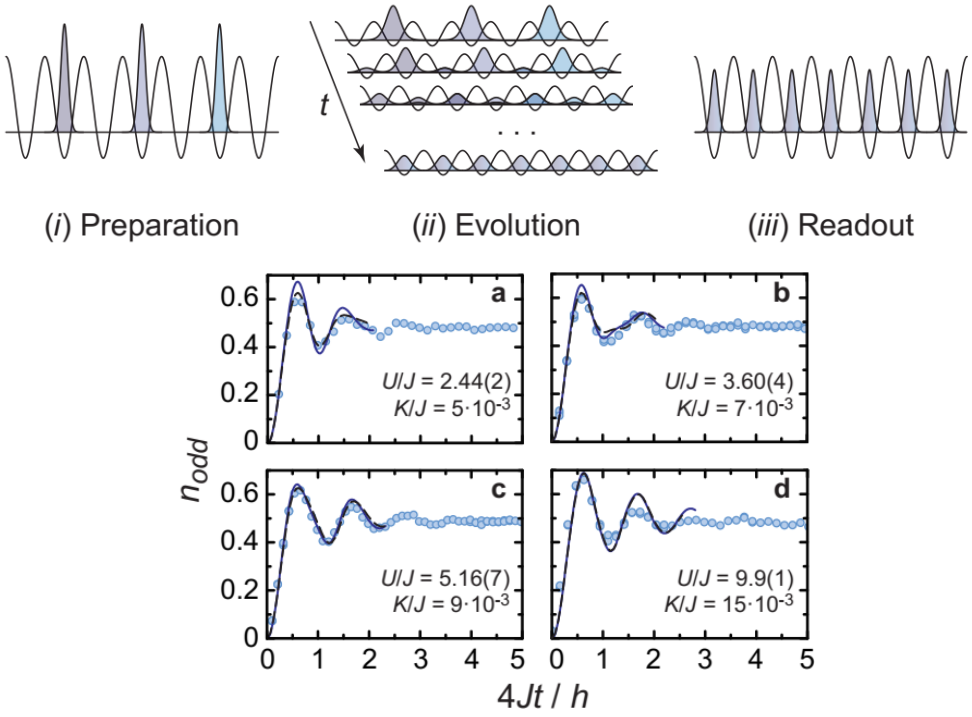


Figure 27: Top: principle of the experiment of Ref. [29], in which a superlattice is used to prepare a period-two density wave (i), let it evolve in a simple lattice (ii), and measure the occupations of even and odd sites (iii). Bottom: measured odd-site occupation $n_{\rm odd}$ as a function of time (in units of $h/4J$), for four values of U/J (K is the curvature of the harmonic trap). The lines are numerical simulations of the Bose-Hubbard dynamics without free parameters. Figures taken from Ref. [29].

in Fig. 27, the agreement is excellent at short times, while the experiment follows the dynamics up to longer times, beyond the reach of the numerical method because of the fast growth of entanglement. The relaxation of the local density towards a stationary value is a first illustration of the use of cold atoms in optical lattices as quantum simulators of out-of-equilibrium many-body dynamics.

3.1.2 Band structure of the SSH model

We now come back to the lattice of double wells ($\phi = \pi/2$), and describe it using a tight-binding model in its lowest band. Each unit cell j contains two sites, denoted A_j and B_j, as sketched in Fig. 28a. We denote J' the tunneling amplitude between the two sites of a unit cell (across the barrier of height $V_{\rm s}$) and J the amplitude between neighbouring unit cells (across the barrier of height $V_{\rm l} + V_{\rm s}$). The Hamiltonian

$$\hat{H} = -\sum_j \left(J'\, \hat{a}_j^\dagger \hat{b}_j + J\, \hat{b}_j^\dagger \hat{a}_{j+1} + \text{h.c.} \right), \tag{3.5}$$

where $\hat{a}_j$ and $\hat{b}_j$ annihilate a particle on the sites A_j and B_j, defines the SSH model [28]. The values of J and J' can be calculated from the Wannier functions of the double-well lattice as in section 2. In the following we treat the two amplitudes as independent positive parameters.

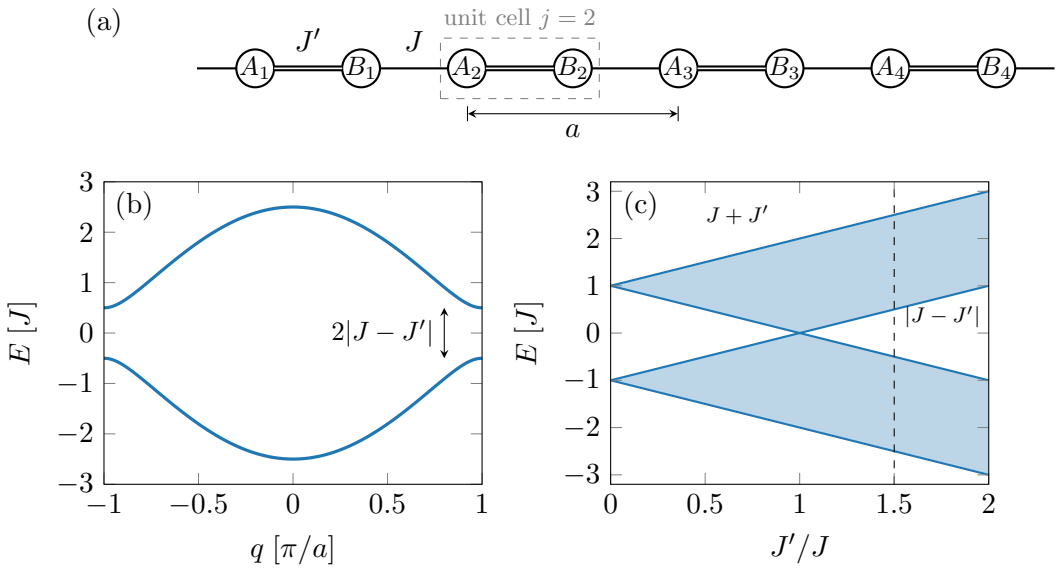


Figure 28: (a) SSH chain with two sites A_j and B_j per unit cell of length a, coupled by the intra-cell tunneling J' (double lines) and the inter-cell tunneling J (single lines). (b) Dispersion relation (3.8) for $J' = 1.5\,J$. (c) Energy spectrum as a function of J'/J: the two bands (shaded areas) extend between $|J - J'|$ and $J + J'$ in absolute value. The gap closes for $J' = J$. The dashed line indicates the case $J' = 1.5\,J$ shown in (b).

Bloch states. The Hamiltonian is invariant under translations by the lattice period a. Following the Bloch theorem we look for eigenstates of the form

$$|\psi_q\rangle = \sum_j \mathrm{e}^{\mathrm{i}qja}\left(\alpha_q|A_j\rangle + \beta_q|B_j\rangle\right), \tag{3.6}$$

with a quasi-momentum q in the Brillouin zone $[-\pi/a, \pi/a[$, and where the amplitudes α_q and β_q do not depend on the cell index j. Applying the Hamiltonian (3.5), the amplitude on site A_j receives a contribution $-J'\beta_q\mathrm{e}^{\mathrm{i}qja}$ from B_j and $-J\beta_q\mathrm{e}^{\mathrm{i}q(j-1)a}$ from B_{j-1}, while the amplitude on B_j receives $-J'\alpha_q\mathrm{e}^{\mathrm{i}qja}$ from A_j and $-J\alpha_q\mathrm{e}^{\mathrm{i}q(j+1)a}$ from A_{j+1}. The Schrödinger equation thus reduces to the 2×2 eigenvalue problem

$$H_q\begin{pmatrix}\alpha_q\\ \beta_q\end{pmatrix} = E_q\begin{pmatrix}\alpha_q\\ \beta_q\end{pmatrix}, \qquad H_q = -\begin{pmatrix}0 & h_q^*\\ h_q & 0\end{pmatrix}, \qquad h_q = J' + J\mathrm{e}^{\mathrm{i}qa}. \tag{3.7}$$

The eigenvalues $E_q = \pm|h_q|$ give the dispersion relation of the two bands

$$E_q^{(\pm)} = \pm\sqrt{J^2 + J'^2 + 2JJ'\cos(qa)}. \tag{3.8}$$

The band structure is shown in Fig. 28b for $J' = 1.5\,J$. The spectrum is symmetric with respect to $E = 0$. The two bands have their maximal splitting $2(J + J')$ at $q = 0$, and are separated by a gap

$$E_{\mathrm{gap}} = 2|J - J'|, \tag{3.9}$$

reached at the edge of the Brillouin zone $q = \pm\pi/a$. As shown in Fig. 28c, the gap closes only for $J' = J$, where one recovers a simple lattice of period $a/2$ with a single cosine

band, artificially folded into the Brillouin zone of the superlattice. The two gapped regimes $J' < J$ and $J' > J$ seem very similar: the band structure is invariant upon the exchange of J and J'. We will see that they nevertheless differ by a topological property of their Bloch states.

The symmetry of the spectrum has a simple origin. The Hamiltonian only couples A sites to B sites, so that the operator σ_z (which changes the sign of the B amplitudes) anticommutes with H_q: $\sigma_z H_q \sigma_z = -H_q$. This *chiral* (or sublattice) symmetry maps each eigenstate of energy E onto an eigenstate of energy $-E$. It is broken by an energy offset between the A and B sites, which occurs in the superlattice (3.1) as soon as $\phi \neq \pi/2$.

3.1.3 Zak phase and band topology

Bloch eigenstates. Writing $h_q = |h_q| \mathrm{e}^{\mathrm{i}\phi_q}$, the eigenstate of the lower band $E_q^{(-)} = -|h_q|$ satisfies $-h_q^* \beta_q = -|h_q| \alpha_q$, hence $\beta_q = \mathrm{e}^{\mathrm{i}\phi_q} \alpha_q$. The normalized lower-band eigenvector reads

$$|u_q\rangle = \frac{1}{\sqrt{2}} \begin{pmatrix} 1 \\ \mathrm{e}^{\mathrm{i}\phi_q} \end{pmatrix}, \qquad \mathrm{e}^{\mathrm{i}\phi_q} = \frac{J' + J\mathrm{e}^{\mathrm{i}qa}}{|J' + J\mathrm{e}^{\mathrm{i}qa}|}. \tag{3.10}$$

(The upper-band eigenvector is $(1, -\mathrm{e}^{\mathrm{i}\phi_q})/\sqrt{2}$.) The two components have equal weights, as expected from the chiral symmetry: all the information on the Bloch state is contained in the relative phase ϕ_q, which is well defined over the whole Brillouin zone as long as $h_q \neq 0$, i.e. except for $J' = J$, where the gap closes at $q = \pm\pi/a$.

When q spans the Brillouin zone, the complex number $h_q = J' + J\mathrm{e}^{\mathrm{i}qa}$ describes a circle of radius J centered on J' in the complex plane. Two cases must be distinguished:

- For $J' > J$, the circle does not enclose the origin. The phase ϕ_q oscillates around zero, with an amplitude $\arcsin(J/J')$, and returns to its initial value without winding.
- For $J' < J$, the circle encloses the origin. The phase ϕ_q increases by 2π when q spans the Brillouin zone: it winds once around the unit circle.

These two behaviours are illustrated in Fig. 29a. The winding number

$$W = \frac{1}{2\pi} \int_{-\pi/a}^{\pi/a} \frac{\mathrm{d}\phi_q}{\mathrm{d}q} \, \mathrm{d}q \in \{0, 1\} \tag{3.11}$$

is an integer, which cannot change under a continuous deformation of the parameters unless h_q vanishes for some q, i.e. unless the gap closes. It is thus a topological invariant, which distinguishes the two gapped phases $J' < J$ ($W = 1$) and $J' > J$ ($W = 0$).

Berry connection and Zak phase. The winding of ϕ_q has a direct physical meaning in terms of the geometric (Berry) phase accumulated by a Bloch state transported adiabatically across the Brillouin zone. When the quasi-momentum q varies slowly in time, for instance under the action of a constant force (Bloch oscillations, see section 2), a particle initially in the Bloch state $|u_q\rangle$ follows the lower band adiabatically, and acquires, besides the dynamical phase $-\int E_q \, \mathrm{d}t/\hbar$, a geometric phase $\int \mathcal{A}(q) \, \mathrm{d}q$ involving the Berry connection

$$\mathcal{A}(q) = \mathrm{i}\langle u_q | \partial_q u_q \rangle. \tag{3.12}$$

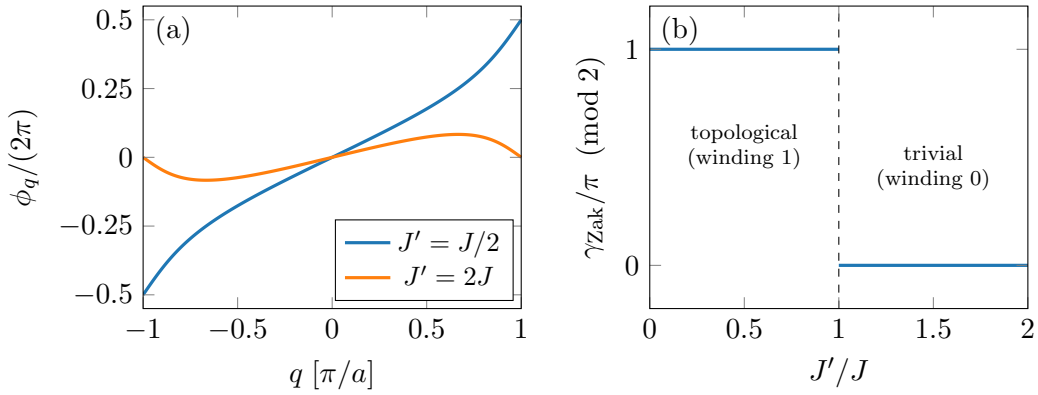


Figure 29: (a) Relative phase ϕ_q between the two components of the lower-band Bloch state (3.10), for $J' = J/2$ (blue line) and $J' = 2J$ (orange line). In the first case ϕ_q winds by 2π across the Brillouin zone (the jump at $q = \pm\pi/a$ is a jump by 2π), while in the second case it oscillates without winding. (b) Zak phase of the lower band versus J'/J, equal to π (winding number $W = 1$) for $J' < J$ and to 0 ($W = 0$) for $J' > J$.

The Berry phase accumulated over the whole Brillouin zone is called the Zak phase [30, 31],

$$\gamma_{\mathrm{Zak}} = \int_{-\pi/a}^{\pi/a} \mathcal{A}(q)\,\mathrm{d}q. \tag{3.13}$$

For the SSH eigenstates (3.10) we get $\langle u_q|\partial_q u_q\rangle = \frac{\mathrm{i}}{2}\,\partial_q\phi_q$, hence $\mathcal{A}(q) = -\frac{1}{2}\partial_q\phi_q$ and

$$\gamma_{\mathrm{Zak}} = -\frac{1}{2}\int_{-\pi/a}^{\pi/a} \frac{\mathrm{d}\phi_q}{\mathrm{d}q}\,\mathrm{d}q = -\pi W \pmod{2\pi}. \tag{3.14}$$

The Zak phase is thus quantized to π in the topological phase $J' < J$, and to 0 in the trivial phase $J' > J$, as shown in Fig. 29b. We checked this result with a gauge-invariant numerical evaluation of the discretized Berry phase.

Two remarks are in order. First, the quantization of the Zak phase relies on the chiral symmetry, which constrains the vector $(\mathrm{Re}\,h_q, \mathrm{Im}\,h_q)$ to the plane and makes the winding well defined. Adding an energy offset between the A and B sites allows one to connect continuously the two phases without closing the gap, the Zak phase taking then arbitrary values. Second, the Zak phase depends on the choice of the unit cell: had we paired the sites as (B_j, A_{j+1}), the roles of J and J' would have been exchanged, and so would the values of γ_{Zak}. Only the difference of Zak phases between the two dimerizations, for a given choice of unit cell, is a physical observable (it is related to the difference of electric polarization between the two configurations). This is precisely the quantity measured in the experiment described below.

3.1.4 Measuring the Zak phase

The Zak phase was measured with ultracold bosonic atoms in an optical superlattice realizing the SSH model [32]. The measurement relies on an interferometric sequence combining Bloch oscillations and Ramsey interferometry between two internal states $|\uparrow\rangle$ and $|\downarrow\rangle$ of the atoms, chosen with opposite magnetic moments (see Fig. 30):

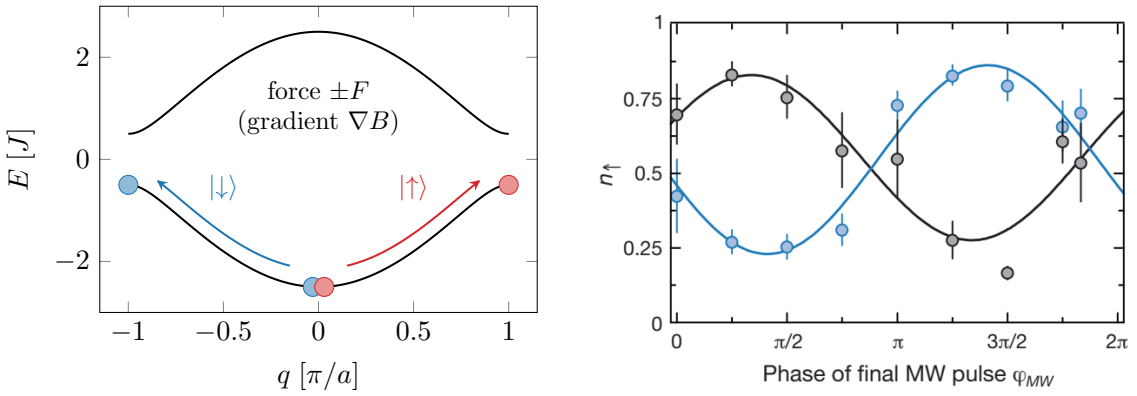


Figure 30: Left: principle of the Zak-phase measurement. After a $\pi/2$ pulse, the two spin components, subjected to opposite forces, move in opposite directions in the lower band and reach the two edges of the Brillouin zone, where a second $\pi/2$ pulse makes them interfere. Right: population $n_\uparrow$ measured at the end of the sequence as a function of the phase φ_{MW} of the second pulse, for the two dimerizations of the superlattice (black and blue). The phase shift between the two fringes gives the Zak phase difference $\delta\gamma_{\mathrm{Zak}} = 0.97(2)\pi$. Data taken from Ref. [32].

1. The atoms are initially prepared in the state $|\uparrow\rangle$, in the lower band, at quasi-momentum $q = 0$.
2. A microwave $\pi/2$ pulse creates the superposition $(|\uparrow\rangle + |\downarrow\rangle)/\sqrt{2}$.
3. A magnetic field gradient is applied, which exerts opposite forces $\pm F$ on the two spin components. They undergo Bloch oscillations in opposite directions, and reach after half a Bloch period the two edges $q = +\pi/a$ and $q = -\pi/a$ of the Brillouin zone, which correspond to the same physical quasi-momentum. Altogether, the two components have explored the whole Brillouin zone.
4. A second $\pi/2$ pulse with a variable phase φ_{MW} closes the interferometer, and the population in $|\uparrow\rangle$ is measured.

Since the dispersion relation is even, $E_q = E_{-q}$, the two paths accumulate the same dynamical phase. The phase difference between the two arms contains the difference of geometric phases $\int_{-\pi/a}^{0} \mathcal{A}\,\mathrm{d}q + \int_{0}^{\pi/a} \mathcal{A}\,\mathrm{d}q = \gamma_{\mathrm{Zak}}$, together with a Zeeman phase due to the magnetic field. The latter was eliminated using spin-echo techniques, and by comparing two measurements performed in the two dimerized configurations $J' > J$ and $J' < J$, which differ only by their Zak phase. The two resulting Ramsey fringes, shown in Fig. 30, are shifted by

$$\delta\gamma_{\mathrm{Zak}} = 0.97(2)\,\pi, \tag{3.15}$$

in agreement with the expected value π. This experiment constitutes a direct measurement of a topological invariant of a Bloch band.

3.1.5 Topological edge modes

A remarkable consequence of a non-trivial band topology is the existence of states localized at the boundaries of the system, whose properties are protected by the

topological invariant of the bulk (bulk-edge correspondence). We illustrate this on the SSH chain, which we cut to obtain a semi-infinite geometry starting with the site A_1, the first bond being an intra-cell bond J' (see Fig. 31a). We write a general state as $|\psi\rangle = \sum_{j\geq 1}(a_j|A_j\rangle + b_j|B_j\rangle)$. The Schrödinger equation reads

$$E\,a_j = -J'b_j - J\,b_{j-1}, \qquad (b_0 \equiv 0), \tag{3.16}$$

$$E\,b_j = -J'a_j - J\,a_{j+1}. \tag{3.17}$$

Bulk states. For an energy E belonging to the spectrum (3.8) of the infinite chain, there exist two degenerate Bloch states $|\psi_q\rangle$ and $|\psi_{-q}\rangle$, since $E_q = E_{-q}$. They can be combined to form a standing wave satisfying the boundary condition $b_0 = 0$ imposed by the edge. These states remain extended in the bulk.

Zero-energy edge mode. The semi-infinite chain also supports an additional state at $E = 0$. For $E = 0$, (3.16) gives $J'b_1 = 0$ for $j = 1$, and then $b_j = -(J/J')b_{j-1} = 0$ by recurrence: the state has no amplitude on the B sublattice. The equation (3.17) then gives the recurrence relation $a_{j+1} = -(J'/J)\,a_j$, hence

$$a_j = a_1\left(-\frac{J'}{J}\right)^{j-1}, \qquad b_j = 0. \tag{3.18}$$

This state is normalizable only for $J' < J$, i.e. in the topological phase with a Zak phase π. Its amplitude decays exponentially away from the edge,

$$|a_j| = |a_1|\,\mathrm{e}^{-(j-1)a/\xi}, \qquad \xi = \frac{a}{\ln(J/J')}, \tag{3.19}$$

over a localization length ξ that diverges when approaching the gap closing $J' \to J$. For $J' = J/2$, the normalized amplitudes $a_j = \frac{\sqrt{3}}{2}(-1/2)^{j-1}$ are shown in Fig. 31b.

The energy of this mode is pinned at the center of the gap. Indeed, its existence relies only on the chiral symmetry, which forbids any amplitude on the B sublattice for a zero-energy state localized on the A end: perturbations respecting the chiral symmetry (for instance disorder in the tunneling amplitudes) cannot shift its energy away from zero as long as the bulk gap remains open. In a finite chain with two edges, the two edge modes (one on each end) hybridize through the bulk, which splits their energies by an amount exponentially small in L/ξ, where L is the chain length. This is illustrated in Fig. 31c, where we computed numerically the spectrum of an open chain of 20 unit cells: two quasi-degenerate states at $E \simeq 0$ appear in the gap for $J' < J$, while no such state exists for $J' > J$. The correspondence between the bulk winding number and the number of zero-energy edge states is an example of the bulk-edge correspondence, a general property of topological band structures.

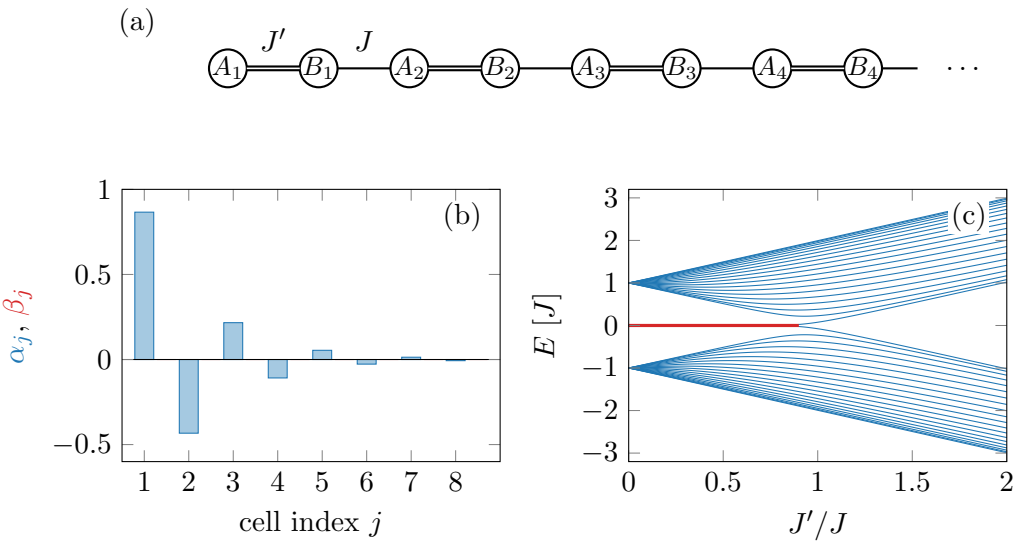


Figure 31: (a) Semi-infinite SSH chain ending with a weak intra-cell bond $J' < J$. (b) Amplitudes $\alpha_j = a_j$ (blue) and $\beta_j = b_j = 0$ (red) of the zero-energy edge mode for $J' = J/2$. (c) Spectrum of an open chain of 20 unit cells as a function of J'/J. Two edge modes appear at $E \simeq 0$ for $J' < J$ (red line), in the gap separating the bulk bands.

3.2 Two-dimensional lattices: Dirac points and quantum Hall bands

We now turn to two-dimensional lattices. We first consider a honeycomb lattice, which exhibits Dirac points similar to those of graphene, and show how they can be revealed using Bloch oscillations. We then explain how complex tunneling amplitudes can be engineered in optical lattices, which gives access to the physics of charged particles in a magnetic field, and in particular to the Hofstadter model and its topological bands characterized by Chern numbers.

3.2.1 Graphene-like honeycomb lattice

Tight-binding model. The honeycomb lattice, which describes the arrangement of carbon atoms in graphene, is a triangular Bravais lattice with two sites A and B per unit cell. Each A site is coupled to three neighbouring B sites located at the relative positions $\boldsymbol{\delta}_1$, $\boldsymbol{\delta}_2$, $\boldsymbol{\delta}_3$. Allowing for different tunneling amplitudes J_1, J_2, J_3 along the three bonds and for an energy offset Δ between the two sublattices, we look for Bloch states $\sum_{\mathbf{R}} \mathrm{e}^{\mathrm{i}\mathbf{q}\cdot\mathbf{R}}(\alpha_{\mathbf{q}}|A_{\mathbf{R}}\rangle + \beta_{\mathbf{q}}|B_{\mathbf{R}}\rangle)$, where $\mathbf{R}$ labels the unit cells. As for the SSH model, the Schrödinger equation reduces to the 2×2 problem

$$H_{\mathbf{q}} = \begin{pmatrix} \Delta/2 & -f_{\mathbf{q}}^* \\ -f_{\mathbf{q}} & -\Delta/2 \end{pmatrix}, \qquad f_{\mathbf{q}} = \sum_{i=1}^{3} J_i \, \mathrm{e}^{\mathrm{i}\mathbf{q}\cdot\boldsymbol{\delta}_i}, \tag{3.20}$$

where the quasi-momentum phases are written using the bond vectors, a choice that only redefines the phase of the B amplitude. The dispersion relation reads

$$E_{\mathbf{q}}^{(\pm)} = \pm\sqrt{\frac{\Delta^2}{4} + |f_{\mathbf{q}}|^2}. \tag{3.21}$$

Dirac points. For $\Delta = 0$, the two bands touch at the points where $f_{\mathbf{q}} = 0$. This condition requires the three complex numbers $J_i e^{i\mathbf{q}\cdot\boldsymbol{\delta}_i}$ to form a closed triangle, which is possible only if the amplitudes satisfy the triangle inequality $|J_1 - J_2| \leq J_3 \leq J_1 + J_2$. In the isotropic case $J_1 = J_2 = J_3 = J$, the band touching occurs at the two inequivalent corners $\mathbf{K}$ and $\mathbf{K}'$ of the hexagonal Brillouin zone. Expanding $f_{\mathbf{q}}$ to first order around these points, one finds a conical dispersion

$$E^{(\pm)}_{\mathbf{K}+\delta\mathbf{q}} \simeq \pm\hbar v_{\mathrm{D}} |\delta\mathbf{q}|, \qquad v_{\mathrm{D}} = \frac{3Jb}{2\hbar}, \tag{3.22}$$

where b is the distance between neighbouring sites. Near these Dirac points, the low-energy excitations behave as massless relativistic particles described by a two-dimensional Dirac equation, the sublattice index playing the role of a pseudo-spin. Each Dirac point carries a Berry phase $\pm\pi$ for a loop encircling it. An offset $\Delta \neq 0$, which breaks the inversion symmetry between the two sublattices, opens a gap Δ at the Dirac points (the Dirac fermions acquire a mass). When the anisotropy of the tunneling amplitudes is increased, the two Dirac points move in the Brillouin zone, and they merge and annihilate when the triangle inequality becomes an equality: beyond this point a gap opens, even for $\Delta = 0$.

Realization with cold atoms. A tunable honeycomb lattice was realized in Ref. [33] with three retro-reflected laser beams, as shown in Fig. 32. Two of them (X and Y) interfere and create a two-dimensional checkerboard pattern, while the third one ($\bar{X}$), slightly detuned by δ from X so that it does not interfere with the others, adds an independent standing wave along x. The resulting 'brick-wall' lattice has the same connectivity as the honeycomb lattice, with two sites A and B per unit cell. The relative phase θ between the X and $\bar{X}$ standing waves, controlled via the detuning δ, sets the energy offset Δ between the two sublattices, which vanishes for $\theta = \pi$. The relative intensities of the beams control the tunneling anisotropy, and hence the positions of the Dirac points. The experiment used a spin-polarized, hence non-interacting, Fermi gas of ^{40}K atoms.

3.2.2 Probing Dirac points using Bloch oscillations

The Dirac points were probed by subjecting the atoms to a constant force $\mathbf{F}$ (a magnetic field gradient), which makes their quasi-momentum evolve as $\hbar\dot{\mathbf{q}} = \mathbf{F}$, as discussed in section 2. After a full Bloch period T_{B}, the quasi-momentum has crossed the Brillouin zone and the population of the second band is measured using band mapping. Two kinds of trajectories can be distinguished (see Fig. 33):

- Atoms whose trajectory passes through (or very close to) a Dirac point cannot follow the lower band adiabatically, since the gap vanishes: they cross the cone and are transferred to the second band.
- Atoms passing far from the Dirac points stay in the lower band and undergo Bragg reflections at the edges of the Brillouin zone, as in a usual Bloch oscillation.

The transfer probability is quantitatively described by the Landau-Zener formula. For a trajectory passing at a distance $\delta q_\perp$ from the Dirac point, the energy difference between the two bands reaches its minimum $E_{\mathrm{G}} = \sqrt{\Delta^2 + 4\hbar^2 v_{\mathrm{D}}^2 \delta q_\perp^2}$, while far from

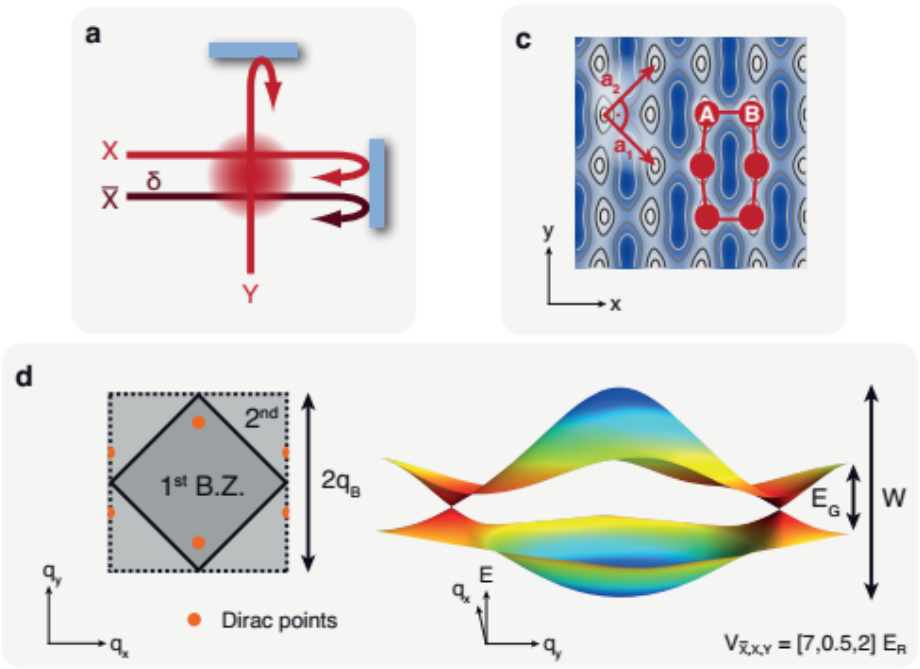


Figure 32: Honeycomb optical lattice of Ref. [33]. (a) Laser configuration: the beams X and Y interfere, while the beam $\bar{X}$, detuned by δ, creates an additional standing wave along x. (c) Resulting potential (brick-wall geometry, with sublattices A and B and primitive vectors $\mathbf{a}_1$, $\mathbf{a}_2$). (d) Brillouin zones and band structure computed for the lattice depths indicated, showing two Dirac points (orange dots). Figure taken from Ref. [33].

the point it varies at the rate $\mathrm{d}(E^{(+)} - E^{(-)})/\mathrm{d}t = 2v_\mathrm{D}F$. The Landau-Zener formula $P = \exp[-\pi E_\mathrm{G}^2/(2\hbar\,\mathrm{d}(E^{(+)} - E^{(-)})/\mathrm{d}t)]$ then gives the transfer probability

$$P = \exp\left(-\frac{\pi E_\mathrm{G}^2}{4\hbar v_\mathrm{D} F}\right). \tag{3.23}$$

The transferred fraction thus depends on the minimal gap encountered along the trajectories: it is maximal when the Dirac points are gapless ($\Delta = 0$), and decreases when an energy offset opens a gap.

This is what was observed in Ref. [33], by measuring the transferred fraction ξ as a function of the detuning δ, which controls the phase θ and hence the sublattice offset Δ (Fig. 33, bottom). The transferred fraction is peaked around $\theta = \pi$, where $\Delta = 0$ and the Dirac cones are gapless, and decreases on both sides as a gap Δ opens (for instance $\Delta/h = 390\,\mathrm{Hz}$ on the right of the resonance). The same technique allowed the authors to follow the motion of the Dirac points when changing the tunneling anisotropy, and to observe their merging, associated with the opening of a gap.

3.2.3 Optical lattices with complex tunneling amplitudes

Peierls phases and magnetic flux. For a charged particle (charge e) moving in a lattice in the presence of a magnetic field $\mathbf{B} = \boldsymbol{\nabla} \times \mathbf{A}$, the tight-binding Hamiltonian is modified by the Peierls substitution, which attaches a phase to the tunneling amplitudes,

$$-J\,\hat{a}^\dagger_{\mathbf{R}'}\hat{a}_{\mathbf{R}} \;\longrightarrow\; -J\,\mathrm{e}^{\mathrm{i}\theta_{\mathbf{R}'\mathbf{R}}}\,\hat{a}^\dagger_{\mathbf{R}'}\hat{a}_{\mathbf{R}}, \qquad \theta_{\mathbf{R}'\mathbf{R}} = \frac{e}{\hbar}\int_{\mathbf{R}}^{\mathbf{R}'} \mathbf{A}\cdot\mathrm{d}\boldsymbol{\ell}. \tag{3.24}$$

The individual phases depend on the choice of gauge, but their sum around a closed loop is gauge invariant. Around a plaquette of a square lattice of spacing d it gives

$$\Phi \equiv \sum_{\text{plaquette}} \theta = 2\pi\,\frac{Bd^2}{h/e}, \tag{3.25}$$

i.e. 2π times the magnetic flux through the plaquette in units of the flux quantum h/e. In a solid, reaching a flux quantum per plaquette with $d \sim 3\,\text{Å}$ would require a magnetic field $h/(ed^2) \sim 5 \times 10^4\,\mathrm{T}$, far beyond what can be produced in a laboratory. With neutral atoms there is no Lorentz force at all, but the same physics can be reproduced by engineering complex tunneling amplitudes directly [34]. Since the Peierls phases are then imposed by laser fields, fluxes of the order of π per plaquette are within reach.

Laser-assisted tunneling. A standard method to imprint Peierls phases proceeds in two steps (see Fig. 34):

1. Tunneling between neighbouring sites is first suppressed by an energy offset $\Delta \gg J$ (created by a superlattice or a potential gradient).

2. Tunneling is then restored by a modulation of the energy offset at the resonant frequency $\omega = \Delta/\hbar$, and the phase of the modulation is transferred to the effective tunneling amplitude.

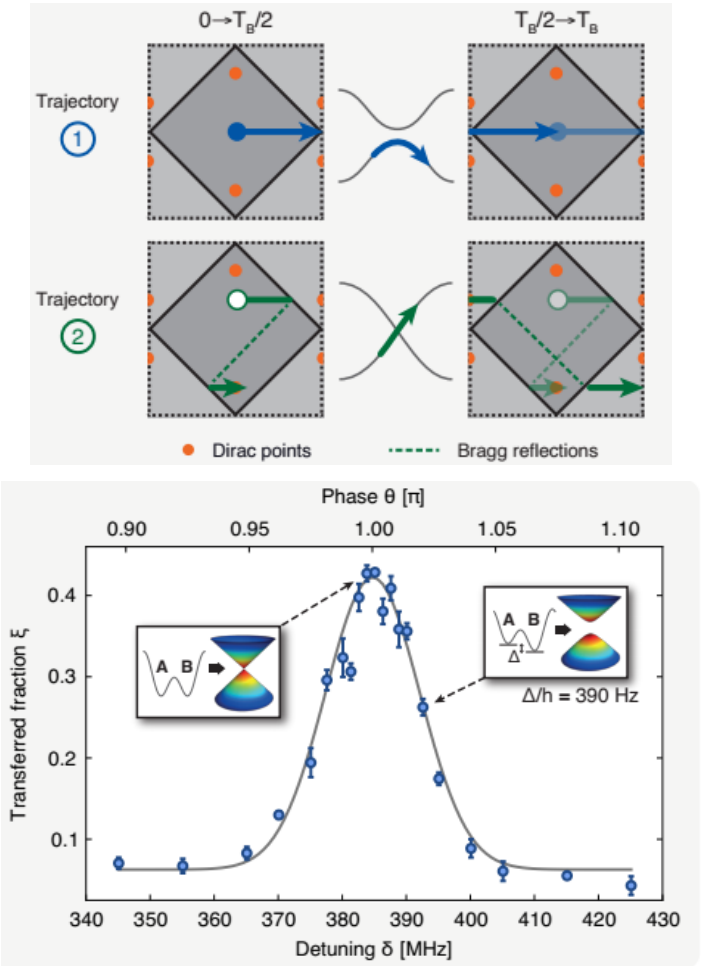


Figure 33: Top: Bloch-oscillation trajectories in the Brillouin zone of the honeycomb lattice. Trajectory 1 crosses a Dirac point and leads to a transfer to the second band. Trajectory 2 avoids the Dirac points and undergoes Bragg reflections, the atoms remaining in the lower band. Bottom: fraction ξ of atoms transferred to the second band as a function of the detuning δ (bottom axis), which sets the relative phase θ (top axis). The maximum around $\theta = \pi$ corresponds to gapless Dirac cones ($\Delta = 0$). Figures taken from Ref. [33].

To show this, we consider two sites coupled by the tunneling J, the second site having a modulated energy $\varepsilon_2(t) = \Delta + \delta\cos(\omega t + \varphi)$:

$$\hat{H}(t) = -J\left(\hat{a}_2^\dagger \hat{a}_1 + \hat{a}_1^\dagger \hat{a}_2\right) + \varepsilon_2(t)\,\hat{n}_2. \tag{3.26}$$

We eliminate the on-site energy with the time-dependent unitary transformation $\hat{U}(t) = \exp[\mathrm{i}\vartheta(t)\hat{n}_2]$, with $\hbar\dot{\vartheta} = \varepsilon_2(t)$, i.e.

$$\vartheta(t) = \frac{\Delta t}{\hbar} + z\sin(\omega t + \varphi), \qquad z = \frac{\delta}{\hbar\omega}, \tag{3.27}$$

up to an irrelevant constant. The transformed state $\hat{U}|\psi\rangle$ evolves with the Hamiltonian $\hat{U}\hat{H}\hat{U}^\dagger + \mathrm{i}\hbar(\partial_t\hat{U})\hat{U}^\dagger$. Using $\hat{U}\hat{a}_2^\dagger\hat{U}^\dagger = \mathrm{e}^{\mathrm{i}\vartheta}\hat{a}_2^\dagger$ and $\mathrm{i}\hbar(\partial_t\hat{U})\hat{U}^\dagger = -\varepsilon_2(t)\hat{n}_2$, it reads

$$\hat{H}'(t) = -J\left(\mathrm{e}^{\mathrm{i}\vartheta(t)}\,\hat{a}_2^\dagger\hat{a}_1 + \mathrm{h.c.}\right). \tag{3.28}$$

We then use the Jacobi-Anger expansion $\mathrm{e}^{\mathrm{i}z\sin x} = \sum_n \mathcal{J}_n(z)\mathrm{e}^{\mathrm{i}nx}$, which gives

$$\mathrm{e}^{\mathrm{i}\vartheta(t)} = \sum_{n=-\infty}^{+\infty} \mathcal{J}_n(z)\,\mathrm{e}^{\mathrm{i}n\varphi}\,\mathrm{e}^{\mathrm{i}(\Delta/\hbar + n\omega)t}. \tag{3.29}$$

For a resonant modulation $\hbar\omega = \Delta$, the term $n = -1$ is time independent, while all other terms oscillate at multiples of ω. In the regime $J \ll \hbar\omega$, these fast oscillating terms average out (rotating-wave approximation), and we obtain, using $\mathcal{J}_{-1} = -\mathcal{J}_1$, the effective Hamiltonian

$$\hat{H}_{\text{eff}} = -J_{\text{eff}}\left(\mathrm{e}^{\mathrm{i}\theta}\,\hat{a}_2^\dagger\hat{a}_1 + \mathrm{h.c.}\right), \qquad J_{\text{eff}} = J\,\mathcal{J}_1\!\left(\frac{\delta}{\Delta}\right), \qquad \theta = \pi - \varphi. \tag{3.30}$$

The tunneling is restored with a reduced amplitude ($J_{\text{eff}} \simeq J\delta/2\Delta$ for a weak modulation, and at most $0.58\,J$), and with a complex phase directly set by the phase of the modulation.

Spatially varying Peierls phases. In practice the modulation is created by a pair of laser beams (with a frequency difference ω and a wave-vector difference $\delta\mathbf{k}$) producing a moving interference pattern $\propto \cos(\delta\mathbf{k}\cdot\mathbf{r} - \omega t)$. What matters is the difference between the modulations of the two sites of a bond, whose phase depends on the position of the bond, $\varphi = -\delta\mathbf{k}\cdot\mathbf{R}$ up to a constant, and so does the Peierls phase. If the tunneling along x is laser-assisted while the tunneling along y is a usual one, a component of $\delta\mathbf{k}$ along y makes the Peierls phase of x bonds vary from one row to the next, leading to a non-zero flux $\Phi = \delta k_y d$ per plaquette (mod 2π). This technique was used to realize staggered fluxes [35] (see Fig. 34) and then uniform fluxes, implementing the Hofstadter model [36, 37].

3.2.4 Hofstadter model and quantum Hall effect

Hofstadter model. We consider a square lattice of spacing d with a uniform flux $\Phi = 2\pi\alpha$ per plaquette. In the Landau gauge, the Peierls phases are carried by the bonds along x and increase linearly with the row index n, and the Hamiltonian reads

$$\hat{H} = -\sum_{m,n}\left(K\,\mathrm{e}^{-\mathrm{i}2\pi\alpha n}\,\hat{a}_{m+1,n}^\dagger\hat{a}_{m,n} + J\,\hat{a}_{m,n+1}^\dagger\hat{a}_{m,n} + \mathrm{h.c.}\right), \tag{3.31}$$

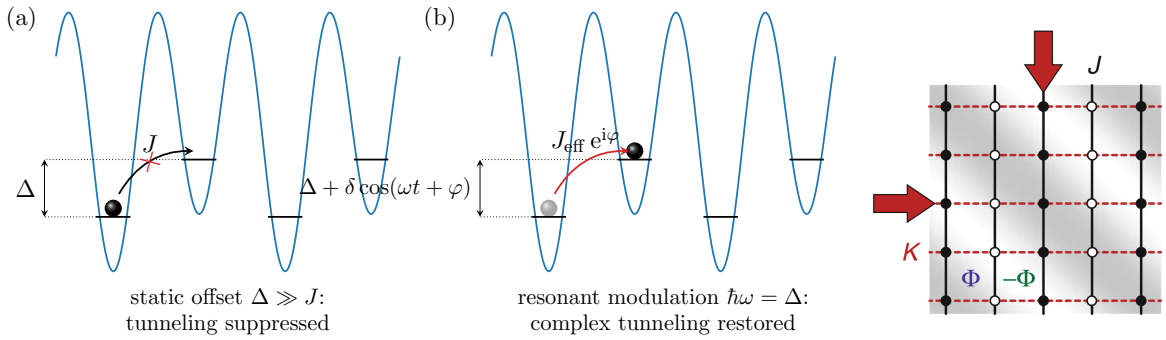


Figure 34: Laser-assisted tunneling. (a) A static energy offset $\Delta \gg J$ between neighbouring sites suppresses tunneling. (b) A modulation of the offset at the resonant frequency $\omega = \Delta/\hbar$ restores tunneling, with an effective amplitude J_{eff} and a phase set by the modulation phase φ, see (3.30). Right: implementation of Ref. [35], where two running-wave beams (red arrows) induce laser-assisted tunneling K along x in a lattice with staggered energy offsets (black and white sites), while tunneling J along y is unaffected. The resulting Peierls phases produce a staggered flux $\pm\Phi$ through neighbouring plaquettes. Right figure taken from Ref. [35].

where (m, n) label the sites along x and y, and K and J are the tunneling amplitudes along the two directions. One checks that the sum of the phases around each plaquette, oriented counterclockwise, is $2\pi\alpha$. The Hamiltonian is invariant under translations along x, and we look for solutions of the form $\psi_{m,n} = \mathrm{e}^{\mathrm{i}q_x md}\psi_n$, which leads to the Harper equation

$$E\,\psi_n = -2K\cos(q_x d + 2\pi\alpha n)\,\psi_n - J\,(\psi_{n+1} + \psi_{n-1})\,. \tag{3.32}$$

For a rational flux $\alpha = p/s$ (with p and s coprime integers), the Harper equation is periodic in n with period s. The magnetic unit cell then contains s sites, the magnetic Brillouin zone is reduced by a factor s, and the lowest band of the lattice splits into s sub-bands. The spectrum, computed numerically in Fig. 35 as a function of α for $K = J$, forms a fractal structure known as the Hofstadter butterfly [38]. In the limit of small flux $\alpha \ll 1$, the bands become very flat near the bottom of the spectrum, and reduce to the Landau levels of a particle of effective mass $m^* = \hbar^2/(2Jd^2)$ in a magnetic field, of cyclotron energy $\hbar\omega_c = 4\pi\alpha J$.

Berry curvature and Chern number. As for the SSH model, the Bloch states $|u_n(\mathbf{q})\rangle$ of each sub-band n define a Berry connection $\boldsymbol{\mathcal{A}}_n(\mathbf{q}) = \mathrm{i}\langle u_n|\boldsymbol{\nabla}_{\mathbf{q}} u_n\rangle$, and in two dimensions a Berry curvature

$$\Omega_n(\mathbf{q}) = \partial_{q_x}\mathcal{A}_{n,y} - \partial_{q_y}\mathcal{A}_{n,x} = \mathrm{i}\left(\langle\partial_{q_x}u_n|\partial_{q_y}u_n\rangle - \langle\partial_{q_y}u_n|\partial_{q_x}u_n\rangle\right). \tag{3.33}$$

The integral of the Berry curvature over the (magnetic) Brillouin zone, which has the topology of a torus, is quantized:

$$C_n = \frac{1}{2\pi}\int_{\text{MBZ}} \Omega_n(\mathbf{q})\,\mathrm{d}^2q \in \mathbb{Z}. \tag{3.34}$$

The integer C_n is the Chern number of the band. Like the winding number of the SSH model, it cannot change unless the band touches another band. Thouless, Kohmoto,

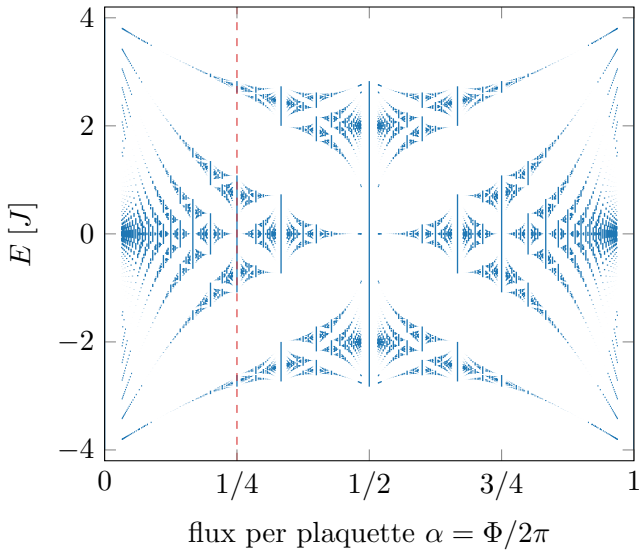


Figure 35: Hofstadter butterfly: energy bands of the Hofstadter model (3.31) with $K = J$, as a function of the flux per plaquette $\alpha = \Phi/2\pi$, computed for all rational values $\alpha = p/s$ with $s \leq 31$. For each α, the vertical segments indicate the extension of the s sub-bands. The dashed line indicates the flux $\alpha = 1/4$ realized in Ref. [39].

Nightingale and den Nijs showed that the Hall conductance of a two-dimensional insulator in which a set of bands is completely filled is given by $\sigma_{xy} = (e^2/h)\sum_n C_n$, which explains the quantization of the Hall conductance in the integer quantum Hall effect [40]. For the Hofstadter model with $\alpha = 1/s$, the lowest band has a Chern number of modulus one: we checked numerically, using a discretized version of the above integral, that $|C_1| = 1$ for $\alpha = 1/3$, $1/4$ and $1/5$ (the sign depends on the orientation conventions).

Anomalous velocity and transverse drift. A non-zero Berry curvature modifies the semi-classical dynamics of a wave packet in a band. In the presence of a force $\mathbf{F}$ in the lattice plane, the quasi-momentum evolves as $\hbar\dot{\mathbf{q}} = \mathbf{F}$, while the velocity acquires an anomalous contribution [31]

$$\dot{\mathbf{r}} = \frac{1}{\hbar}\boldsymbol{\nabla}_{\mathbf{q}} E_n(\mathbf{q}) - \dot{\mathbf{q}} \times \Omega_n(\mathbf{q})\, \mathbf{e}_z. \tag{3.35}$$

The anomalous velocity is perpendicular to the force, like a Hall drift. Consider now a band uniformly populated over the magnetic Brillouin zone, of area $(2\pi)^2/A_{\text{cell}}$, where A_{cell} is the area of the magnetic unit cell. The group velocity averages to zero, since $E_n(\mathbf{q})$ is periodic, while the average Berry curvature is $\langle\Omega_n\rangle = 2\pi C_n/[(2\pi)^2/A_{\text{cell}}] = C_n A_{\text{cell}}/2\pi$. The center of mass of the cloud thus drifts perpendicular to the force, with the velocity

$$|v_\perp| = \frac{|C_n|\, F A_{\text{cell}}}{h}, \tag{3.36}$$

a direct measurement of the Chern number in units fixed by the force and the lattice geometry.

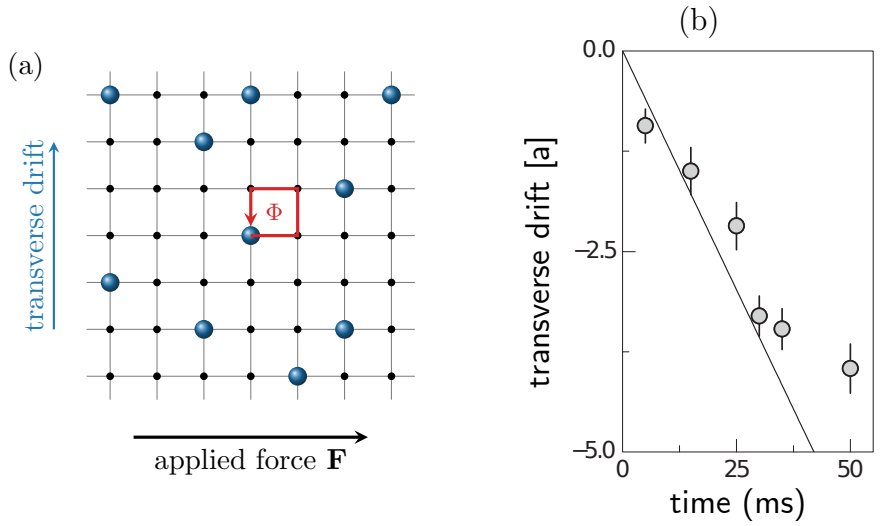


Figure 36: (a) Atoms in a square lattice with a uniform flux Φ per plaquette (Hofstadter model). A force applied along x induces a transverse drift of the atoms along y, proportional to the Chern number of the populated band. (b) Transverse displacement (in units of the lattice spacing) measured as a function of time, for a flux $\alpha = 1/4$. The linear drift gives the Chern number $C = 0.99(5)$. Data taken from Ref. [39].

Measuring the Chern number. This strategy was implemented in Ref. [39] with bosonic ^{87}Rb atoms in an optical lattice realizing the Hofstadter model with $\alpha = 1/4$ by laser-assisted tunneling. The atoms were loaded in the lowest band, populated nearly uniformly, and a constant force was applied along one lattice direction. The transverse displacement of the cloud was measured in situ as a function of time (see Fig. 36). It increases linearly with time, as expected for a Hall drift, and the comparison with the expression of $v_\perp$ above yields a Chern number $C = 0.99(5)$ for the lowest band, in agreement with the theoretical value. This experiment provided the first measurement of a Chern number with ultracold atoms.

4 Superfluid to Mott insulator transition

In the previous sections we described the motion of a single particle in an optical lattice. We now consider an assembly of interacting bosons in a deep lattice. Two energy scales then compete: the tunnel coupling J, which favours delocalization of the particles over the whole lattice and leads to a Bose-Einstein condensate, and the on-site interaction energy U, which penalizes the fluctuations of the occupation numbers of individual sites. When interactions dominate, and for an integer mean number of atoms per site, the gas becomes an incompressible Mott insulator, in which the atoms are localized on the lattice sites. The transition between the superfluid and the Mott insulator is a quantum phase transition, driven by quantum fluctuations rather than thermal fluctuations, which was predicted for lattice bosons in Ref. [41]. It was proposed to realize it with ultracold atoms in optical lattices in Ref. [6], and first observed in Ref. [7]. This system has since become a paradigm of quantum simulation [3].

In this section, we first derive the Bose-Hubbard Hamiltonian that models bosons

in a deep optical lattice, and we discuss the structure of its phase diagram. We then describe the transition quantitatively using the Gutzwiller variational approach, which provides a simple mean-field picture of both phases. We finally discuss the main experimental signatures of the transition: the loss of phase coherence revealed by interference experiments, the breakdown of superfluid transport, the shell structure of trapped Mott insulators observed by single-atom imaging, and the low-energy excitations close to the transition.

4.1 The Bose-Hubbard Hamiltonian

We consider spin-polarized bosonic atoms in a deep three-dimensional optical lattice, in the tight-binding regime discussed in section 2. We first show how contact interactions can be included in the tight-binding description, which leads to the Bose-Hubbard model, and we then compare the magnitudes of the tunnel coupling and of the interaction energy as a function of the lattice depth.

4.1.1 Tight-binding model with on-site interactions

We start from a cubic lattice potential

$$V(\mathbf{r}) = V_0 \left[\sin^2(k_\mathrm{L} x) + \sin^2(k_\mathrm{L} y) + \sin^2(k_\mathrm{L} z)\right], \tag{4.1}$$

of spacing $d = \pi/k_\mathrm{L}$, with sites located at the positions $\mathbf{r}_j$ of the simple cubic lattice. In the absence of interactions, and when only the lowest band is populated, the dynamics is described by the tight-binding Hamiltonian derived in section 2.3,

$$\hat{H}_0 = -J \sum_{\langle i,j \rangle} \hat{a}_i^\dagger \hat{a}_j, \tag{4.2}$$

where $\hat{a}_j$ annihilates a particle in the Wannier state $w(\mathbf{r} - \mathbf{r}_j)$ of the lowest band centered on the site j, and $J > 0$ is the nearest-neighbour tunnel coupling. The notation $\langle i, j \rangle$ denotes the ordered pairs of nearest-neighbouring sites, so that each bond appears twice in the sum and $\hat{H}_0$ is hermitian. In one dimension, (4.2) reduces to $\hat{H}_0 = -J \sum_j (\hat{a}_j^\dagger \hat{a}_{j+1} + \hat{a}_{j+1}^\dagger \hat{a}_j)$. Since the potential (4.1) is separable, the three-dimensional Wannier function factorizes as $w(\mathbf{r}) = w(x)w(y)w(z)$, where $w(x)$ is the one-dimensional Wannier function of the ground band, and the tunnel coupling J is the same as in one dimension.

We now include the interactions between atoms. At ultracold temperatures, they are described by the contact pseudo-potential $g\,\delta(\mathbf{r} - \mathbf{r}')$, with $g = 4\pi\hbar^2 a/m$ and a the s-wave scattering length. In second quantization, the interaction energy reads

$$\hat{H}_\mathrm{int} = \frac{g}{2} \int \hat{\psi}^\dagger(\mathbf{r}) \hat{\psi}^\dagger(\mathbf{r}) \hat{\psi}(\mathbf{r}) \hat{\psi}(\mathbf{r}) \, \mathrm{d}^3 r. \tag{4.3}$$

The Bloch basis, which diagonalizes the single-particle Hamiltonian, is not well suited to describe contact interactions: Bloch states being extended over the whole lattice, the interaction couples all quadruplets of Bloch states compatible with quasi-momentum conservation. The Wannier basis is much more convenient. Restricting the field operator to the lowest band, we write

$$\hat{\psi}(\mathbf{r}) = \sum_j w(\mathbf{r} - \mathbf{r}_j)\, \hat{a}_j, \tag{4.4}$$

which gives

$$\hat{H}_{\rm int} = \frac{g}{2} \sum_{i,j,k,l} \left[\int w^*(\mathbf{r}-\mathbf{r}_i) w^*(\mathbf{r}-\mathbf{r}_j) w(\mathbf{r}-\mathbf{r}_k) w(\mathbf{r}-\mathbf{r}_l)\, \mathrm{d}^3 r \right] \hat{a}_i^\dagger \hat{a}_j^\dagger \hat{a}_k \hat{a}_l. \tag{4.5}$$

In a deep lattice, the Wannier functions are localized within single wells, and the overlap integral is dominated by the on-site term $i = j = k = l$. The other terms, which describe nearest-neighbour interactions or interaction-assisted tunneling, involve the small overlap between Wannier functions of neighbouring sites and can be neglected in a first approximation. We are left with the on-site interaction

$$\hat{H}_{\rm int} \simeq \frac{U}{2} \sum_j \hat{a}_j^\dagger \hat{a}_j^\dagger \hat{a}_j \hat{a}_j = \frac{U}{2} \sum_j \hat{n}_j (\hat{n}_j - 1), \qquad \hat{n}_j = \hat{a}_j^\dagger \hat{a}_j, \tag{4.6}$$

where we used the bosonic commutation relation $[\hat{a}_j, \hat{a}_j^\dagger] = 1$, and where we defined the on-site interaction energy

$$U = g \int |w(\mathbf{r})|^4 \, \mathrm{d}^3 r = g \left[\int |w(x)|^4 \, \mathrm{d}x \right]^3. \tag{4.7}$$

The energy $U\hat{n}_j(\hat{n}_j - 1)/2$ is simply the interaction energy U multiplied by the number $n_j(n_j - 1)/2$ of pairs of atoms sitting on the site j.

Adding the two contributions, and working in the grand-canonical ensemble with a chemical potential μ, we obtain the Bose-Hubbard Hamiltonian [41, 6]

$$\hat{H} = -J \sum_{\langle i,j \rangle} \hat{a}_i^\dagger \hat{a}_j + \frac{U}{2} \sum_j \hat{n}_j (\hat{n}_j - 1) - \mu \sum_j \hat{n}_j. \tag{4.8}$$

It is the same model as the one studied in the notes *Advanced quantum mechanics*, where the tunnel coupling is denoted t. We will denote by z the coordination number, i.e. the number of nearest neighbours of a given site ($z = 2D$ for a hypercubic lattice in dimension D, i.e. $z = 6$ for the cubic lattice). The model (4.8) relies on several approximations, which are well fulfilled in deep optical lattices: (i) the single-band approximation requires the interaction energy, the chemical potential and the temperature to be small compared with the gap to the first excited band, of order $\hbar\omega_{\rm ho} = 2\sqrt{V_0 E_{\rm r}}$ (see (2.18)); (ii) tunneling beyond nearest neighbours is neglected; (iii) interactions between atoms in different sites are neglected.

4.1.2 Tunneling versus interaction

The two parameters J and U of the Bose-Hubbard model can be computed from the band structure and the Wannier functions of the lattice, and they depend very differently on the lattice depth V_0. As shown in section 2, the tunnel coupling decreases exponentially with the lattice depth, as

$$J \simeq \frac{4}{\sqrt{\pi}} E_{\rm r} \left(\frac{V_0}{E_{\rm r}} \right)^{3/4} \exp\left[-2 \left(\frac{V_0}{E_{\rm r}} \right)^{1/2} \right] \tag{4.9}$$

for $V_0 \gg E_{\rm r}$ (see (2.57)).

The interaction energy, on the contrary, increases with the lattice depth, since the Wannier functions become more and more localized. Its dependence can be estimated in the harmonic approximation of the lattice wells. Close to a minimum, the lattice potential (4.1) is approximately harmonic, $V(\mathbf{r}) \simeq V_0 k_{\mathrm{L}}^2 r^2 = m\omega_{\mathrm{ho}}^2 r^2/2$, and the Wannier function is close to the Gaussian ground state of the harmonic well,

$$w(x) \simeq \frac{1}{(\pi\sigma^2)^{1/4}}\,\mathrm{e}^{-x^2/(2\sigma^2)}, \qquad \sigma = \frac{1}{k_{\mathrm{L}}}\left(\frac{E_{\mathrm{r}}}{V_0}\right)^{1/4}, \tag{4.10}$$

where σ is the harmonic oscillator length given in (2.19). We then compute

$$\int |w(x)|^4\,\mathrm{d}x = \frac{1}{\pi\sigma^2}\int \mathrm{e}^{-2x^2/\sigma^2}\mathrm{d}x = \frac{1}{\sqrt{2\pi}\,\sigma}, \tag{4.11}$$

and, using $g = 4\pi\hbar^2 a/m = 8\pi a E_{\mathrm{r}}/k_{\mathrm{L}}^2$, we obtain

$$U \simeq \frac{g}{(2\pi)^{3/2}\sigma^3} = \sqrt{\frac{8}{\pi}}\,k_{\mathrm{L}} a\,E_{\mathrm{r}}\left(\frac{V_0}{E_{\mathrm{r}}}\right)^{3/4}. \tag{4.12}$$

In a cubic lattice, the interaction energy thus increases as $V_0^{3/4}$, as the inverse volume σ^3 of the Wannier function. The harmonic approximation overestimates U, since the actual wells are softer than their harmonic approximation and the Wannier function is broader than the harmonic ground state.

We show in Fig. 37 the values of J and U computed for ^{87}Rb atoms ($a \simeq 5.3\,\mathrm{nm}$) in a cubic lattice of wavelength $\lambda = 840\,\mathrm{nm}$, for which $k_{\mathrm{L}} a \simeq 0.040$ and $E_{\mathrm{r}} \simeq h \times 3.3\,\mathrm{kHz}$. The ratio U/J varies over more than three orders of magnitude when the depth is varied between 0 and $25\,E_{\mathrm{r}}$, which allows one to explore both the weakly interacting regime $U \ll J$ and the strongly interacting regime $U \gg J$ simply by tuning the lattice laser intensity. For example, at $V_0 = 13\,E_{\mathrm{r}}$ we find $J \simeq 0.0099\,E_{\mathrm{r}} \simeq h \times 32\,\mathrm{Hz}$ and $U \simeq 0.35\,E_{\mathrm{r}} \simeq h \times 1.1\,\mathrm{kHz}$, i.e. $U/J \simeq 35$. The interaction energy remains small compared with the band gap ($\hbar\omega_{\mathrm{ho}} \simeq 7\,E_{\mathrm{r}}$ at this depth), which justifies the single-band approximation. We will see that the superfluid-Mott insulator transition is expected around $U/J \simeq 30$ for the cubic lattice, i.e. for a lattice depth of about 12 to $13\,E_{\mathrm{r}}$.

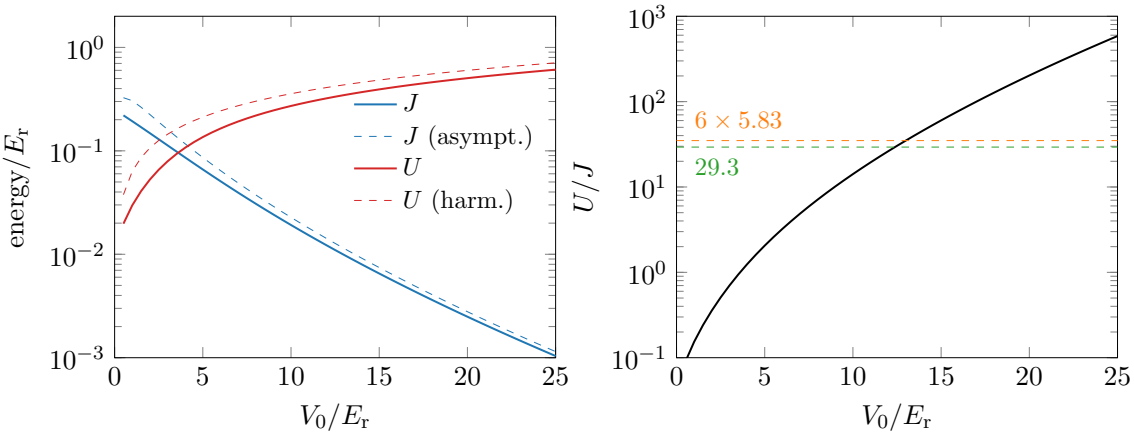


Figure 37: Left: tunnel coupling J (blue) and on-site interaction energy U (red) for ^{87}Rb atoms in a cubic lattice of wavelength $\lambda = 840\,\text{nm}$, as a function of the lattice depth V_0. The solid lines are computed from the exact band structure and Wannier function, the dashed lines show the deep-lattice asymptotic formula for J and the harmonic approximation (4.12) for U. Right: ratio U/J. The horizontal lines indicate the critical value $U/J = 6 \times 5.83$ predicted by the Gutzwiller mean-field theory for unit filling (section 4.3), and the exact value $U/J \simeq 29.3$ obtained from quantum Monte Carlo simulations [42]. They correspond to $V_0 \simeq 13.0\,E_r$ and $12.4\,E_r$, respectively.

4.2 Superfluid–Mott insulator phase diagram

Before developing a quantitative approach, we discuss the limiting cases of the Bose-Hubbard model, which allow us to anticipate the structure of its phase diagram in the plane $(J/U, \mu/U)$.

4.2.1 The atomic limit

For very deep lattices ($V_0 \gtrsim 30\,E_r$), the tunnel coupling becomes negligible on experimental time scales ($J \sim h \times 1\,\text{Hz}$ for ^{87}Rb at $30\,E_r$), and the lattice wells can be considered as independent. In this atomic limit $J = 0$, the Hamiltonian is a sum of single-site Hamiltonians

$$\hat{h}_j = \frac{U}{2}\hat{n}_j(\hat{n}_j - 1) - \mu\hat{n}_j, \tag{4.13}$$

which are diagonal in the Fock basis $|n\rangle$, $n \in \mathbb{N}$, with eigenvalues

$$E_n = \frac{U}{2}n(n-1) - \mu n. \tag{4.14}$$

The energy difference between two consecutive Fock states

$$E_{n+1} - E_n = Un - \mu \tag{4.15}$$

shows that the ground state is the Fock state $|n_0\rangle$, with $n_0 = 0$ for $\mu < 0$ and n_0 the integer such that

$$U(n_0 - 1) < \mu < Un_0 \tag{4.16}$$

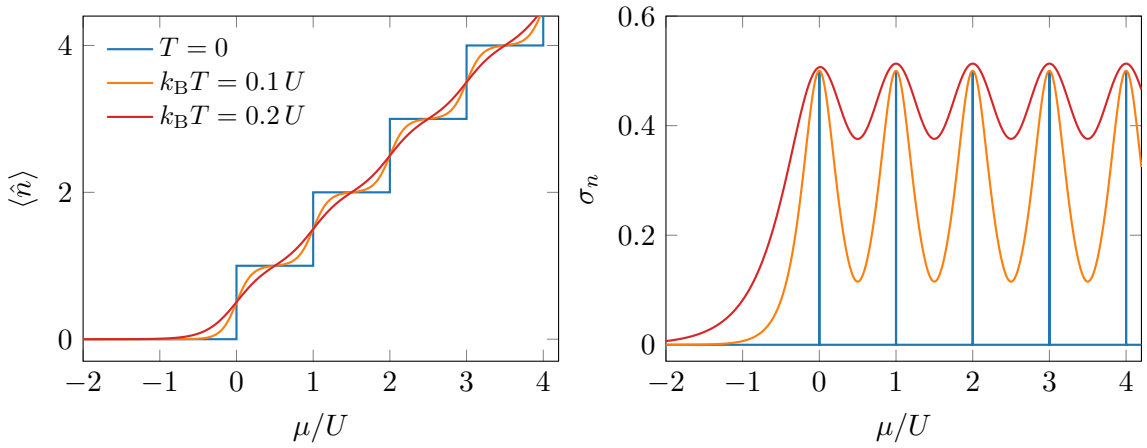


Figure 38: Mean occupation $\langle\hat{n}\rangle$ (left) and number fluctuations σ_n (right) of a lattice site in the atomic limit $J = 0$, as a function of the chemical potential, for temperatures $T = 0$, $k_\mathrm{B}T = 0.1\,U$ and $k_\mathrm{B}T = 0.2\,U$.

for $\mu > 0$. The mean occupation $\langle\hat{n}\rangle$ is thus a staircase function of the chemical potential, shown in Fig. 38. Within each plateau the system is incompressible, $\partial\langle\hat{n}\rangle/\partial\mu = 0$: adding a particle (particle excitation) costs the energy $Un_0 - \mu > 0$, and removing one (hole excitation) costs $\mu - U(n_0 - 1) > 0$. The number fluctuations vanish, except at the degeneracy points $\mu = Un_0$ where the states $|n_0\rangle$ and $|n_0 + 1\rangle$ are degenerate.

At finite temperature T, each site is described by a grand-canonical distribution $P(n) \propto \exp(-E_n/k_\mathrm{B}T)$. As shown in Fig. 38, the plateaus are rounded, and the number fluctuations $\sigma_n = (\langle\hat{n}^2\rangle - \langle\hat{n}\rangle^2)^{1/2}$ remain significant in the plateaus as soon as $k_\mathrm{B}T \gtrsim 0.1\,U$: the thermal admixture of the states $|n_0 \pm 1\rangle$, of relative weight $\sim \mathrm{e}^{-(U/2)/k_\mathrm{B}T}$ at the center of a plateau, then becomes significant. The temperature must therefore remain small compared with U to observe well-defined incompressible plateaus. We will use this simple model in section 4.6 to determine the temperature of trapped Mott insulators.

4.2.2 Qualitative phase diagram

The two limiting cases of the Bose-Hubbard model have very different properties.

- For $U \to 0$, the ground state is the Bose-Einstein condensate of all atoms in the Bloch state $\mathbf{q} = \mathbf{0}$ of the lowest band. For weak interactions $U \ll J$, it can be described by Bogoliubov theory, as done in the notes *Advanced quantum mechanics*: interactions lead to a quantum depletion of the condensate, which increases with U/J. One expects that strong enough interactions eventually lead to the disappearance of the condensate. The question is then whether superfluidity also disappears.

- For $J \to 0$, the ground state has a fixed integer occupation n_0 on each site and it is incompressible, as discussed above. The excitations are gapped, with a gap of order U. The question is whether this incompressible state survives a finite tunnel coupling J.

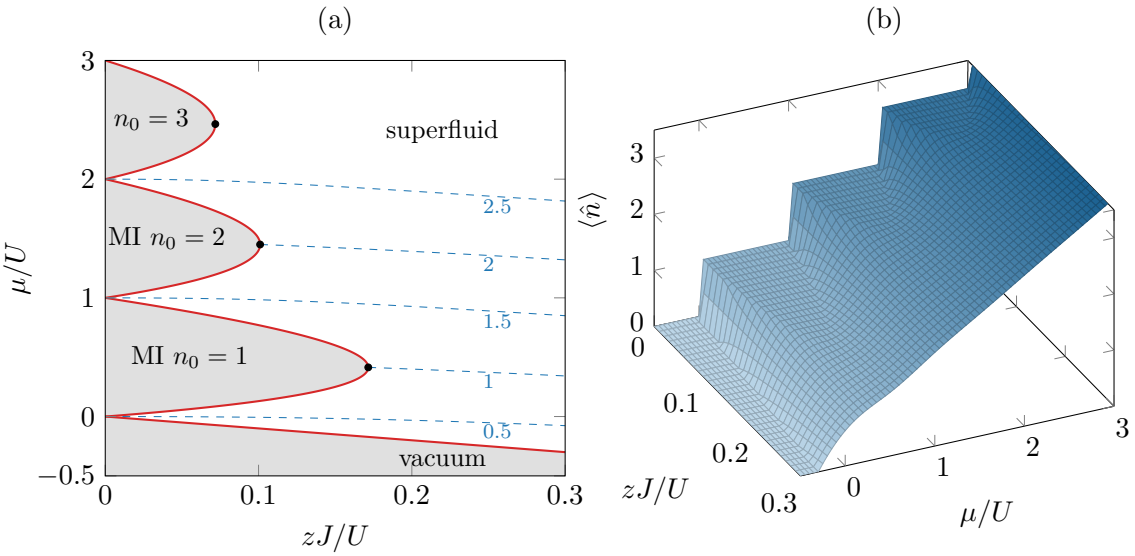


Figure 39: (a) Phase diagram of the Bose-Hubbard model calculated with the Gutzwiller mean-field approach. The red lines are the boundaries (4.42) of the Mott insulating (MI) lobes of integer fillings $n_0 = 1$, 2 and 3, and of the vacuum $n_0 = 0$ ($\mu < -zJ$). The black dots indicate the tips of the lobes. The blue dashed lines are lines of constant density $\langle \hat{n} \rangle = 0.5$, 1, 1.5, 2 and 2.5 in the superfluid phase. (b) Mean filling $\langle \hat{n} \rangle$ as a function of μ/U and zJ/U in the same approach, showing the incompressible plateaus of the Mott phases.

One expects that the gap protects the incompressibility for small enough J/U, so that each plateau of the atomic limit extends to a finite region of the phase diagram, called a Mott lobe. The resulting phase diagram is sketched in Fig. 39: the Mott insulating phases, of integer fillings $n_0 = 1, 2, 3, \ldots$, occupy lobes that shrink with n_0, while the rest of the phase diagram is occupied by the superfluid phase, which is compressible and supports a Bose-Einstein condensate. In the superfluid phase, the mean filling varies continuously with μ and J, while it is pinned to the integer value n_0 inside the Mott lobes, as shown by the three-dimensional representation of Fig. 39b (see also Ref. [43]).

Two kinds of transitions can be distinguished. Crossing the boundary of a lobe away from its tip, the density changes in the superfluid phase, and the transition is driven by the addition or removal of particles. At fixed integer density $\langle \hat{n} \rangle = n_0$, the transition occurs at the tip of the lobe, when the ratio J/U is varied at fixed density: this is the transition probed in most optical lattice experiments, where the atom number is fixed. For non-integer fillings, the system remains superfluid for all values of U/J.

4.3 Gutzwiller variational approach

The Bose-Hubbard model cannot be solved exactly in dimension $D \geq 2$, and its phase diagram has been determined accurately using quantum Monte Carlo simulations. We present here a simple variational approach, based on the Gutzwiller ansatz [44], which captures the main features of the superfluid-Mott insulator transition and gives analytical expressions of the phase boundaries.

4.3.1 Gutzwiller ansatz

We look for a trial ground state that interpolates between the two limiting cases discussed above.

- In the limit $U \to 0$, the ground state is a Bose-Einstein condensate in the Bloch state $\mathbf{q} = \mathbf{0}$. For a large number of particles, we can describe it as a coherent state of the condensate mode, of mean atom number N,

$$|\psi\rangle = \mathrm{e}^{-N/2} \exp\left(\sqrt{N}\, \hat{b}^\dagger_{\mathbf{q}=\mathbf{0}}\right) |\varnothing\rangle, \qquad \hat{b}^\dagger_{\mathbf{q}=\mathbf{0}} = \frac{1}{\sqrt{N_s}} \sum_j \hat{a}^\dagger_j, \tag{4.17}$$

  where N_s is the number of sites and $|\varnothing\rangle$ the vacuum. Since the operators $\hat{a}^\dagger_j$ commute, the exponential factorizes, and the coherent state is a product of single-site states,

$$|\psi\rangle = \prod_j \left[\mathrm{e}^{-\bar{n}/2} \exp\left(\sqrt{\bar{n}}\, \hat{a}^\dagger_j\right) |0\rangle_j\right], \qquad \bar{n} = \frac{N}{N_s}. \tag{4.18}$$

  Each site is in a coherent state, with a Poisson distribution of the atom number of mean $\bar{n}$.

- In the limit $J \to 0$, the Mott insulator of filling n_0 is also a product state,

$$|\psi\rangle = \prod_j |n_0\rangle_j. \tag{4.19}$$

In both limits, the ground state is a product of identical single-site states. In the general case, we thus use the Gutzwiller trial wave-function

$$|\psi\rangle = \prod_j |\phi\rangle_j, \qquad |\phi\rangle = \sum_{n=0}^{\infty} c(n)|n\rangle, \qquad \sum_n |c(n)|^2 = 1, \tag{4.20}$$

where the coefficients $c(n)$ are variational parameters, chosen to minimize the energy for a given chemical potential, or equivalently for a given mean filling $\bar{n} \equiv \langle\hat{n}\rangle = \sum_n n|c(n)|^2$. This ansatz neglects all correlations between different sites: it is a mean-field approximation, which becomes exact in the limit of infinite coordination number.

4.3.2 Gutzwiller energy functional

For a product state, the expectation value of the tunneling term factorizes, $\langle\hat{a}^\dagger_i \hat{a}_j\rangle = \langle\hat{a}^\dagger\rangle\langle\hat{a}\rangle$ for $i \neq j$. The mean value of the Hamiltonian (4.8) per site, i.e. the zero-temperature grand potential per site, then reads

$$F = -Jz|\langle\hat{a}\rangle|^2 + \frac{U}{2}\langle\hat{n}^2\rangle - \left(\mu + \frac{U}{2}\right)\langle\hat{n}\rangle, \tag{4.21}$$

where the factor z comes from the number of neighbours of each site, and where we wrote $\hat{n}(\hat{n}-1) = \hat{n}^2 - \hat{n}$. The mean values are computed in the single-site state $|\phi\rangle$,

$$\langle\hat{a}\rangle = \sum_n \sqrt{n+1}\, c^*(n)\, c(n+1), \tag{4.22}$$

$$\langle\hat{n}\rangle = \sum_n n\, |c(n)|^2, \qquad \langle\hat{n}^2\rangle = \sum_n n^2\, |c(n)|^2. \tag{4.23}$$

The ground state is obtained by minimizing F with respect to the coefficients $c(n)$ under the normalization constraint, which we enforce with a Lagrange multiplier λ. Using $\partial\langle\hat{a}\rangle/\partial c^*(n) = \sqrt{n+1}\, c(n+1) = (\hat{a}\, c)(n)$ and $\partial\langle\hat{a}\rangle^*/\partial c^*(n) = \sqrt{n}\, c(n-1) = (\hat{a}^\dagger c)(n)$, the condition $\partial F/\partial c^*(n) = \lambda\, c(n)$ reads

$$\left[\frac{U}{2}\hat{n}(\hat{n}-1) - \mu\hat{n} - zJ\left(\alpha^*\hat{a} + \alpha\,\hat{a}^\dagger\right)\right]|\phi\rangle = \lambda|\phi\rangle, \qquad \alpha = \langle\hat{a}\rangle. \tag{4.24}$$

The single-site state $|\phi\rangle$ is thus the ground state of a mean-field Hamiltonian, in which the neighbouring sites act on a given site via the order parameter α, which must be determined self-consistently. This is the same equation as the one obtained in the notes *Advanced quantum mechanics* by linearizing the fluctuations of the tunneling operator around their mean value. In practice, we solve (4.24) numerically by iteration, truncating the Fock basis to $n \leq 16$.

The order parameter α determines the condensed fraction. In a product state, the one-body correlation function reads $\langle\hat{a}_i^\dagger\hat{a}_j\rangle = |\alpha|^2 + (\bar{n} - |\alpha|^2)\delta_{ij}$, and the population of the Bloch state $\mathbf{q} = \mathbf{0}$ is

$$\langle\hat{b}_{\mathbf{0}}^\dagger\hat{b}_{\mathbf{0}}\rangle = \frac{1}{N_s}\sum_{i,j}\langle\hat{a}_i^\dagger\hat{a}_j\rangle = N_s|\alpha|^2 + \bar{n} - |\alpha|^2 \simeq N_s|\alpha|^2. \tag{4.25}$$

The condensed fraction is thus

$$f_{\rm c} = \frac{1}{N}\langle\hat{b}_{\mathbf{0}}^\dagger\hat{b}_{\mathbf{0}}\rangle = \frac{|\langle\hat{a}\rangle|^2}{\langle\hat{n}\rangle}. \tag{4.26}$$

It is non-zero in the superfluid phase and vanishes in the Mott phase, where each site is in a Fock state, $\langle\hat{a}\rangle = 0$. We note that, within the Gutzwiller approach, the condensed fraction and the superfluid fraction cannot be distinguished, since the order parameter α describes both the condensate and its ability to carry a superflow.

4.3.3 Gutzwiller ground state for unit filling

We show in Fig. 40 the Fock state distribution $|c(n)|^2$ of the Gutzwiller ground state for a unit filling $\langle\hat{n}\rangle = 1$, for increasing values of U/zJ. For $U \ll zJ$, the distribution is close to the Poisson distribution of a coherent state, as expected for a weakly interacting condensate. When U/zJ increases, interactions penalize multiple occupancies, and the distribution narrows around $n = 1$, the weights of the states $|0\rangle$ and $|2\rangle$ becoming equal and those of the states $n \geq 3$ negligible. Above a critical value $U/zJ \simeq 5.83$, the ground state is exactly the Fock state $|1\rangle$: the system is in the Mott insulating phase.

4.3.4 Number fluctuations

A simple way to characterize the transition is to compute the fluctuations of the atom number on a given site, $\Delta n = (\langle\hat{n}^2\rangle - \langle\hat{n}\rangle^2)^{1/2}$. They are shown in Fig. 41, normalized by the value $\sqrt{\bar{n}}$ expected for a Poisson distribution.

- For integer fillings $\bar{n} = 1$ and 2, the fluctuations decrease with U/zJ and vanish continuously at the critical values $U/zJ \simeq 5.83$ and 9.90 respectively, beyond which the system is a Mott insulator.

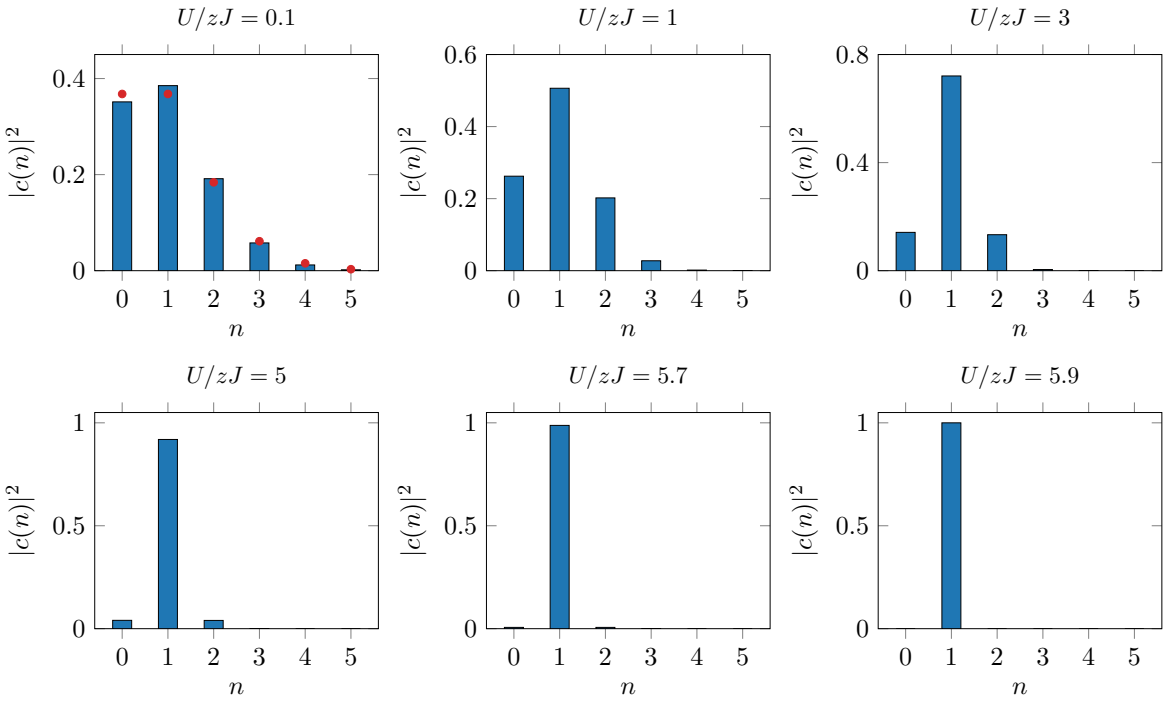


Figure 40: Distribution $|c(n)|^2$ of the atom number in the Gutzwiller ground state at unit filling $\langle \hat{n} \rangle = 1$, for $U/zJ = 0.1$, 1, 3, 5, 5.7 and 5.9. In the first panel, the red dots show the Poisson distribution of mean 1 of a coherent state.

- For non-integer fillings, the fluctuations remain finite for arbitrarily large interactions. In the limit $U \to \infty$, only the two Fock states $|\lfloor \bar{n} \rfloor\rangle$ and $|\lfloor \bar{n} \rfloor + 1\rangle$ are populated. For $\bar{n} < 1$, for instance, we have $|\phi\rangle = \sqrt{1-\bar{n}}|0\rangle + \sqrt{\bar{n}}|1\rangle$, which gives $\Delta n^2 = \bar{n}(1-\bar{n})$ and $|\langle \hat{a} \rangle|^2 = \bar{n}(1-\bar{n})$: the system remains superfluid, with a condensed fraction $1-\bar{n}$, as for hard-core bosons. Similarly, for $1 < \bar{n} < 2$, we find $\Delta n^2 = (\bar{n}-1)(2-\bar{n})$, i.e. $\Delta n/\sqrt{\bar{n}} \simeq 0.41$ for $\bar{n} = 1.5$, as observed in Fig. 41a.

- As a function of the filling (Fig. 41b), the fluctuations exhibit dips at integer fillings, which reach zero when zJ/U is below the critical value of the corresponding Mott lobe ($zJ/U < 0.172$ for $n_0 = 1$, $zJ/U < 0.101$ for $n_0 = 2$, $zJ/U < 0.072$ for $n_0 = 3$).

4.3.5 Particle-hole approximation close to a Mott state

Analytical expressions can be obtained close to a Mott state of filling n_0, by restricting the single-site state to the three Fock states $|n_0\rangle$ and $|n_0 \pm 1\rangle$, which describe the creation of a particle or a hole on top of the Mott state:

$$|\phi\rangle = c(n_0 - 1)|n_0 - 1\rangle + c(n_0)|n_0\rangle + c(n_0 + 1)|n_0 + 1\rangle. \tag{4.27}$$

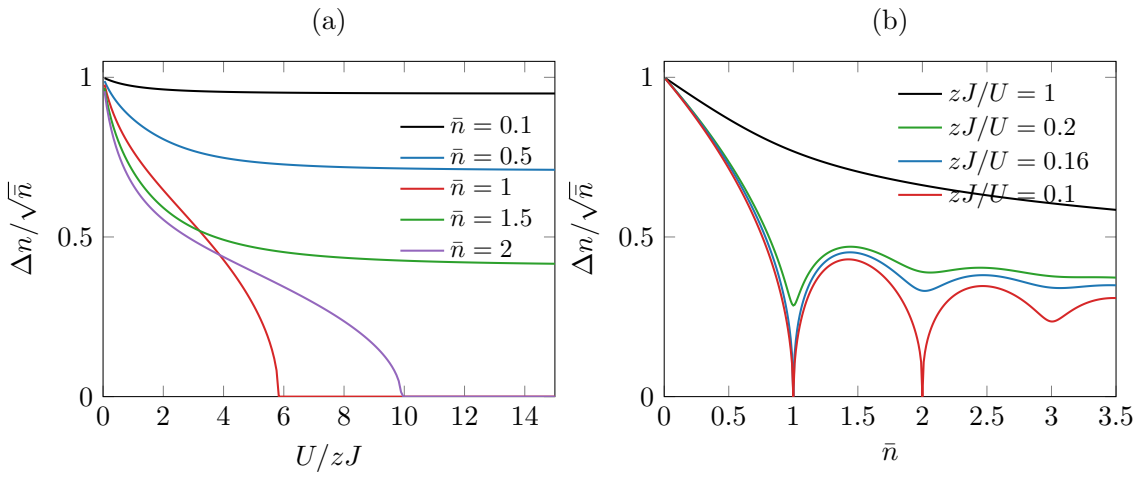


Figure 41: Number fluctuations Δn in the Gutzwiller ground state, normalized by their Poissonian value $\sqrt{\bar{n}}$. (a) As a function of U/zJ, for fixed fillings $\bar{n} = 0.1$, 0.5, 1, 1.5 and 2. (b) As a function of the filling $\bar{n}$, for $zJ/U = 1$, 0.2, 0.16 and 0.1.

We parametrize the normalized coefficients as

$$\begin{aligned} c(n_0 - 1) &= \cos\chi \, \sin\theta \, \mathrm{e}^{\mathrm{i}\phi_-}, \\ c(n_0) &= \cos\theta, \\ c(n_0 + 1) &= \sin\chi \, \sin\theta \, \mathrm{e}^{\mathrm{i}\phi_+}, \end{aligned} \tag{4.28}$$

where we chose $c(n_0)$ real and positive, the global phase of $|\phi\rangle$ being irrelevant. The angle θ measures the admixture of particle and hole excitations, and the angle χ their relative weight. The average filling reads

$$\langle\hat{n}\rangle = (n_0-1)\cos^2\chi\sin^2\theta + n_0\cos^2\theta + (n_0+1)\sin^2\chi\sin^2\theta = n_0 - \sin^2\theta\cos(2\chi). \tag{4.29}$$

Ground state at commensurate filling. We now assume a commensurate filling $\langle\hat{n}\rangle = n_0$, which imposes $\chi = \pi/4$ (unless $\theta = 0$), i.e. equal weights of particles and holes. The chemical potential term in (4.21) is then a constant $-\mu n_0$, which we drop. The interaction energy reads

$$\begin{aligned} \frac{U}{2}\langle\hat{n}(\hat{n}-1)\rangle &= \frac{U}{2}\left[n_0(n_0-1)\cos^2\theta + \frac{(n_0-1)(n_0-2) + (n_0+1)n_0}{2}\sin^2\theta\right] \\ &= \frac{U}{2}n_0(n_0-1) + \frac{U}{2}\sin^2\theta, \end{aligned} \tag{4.30}$$

which shows that a particle-hole pair costs an energy U. The order parameter (4.22) reads

$$\langle\hat{a}\rangle = \frac{\sin\theta\cos\theta}{\sqrt{2}}\left(\sqrt{n_0}\,\mathrm{e}^{-\mathrm{i}\phi_-} + \sqrt{n_0+1}\,\mathrm{e}^{\mathrm{i}\phi_+}\right), \tag{4.31}$$

hence

$$|\langle\hat{a}\rangle|^2 = \frac{\sin^2(2\theta)}{8}\left[2n_0 + 1 + 2\sqrt{n_0(n_0+1)}\cos(\phi_+ + \phi_-)\right]. \tag{4.32}$$

Dropping constant terms, the energy functional thus reads

$$F = \frac{U}{2}\sin^2\theta - \frac{zJ}{8}\sin^2(2\theta)\left[2n_0 + 1 + 2\sqrt{n_0(n_0+1)}\cos(\phi_+ + \phi_-)\right]. \tag{4.33}$$

The energy is obviously minimized for $\cos(\phi_+ + \phi_-) = 1$, i.e. $\phi_+ = -\phi_- \equiv \varphi$, the phase φ of the order parameter $\langle\hat{a}\rangle \propto \mathrm{e}^{\mathrm{i}\varphi}$ remaining arbitrary. This is the spontaneous breaking of the $U(1)$ symmetry associated with particle number conservation, characteristic of Bose-Einstein condensation. We then get

$$F = \frac{U}{2}\sin^2\theta - \frac{U_\mathrm{c}}{8}\sin^2(2\theta), \qquad U_\mathrm{c} = zJ\left(\sqrt{n_0} + \sqrt{n_0+1}\right)^2. \tag{4.34}$$

Writing $s = \sin^2\theta$ and $\sin^2(2\theta) = 4s(1-s)$, we have $F = Us/2 - U_\mathrm{c}s(1-s)/2$, which is minimized for $1 - 2s = U/U_\mathrm{c}$, provided this solution lies in the interval $0 \leq s \leq 1/2$. We obtain two regimes.

- For $U \leq U_\mathrm{c}$, the minimum is reached for

$$\cos(2\theta) = \frac{U}{U_\mathrm{c}}, \quad \text{i.e.} \quad \theta = \frac{1}{2}\arccos\left(\frac{U}{U_\mathrm{c}}\right). \tag{4.35}$$

  This state is superfluid, with a condensed fraction

$$f_\mathrm{c} = \frac{|\langle\hat{a}\rangle|^2}{n_0} = \frac{(\sqrt{n_0} + \sqrt{n_0+1})^2}{8n_0}\left[1 - \left(\frac{U}{U_\mathrm{c}}\right)^2\right]. \tag{4.36}$$

  The number fluctuations $\Delta n^2 = \sin^2\theta = (1 - U/U_\mathrm{c})/2$ also vanish linearly at U_c.

- For $U > U_\mathrm{c}$, the minimum is reached for $\theta = 0$, i.e. $c(n_0 - 1) = c(n_0 + 1) = 0$: the ground state is the Mott insulator $|n_0\rangle$, with no condensate and no number fluctuations.

The transition is continuous (second order): the order parameter vanishes as $|\langle\hat{a}\rangle| \propto (U_\mathrm{c} - U)^{1/2}$, with the mean-field critical exponent $1/2$. For unit filling, the critical point is

$$\left(\frac{U}{zJ}\right)_\mathrm{c} = \left(1 + \sqrt{2}\right)^2 = 3 + 2\sqrt{2} \simeq 5.83. \tag{4.37}$$

For the cubic lattice ($z = 6$), this corresponds to $U/J \simeq 35$.

We compare in Fig. 42 the condensed fraction (4.36) with the full numerical solution of the Gutzwiller problem at unit filling. The particle-hole approximation becomes exact close to the transition, where the admixture of the states $|n_0 \pm 1\rangle$ is small. It fails in the weakly interacting regime: for $U \to 0$, it predicts $f_\mathrm{c} = (1 + \sqrt{2})^2/8 \simeq 0.73$, instead of $f_\mathrm{c} = 1$ obtained when all Fock states are included.

4.3.6 Mott phase boundary

The boundary of the Mott lobes in the $(zJ/U, \mu/U)$ plane can be obtained by treating the mean-field Hamiltonian (4.24) in perturbation theory, since the order parameter α is small close to the boundary. We take α real without loss of generality. At zeroth order in α, the single-site ground state is the Fock state $|n_0\rangle$ of the atomic limit. The

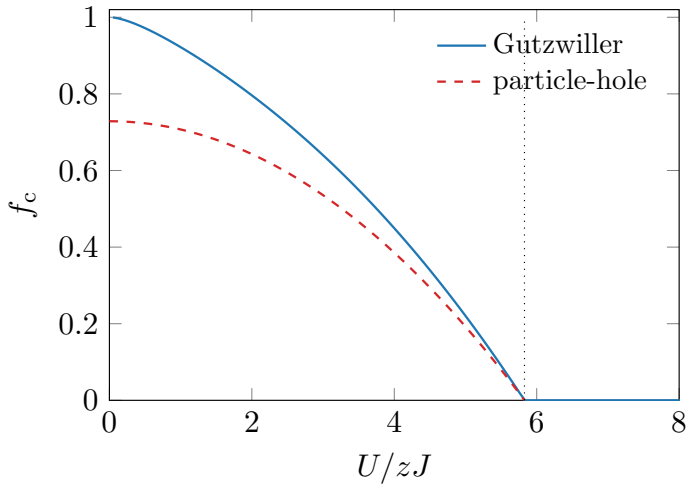


Figure 42: Condensed fraction f_c at unit filling as a function of U/zJ, computed with the full Gutzwiller ansatz (solid line) and in the particle-hole approximation (4.36) (dashed line). Both vanish at $(U/zJ)_c = 3 + 2\sqrt{2} \simeq 5.83$.

perturbation $\hat{T} = -zJ\alpha(\hat{a} + \hat{a}^\dagger)$ couples it to the states $|n_0 \pm 1\rangle$, with matrix elements $\langle n_0+1|\hat{T}|n_0\rangle = -zJ\alpha\sqrt{n_0+1}$ and $\langle n_0-1|\hat{T}|n_0\rangle = -zJ\alpha\sqrt{n_0}$, and energy denominators given by (4.15). At first order, we obtain

$$|\phi\rangle = |n_0\rangle + \frac{zJ\alpha\sqrt{n_0}}{\mu - U(n_0-1)}|n_0-1\rangle + \frac{zJ\alpha\sqrt{n_0+1}}{Un_0-\mu}|n_0+1\rangle. \tag{4.38}$$

Both denominators are positive inside the lobe of the atomic limit. The order parameter $\alpha = \langle\phi|\hat{a}|\phi\rangle$ must be determined self-consistently, which gives, at first order in α,

$$\alpha = zJ\alpha\left[\frac{n_0}{\mu - U(n_0-1)} + \frac{n_0+1}{Un_0-\mu}\right]. \tag{4.39}$$

The solution $\alpha = 0$ always exists and corresponds to the Mott phase. A superfluid solution $\alpha \neq 0$ appears when the bracket times zJ reaches one, i.e. on the line

$$\frac{1}{zJ} = \frac{n_0}{\mu - U(n_0-1)} + \frac{n_0+1}{Un_0-\mu}. \tag{4.40}$$

Inside the lobe, the right-hand side is smaller than $1/zJ$, and the Mott phase is stable; outside, the Mott state becomes unstable towards the formation of a condensate. Multiplying (4.40) by the two denominators, and writing $x = \mu/U$ and $\tau = zJ/U$, we obtain

$$(x - n_0 + 1)(n_0 - x) = \tau\left[n_0(n_0-x) + (n_0+1)(x-n_0+1)\right] = \tau(x+1), \tag{4.41}$$

i.e. the second-order equation $x^2 - (2n_0 - 1 - \tau)x + n_0(n_0-1) + \tau = 0$. Its two solutions give the lower and upper boundaries of the lobe,

$$\frac{\mu_\pm}{U} = n_0 - \frac{1}{2} - \frac{zJ}{2U} \pm \frac{1}{2}\sqrt{1 - 2(2n_0+1)\frac{zJ}{U} + \left(\frac{zJ}{U}\right)^2}. \tag{4.42}$$

For $J \to 0$, we recover the boundaries $\mu_- = U(n_0 - 1)$ and $\mu_+ = Un_0$ of the atomic limit. The lower boundary of the vacuum ($n_0 = 0$) is obtained in the same way: only the particle term contributes, and the condition $zJ = -\mu$ gives $\mu = -zJ$, which is the bottom of the band $-zJ$ of a single particle. The width of the lobe

$$\Delta = \mu_+ - \mu_- = \sqrt{U^2 - 2(2n_0+1)UzJ + (zJ)^2} \tag{4.43}$$

is the energy needed to create a particle-hole pair, i.e. the Mott gap. It vanishes at the tip of the lobe, located at

$$\left(\frac{zJ}{U}\right)_{\rm c} = 2n_0 + 1 - 2\sqrt{n_0(n_0+1)} = \left(\sqrt{n_0+1} - \sqrt{n_0}\right)^2, \qquad \frac{\mu_{\rm c}}{U} = n_0 - \frac{1}{2} - \frac{1}{2}\left(\frac{zJ}{U}\right)_{\rm c}. \tag{4.44}$$

The critical ratio $(U/zJ)_{\rm c} = (\sqrt{n_0} + \sqrt{n_0+1})^2$ coincides with the value $U_{\rm c}/zJ$ found in the particle-hole approximation at commensurate filling: the transition at fixed integer density occurs at the tip of the lobe. Numerically, we find $(U/zJ)_{\rm c} \simeq 5.83$, 9.90 and 13.93 for $n_0 = 1$, 2 and 3, the lobes shrinking as $(U/zJ)_{\rm c} \simeq 4n_0 + 2$ for large n_0.

The resulting phase diagram is shown in Fig. 39. The lines of constant non-integer density never enter a Mott lobe, while the line of density n_0 ends at the tip of the corresponding lobe. The Gutzwiller approach retains information on the lattice geometry only via the coordination number z, and it neglects quantum fluctuations beyond mean field, which favour the disordered phase. Its predictions can be compared with exact quantum Monte Carlo calculations: for the cubic lattice at unit filling, the critical point is $(U/J)_{\rm c} \simeq 29.3$ [42], compared with $6 \times 5.83 \simeq 35$ in mean field; for the square lattice, $(U/J)_{\rm c} \simeq 16.7$ [45], compared with $4 \times 5.83 \simeq 23$. As usual, the mean-field approximation becomes more accurate when the dimension (or the coordination number) increases, and it is qualitatively wrong in one dimension.

4.4 Interference experiments

The first evidence for the superfluid-Mott insulator transition was obtained by imaging the atomic gas after a time of flight [7]. We explain here how such images reveal the phase coherence between lattice sites, and how they evolve across the transition.

4.4.1 Phase coherence from time-of-flight experiments

At time $t = 0$, all trapping potentials are switched off, and the atoms expand freely. We neglect interactions during the expansion, which is justified since the density quickly drops. Restricting to the lowest band, the field operator at $t = 0$ is given by the expansion (4.4) in the Wannier basis. Each Wannier function then evolves according to the free propagator,

$$w(\mathbf{r} - \mathbf{r}_j) \to \left(\frac{m}{2\pi {\rm i}\hbar t}\right)^{3/2} \int {\rm e}^{{\rm i}m(\mathbf{r}-\mathbf{r}')^2/(2\hbar t)}\, w(\mathbf{r}' - \mathbf{r}_j)\, {\rm d}^3 r'. \tag{4.45}$$

At long times, we can neglect the term $mr'^2/(2\hbar t)$ in the phase (far-field regime), and the evolved Wannier function reads

$$w(\mathbf{r} - \mathbf{r}_j) \to \left(\frac{m}{{\rm i}\hbar t}\right)^{3/2} {\rm e}^{{\rm i}mr^2/(2\hbar t)}\, \tilde{w}(\mathbf{k})\, {\rm e}^{-{\rm i}\mathbf{k}\cdot\mathbf{r}_j}, \qquad \mathbf{k} = \frac{m\mathbf{r}}{\hbar t}, \tag{4.46}$$

where $\tilde{w}(\mathbf{k}) = (2\pi)^{-3/2} \int w(\mathbf{r}) \mathrm{e}^{-\mathrm{i}\mathbf{k}\cdot\mathbf{r}} \mathrm{d}^3 r$ is the Fourier transform of the Wannier function. The position $\mathbf{r}$ after time of flight thus maps the initial momentum $\hbar\mathbf{k} = m\mathbf{r}/t$. The density after time of flight, $n(\mathbf{r}) = \langle \hat{\psi}^\dagger(\mathbf{r}, t) \hat{\psi}(\mathbf{r}, t) \rangle$, reads

$$n(\mathbf{r}) = G(\mathbf{k})\, S(\mathbf{k}), \tag{4.47}$$

$$G(\mathbf{k}) = \left(\frac{m}{\hbar t}\right)^3 |\tilde{w}(\mathbf{k})|^2,$$

$$S(\mathbf{k}) = \sum_{i,j} \mathrm{e}^{\mathrm{i}\mathbf{k}\cdot(\mathbf{r}_i - \mathbf{r}_j)} \langle \hat{a}_i^\dagger \hat{a}_j \rangle, \tag{4.48}$$

where the phase factor $\mathrm{e}^{\mathrm{i}mr^2/(2\hbar t)}$ cancelled out. The envelope $G(\mathbf{k})$ is a smooth function of $\mathbf{k}$, of width $\sim 1/\sigma$ larger than the size $2k_\mathrm{L}$ of the Brillouin zone in a deep lattice. The structure factor $S(\mathbf{k})$ is the Fourier transform of the *site* correlation function

$$C(i, j) = \langle \hat{a}_i^\dagger \hat{a}_j \rangle, \tag{4.49}$$

which describes the phase coherence between the sites i and j. The time-of-flight image thus directly reveals the phase coherence properties of the lattice gas. We note that the far-field condition $t \gg mL^2/\hbar$, where L is the size of the cloud, is in practice not strictly fulfilled, which leads to a broadening of the interference peaks discussed below.

4.4.2 Phase coherence in the superfluid and Mott phases

The structure factor takes very different forms in the two phases.

- In the superfluid phase, for a fully condensed gas (all atoms in the Bloch state $\mathbf{q} = \mathbf{0}$), the phase coherence extends over the whole lattice,

$$C(i, j) = \langle \hat{n} \rangle, \qquad S(\mathbf{k}) = \langle \hat{n} \rangle \sum_{i,j} \mathrm{e}^{\mathrm{i}\mathbf{k}\cdot(\mathbf{r}_i - \mathbf{r}_j)} = \langle \hat{n} \rangle \left| \sum_j \mathrm{e}^{\mathrm{i}\mathbf{k}\cdot\mathbf{r}_j} \right|^2. \tag{4.50}$$

  The structure factor is that of a diffraction grating: it exhibits sharp peaks of height $\langle \hat{n} \rangle N_s^2$ at the vectors $\mathbf{K}$ of the reciprocal lattice, i.e. $\mathbf{K} = 2k_\mathrm{L}(n_x, n_y, n_z)$ with $n_x, n_y, n_z \in \mathbb{Z}$, of width $\sim 2\pi/L$. This is the matter-wave analog of the Bragg diffraction of X-rays by a crystal. Within the Gutzwiller approach, the condensed fraction is partial and $C(i, j) = |\alpha|^2 + (\bar{n} - |\alpha|^2)\delta_{ij}$: the peaks, of weight proportional to $|\alpha|^2$, are superimposed on a uniform background $N_s(\bar{n} - |\alpha|^2)$.

- In the Mott insulator of filling n_0, the state is a product of Fock states, and there is no phase coherence between different sites,

$$C(i, j) = n_0\, \delta_{ij}, \qquad S(\mathbf{k}) = N_s n_0 = N. \tag{4.51}$$

  The structure factor is uniform: there are no more diffraction peaks, and the time-of-flight image simply reproduces the envelope $G(\mathbf{k})$.

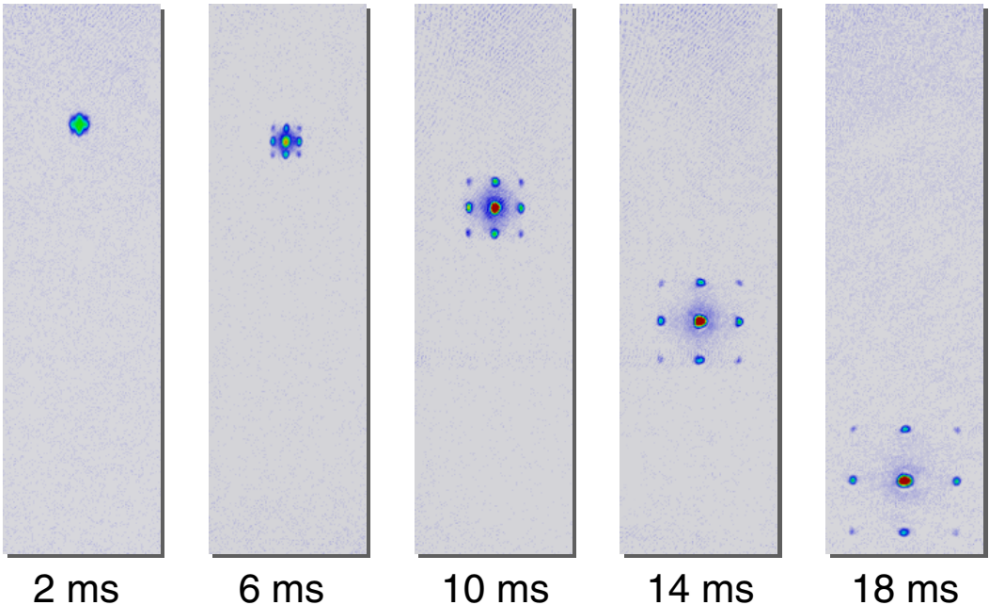


Figure 43: Absorption images of a ^{87}Rb Bose-Einstein condensate released from a three-dimensional optical lattice, for times of flight between 2 and 18 ms. Interference peaks emerge from the expanding cloud, which also falls under gravity. Figure taken from Ref. [43].

4.4.3 Observation of the transition

Expansion of a superfluid gas. We show in Fig. 43 a series of absorption images of a superfluid gas released from a three-dimensional optical lattice, taken for increasing times of flight [43]. At short times, the cloud has a single maximum, the different diffraction orders being still superimposed. After a few milliseconds, interference peaks appear and separate from each other, their distance increasing linearly with time, as expected from the momentum spacing $2\hbar k_{\mathrm{L}}$ between diffraction orders. The cloud also falls under gravity. After ~ 15 ms, the image represents the momentum distribution of the trapped gas, with the central peak $\mathbf{K} = \mathbf{0}$ and the first-order peaks $\mathbf{K} = \pm 2k_{\mathrm{L}}\mathbf{e}_{x,y}$ in the imaging plane, together with weaker second-order peaks along the diagonals.

Time-of-flight images across the transition. The pioneering experiment of Ref. [7] used a ^{87}Rb Bose-Einstein condensate adiabatically loaded into a three-dimensional optical lattice, whose depth was varied between 0 and $22\,E_{\mathrm{r}}$. The time-of-flight images are shown in Fig. 44. For shallow lattices, the interference peaks become more visible when the depth increases, since the atomic density gets more strongly modulated by the lattice, and the higher diffraction orders gain weight (the envelope $G(\mathbf{k})$ becomes broader). Around $V_0 \simeq 13\,E_{\mathrm{r}}$, an incoherent background appears and grows, and the interference peaks vanish beyond $V_0 \simeq 16\,E_{\mathrm{r}}$, the image reducing to a broad incoherent distribution. This loss of phase coherence signals the transition to the Mott insulator, in agreement with the expected critical lattice depth $V_0 \simeq 12$–$13\,E_{\mathrm{r}}$ (see Fig. 37). It was also shown that phase coherence is quickly restored when the lattice depth is lowered back into the superfluid regime, which demonstrates that the loss of coherence is not due to heating or to irreversible processes [7].

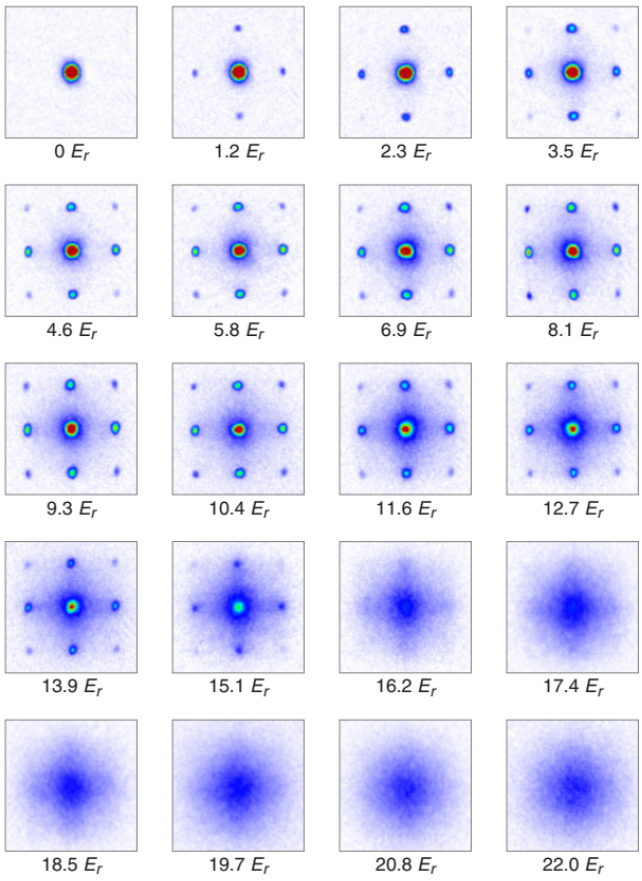


Figure 44: Time-of-flight absorption images of a ^{87}Rb gas released from a three-dimensional optical lattice, for lattice depths increasing from 0 to 22 E_r. The interference peaks, which reveal the phase coherence of the superfluid, disappear for $V_0 \gtrsim 16\,E_\mathrm{r}$, where the gas forms a Mott insulator. Figure taken from Ref. [7].

4.4.4 Particle-hole excitations and residual coherence

The interference peaks do not vanish abruptly at the transition. Indeed, the Mott insulator is a product of Fock states only for $J = 0$: for a finite tunnel coupling, it contains virtual particle-hole excitations, which restore a short-range phase coherence.

Perturbative calculation. Starting from the Mott insulator $|\psi_0\rangle = \prod_j |n_0\rangle_j$ of filling n_0, we treat the tunneling term of (4.8) at first order in perturbation theory. The operator $\hat{a}_i^\dagger \hat{a}_j$ acting on $|\psi_0\rangle$, with i and j nearest neighbours, creates the state $|\mathsf{p} : i, \mathsf{h} : j\rangle$ with a particle excitation ($n_0 + 1$ atoms) on site i and a hole excitation ($n_0 - 1$ atoms) on site j, with the matrix element $\sqrt{(n_0+1)n_0}$. Its interaction energy exceeds that of $|\psi_0\rangle$ by

$$\frac{U}{2}\left[(n_0+1)n_0 + (n_0-1)(n_0-2) - 2n_0(n_0-1)\right] = U. \tag{4.52}$$

At first order in J/U, the ground state thus reads

$$|\psi\rangle = |\psi_0\rangle + \frac{J\sqrt{n_0(n_0+1)}}{U} \sum_{\langle i,j\rangle} |\mathsf{p} : i, \mathsf{h} : j\rangle, \tag{4.53}$$

where the sum runs over all ordered pairs of nearest neighbours. The correlation function between two nearest neighbours i and j receives two contributions, from the terms $|\mathsf{p} : i, \mathsf{h} : j\rangle$ and $|\mathsf{p} : j, \mathsf{h} : i\rangle$, each equal to $Jn_0(n_0+1)/U$. We obtain the short-range correlation function

$$C(i,j) = n_0\,\delta_{ij} + \frac{2Jn_0(n_0+1)}{U}\,\delta_{\langle i,j\rangle}, \tag{4.54}$$

where $\delta_{\langle i,j\rangle} = 1$ if i and j are nearest neighbours, and 0 otherwise. The structure factor (4.48) per site then becomes modulated. In one dimension, each site having two neighbours at distances $\pm d$, we obtain

$$\frac{S(k)}{N_s} = n_0 + \frac{4Jn_0(n_0+1)}{U}\cos(kd), \tag{4.55}$$

and in a cubic lattice the cosine is replaced by $\cos(k_x d) + \cos(k_y d) + \cos(k_z d)$. The time-of-flight images of a Mott insulator thus still exhibit weak interference peaks at the reciprocal lattice vectors, whose contrast decreases as J/U.

Correlation length. At higher orders in perturbation theory, correlations between more distant sites appear: a correlation between two sites separated by ℓ lattice spacings requires a particle-hole pair separated by ℓ sites, which is created at order ℓ in the tunnel coupling. The correlation function thus decays exponentially,

$$C(i,j) \sim \left(\frac{J}{U}\right)^{|i-j|} = \exp\left(-\frac{|\mathbf{r}_i - \mathbf{r}_j|}{\xi}\right), \qquad \xi = \frac{d}{\ln(U/J)}, \tag{4.56}$$

where $|i-j|$ denotes the distance in units of d. The Mott insulator has a finite correlation length ξ, which is smaller than the lattice spacing deep in the Mott phase, and diverges at the transition. In the superfluid phase, on the contrary, $C(i,j)$ tends to the non-zero value $|\alpha|^2$ at large distance (long-range order).

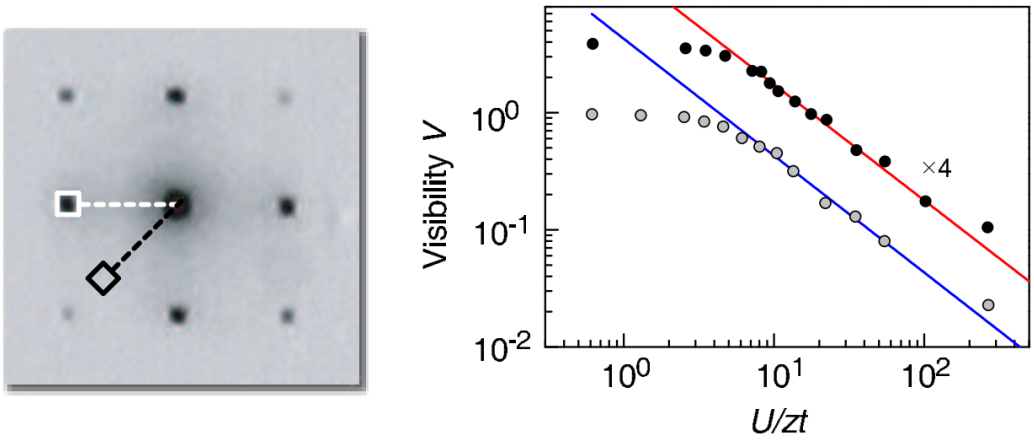


Figure 45: Left: time-of-flight image of a gas in a three-dimensional lattice, indicating the positions used to define the visibility (square: first-order interference peak; diamond: point at the same distance from the center along the diagonal). Right: visibility as a function of U/zJ (two data sets, one of them multiplied by 4 for clarity). The solid lines show the $(U/zJ)^{-1}$ scaling predicted by perturbation theory. Figure taken from Ref. [46].

Experimental signature. These residual correlations were measured in Ref. [46] by analysing the visibility of the interference pattern of a Mott insulator. To remove the contribution of the envelope $G(\mathbf{k})$, one compares the column density n_1 at the position of a first-order peak $\mathbf{k}_1 = 2k_{\mathrm{L}}\mathbf{e}_x$ (square in Fig. 45) with the density n_2 at a point $\mathbf{k}_2 = \sqrt{2}k_{\mathrm{L}}(\mathbf{e}_x + \mathbf{e}_y)$ at the same distance from the center along the diagonal (diamond), and defines the visibility

$$\mathcal{V} = \frac{n_1 - n_2}{n_1 + n_2}. \tag{4.57}$$

Using the structure factor computed above (the contribution of the z direction, integrated along the line of sight, being identical for both points), we obtain at first order in J/U

$$\mathcal{V} \simeq \frac{2J(n_0+1)}{U}\left[2 - 2\cos(\sqrt{2}\pi)\right] \simeq 5.1\,(n_0+1)\frac{J}{U}. \tag{4.58}$$

The visibility measured in Ref. [46] indeed decreases as $(U/zJ)^{-1}$ deep in the Mott regime, as shown in Fig. 45, which confirms that the residual coherence is due to particle-hole admixture. The visibility remains non-zero well beyond the transition point, so that the disappearance of interference peaks is not a sharp criterion to locate the transition.

4.4.5 Finite temperature

So far we discussed the ground state of the system. At finite temperature, phase coherence is also reduced by thermal fluctuations, and the superfluid phase only exists below a critical temperature T_{c}. A quantitative comparison between experiment and theory at finite temperature was performed in Ref. [47], using exact quantum Monte Carlo calculations of the Bose-Hubbard model, which include the harmonic trap and can simulate the same atom numbers as in the experiment. As shown in Fig. 46, the time-of-flight images measured in a superfluid state for increasing temperatures (between

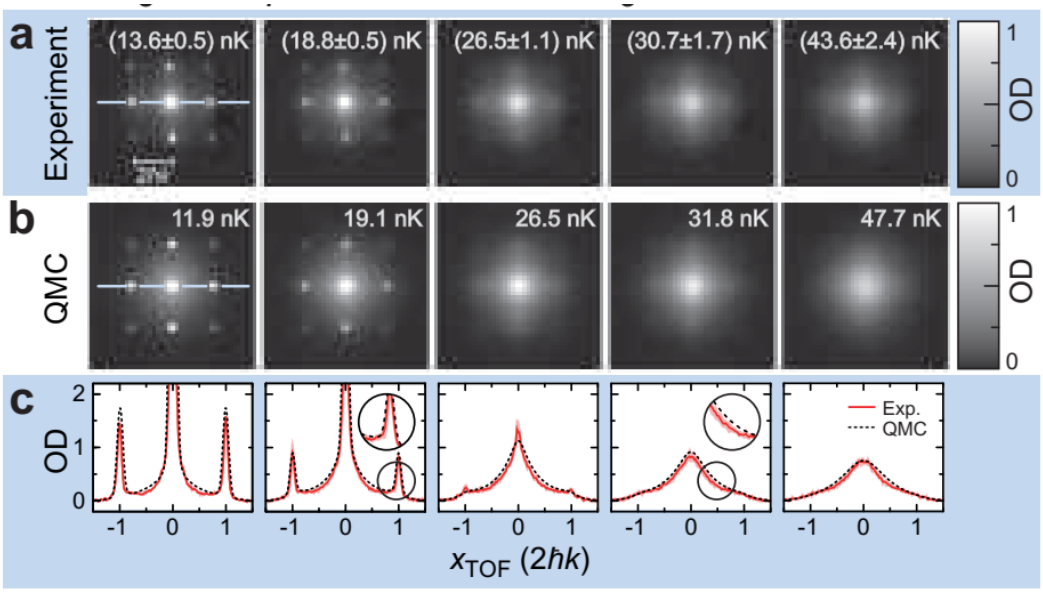


Figure 46: Time-of-flight images of a ^{87}Rb gas in a three-dimensional optical lattice at various temperatures, in the superfluid regime. (a) Experimental images. (b) Images obtained by quantum Monte Carlo simulations of the Bose-Hubbard model with the same parameters, the temperature being fitted. (c) Cuts along the lines indicated in the first images, comparing experiment (red) and simulation (dashed black). Figure taken from Ref. [47].

14 and 44 nK) are reproduced very accurately by the simulations, with the temperature as the only adjustable parameter. The interference peaks progressively vanish when the temperature increases, which signals the loss of long-range coherence above T_c. This agreement provides a reliable thermometry method, as well as a validation of the quantum simulation of the Bose-Hubbard model with cold atoms.

Superfluid critical temperature. By repeating these measurements for various values of U/J, the critical temperature for superfluidity was determined as a function of the interaction strength (Fig. 47). For weak interactions, $k_B T_c$ is of the order of 5 to 6 J, i.e. of the order of the band width, as for an ideal Bose gas in a lattice at unit filling. When U/J increases, the critical temperature is strongly suppressed, and it vanishes at the quantum critical point $(U/J)_c \simeq 29.3$, beyond which the ground state is a Mott insulator. The region above T_c is a normal fluid (NF), which smoothly connects to the Mott insulator at large U/J: at finite temperature, the Mott insulator is not a distinct thermodynamic phase, but a crossover regime of reduced compressibility.

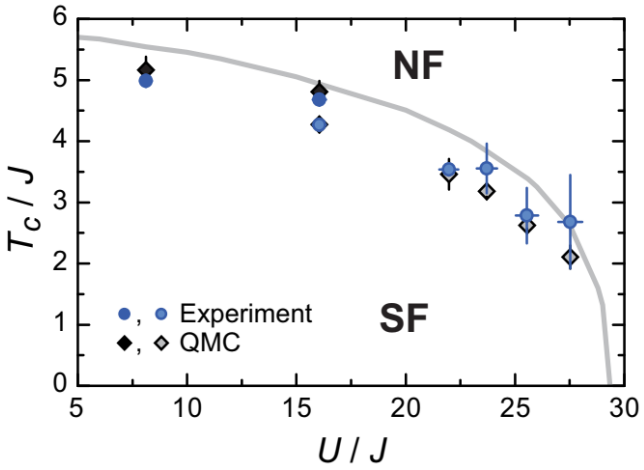


Figure 47: Critical temperature T_c for superfluidity (in units of J/k_B) as a function of U/J, for unit filling. The points are deduced from the experimental data and from the simulations including the trap; the grey line is the result of quantum Monte Carlo simulations for the uniform system, which separates the superfluid (SF) and normal fluid (NF) regions. Figure taken from Ref. [47].

4.5 Transport experiments: superfluid critical velocity

The superfluid character of the gas can also be probed via its transport properties. In Ref. [48], a ^{87}Rb Bose-Einstein condensate was loaded into a three-dimensional optical lattice, one of the lattice axes being set into motion at a constant velocity by detuning the frequencies of the two counter-propagating beams that create it. In the frame of the moving lattice, the condensate thus flows with a quasi-momentum p, which is increased up to the point where the flow becomes dissipative, as revealed by a sudden loss of coherence in time-of-flight images. The critical momentum p_c obtained in this way is shown in Fig. 48 as a function of the interaction parameter $u = U/J$, normalized by its value u_c at the Mott transition.

- For weak interactions, the critical momentum is close to $p_r/2$, where $p_r = \hbar k_L$ is the recoil momentum, i.e. half the quasi-momentum at the edge of the Brillouin zone. This value corresponds to the inflection point of the cosine dispersion relation $-2J\cos(pd/\hbar)$, beyond which the effective mass becomes negative and the flow is dynamically unstable, as observed in Ref. [19] and discussed in section 2.

- When the interactions increase, the critical momentum decreases and vanishes when approaching the Mott transition, $u \to u_c$. Close to the transition, the superfluid becomes extremely fragile, and even a slow flow destroys it. This behaviour is well reproduced by a mean-field theory of the moving superfluid [49] (red line). In the Mott phase, $u > u_c$, the measured critical momentum remains at a small residual value, consistent with the absence of superfluid flow.

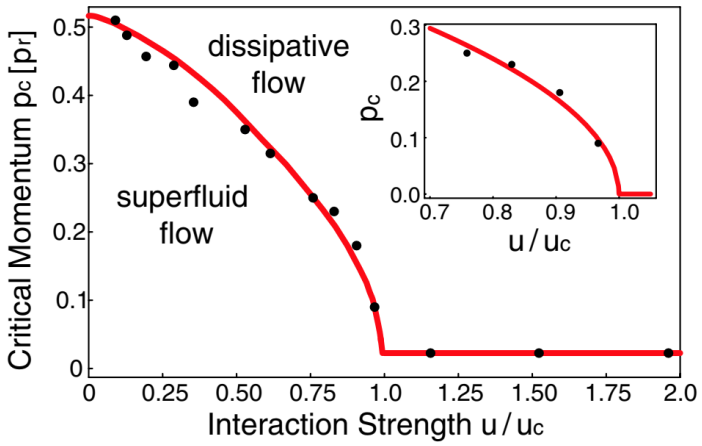


Figure 48: Critical momentum p_c (in units of the recoil momentum p_r) for the onset of dissipation of a condensate moving in a three-dimensional optical lattice, as a function of the interaction parameter $u = U/J$ normalized by its value u_c at the Mott transition. The red line is a mean-field prediction. Inset: zoom close to the transition. Figure taken from Ref. [48].

4.6 Mott shell structure

In experiments, the lattice gas is not homogeneous, because the Gaussian profile of the lattice beams creates an additional harmonic confinement. As a consequence, the local chemical potential varies across the cloud, and different phases coexist in different regions of space. We first describe this confinement, then the resulting shell structure, and its direct observation by single-atom imaging.

4.6.1 Harmonic confinement from Gaussian beams

We consider a one-dimensional lattice formed by two counter-propagating Gaussian beams of waist w, red-detuned from the atomic resonance so that the atoms are attracted towards the intensity maxima. The potential reads

$$V(\mathbf{r}) = -V_0 \cos^2(k_L x)\, \mathrm{e}^{-2(y^2+z^2)/w^2} = -V_0 \left[1 - \sin^2(k_L x)\right] \mathrm{e}^{-2(y^2+z^2)/w^2}. \tag{4.59}$$

Close to the axis, $\rho^2 = y^2 + z^2 \ll w^2$, we expand the Gaussian factor as $\mathrm{e}^{-2\rho^2/w^2} \simeq 1 - 2\rho^2/w^2$, and obtain

$$V(\mathbf{r}) \simeq -V_0 + V_0 \sin^2(k_L x) \left(1 - \frac{2\rho^2}{w^2}\right) + \frac{2V_0}{w^2}\rho^2. \tag{4.60}$$

Neglecting the slow variation of the lattice depth (second term), the potential is the sum of

- a lattice of uniform depth V_0,
- an additional harmonic confinement in the transverse plane, $m\Omega^2\rho^2/2$, of frequency

$$\Omega = \sqrt{\frac{4V_0}{mw^2}}. \tag{4.61}$$

In a cubic lattice formed by three such standing waves of equal depths and waists, each direction is confined by the two lattice beams orthogonal to it, giving an isotropic harmonic potential of frequency $\sqrt{8V_0/mw^2}$. For ^{87}Rb atoms in a lattice of depth $V_0 = 13\,E_\mathrm{r}$ at $\lambda = 840\,\mathrm{nm}$ and $w = 100\,\mu\mathrm{m}$, we get a frequency of about $2\pi \times 60\,\mathrm{Hz}$.

Assuming that the trap varies slowly at the scale of the lattice spacing, we can use the local density approximation: each region of the cloud behaves as a homogeneous system, with a local chemical potential

$$\mu(\mathbf{r}) = \mu_0 - \frac{1}{2} m\Omega^2 r^2, \tag{4.62}$$

where μ_0 is the chemical potential at the trap center, fixed by the total atom number.

4.6.2 Shell structure of a trapped Mott insulator

At fixed J/U, the local chemical potential (4.62) decreases from the center to the edge of the cloud. The local state of the gas is obtained by following a vertical line in the phase diagram, from μ_0 down to negative values (Fig. 49a). For zJ/U smaller than the critical value of the lobe $n_0 = 1$, this line crosses alternately Mott lobes and superfluid regions. The density profile then exhibits a succession of Mott plateaus of integer fillings, decreasing from the center to the edge, separated by thin superfluid shells, which are compressible and carry the number fluctuations (Fig. 49b). This structure, reminiscent of a wedding cake, was first observed with spatially resolved spectroscopic techniques [50, 51], before being directly imaged at the single-atom level.

The size of the shells can be estimated from the energy scales. For the parameters given above, the trap energy increases by $m\Omega^2 d^2/2 \simeq h \times 3\,\mathrm{Hz}$ between the trap center and the first neighbouring site, and the radius R_1 at which the trap energy reaches $U \simeq h \times 1.1\,\mathrm{kHz}$ is about 20 lattice sites.

4.6.3 Single-atom imaging

Quantum gas microscopes allow one to image the atoms in a two-dimensional optical lattice with single-site resolution [1, 52]. A high-resolution microscope objective, of numerical aperture NA $\simeq 0.7$ to 0.8, is placed close to the atoms, and collects the fluorescence emitted by the atoms (Fig. 50). The resolution, of the order of the optical wavelength, is comparable to the lattice spacing (532 nm in Ref. [52], 640 nm in Ref. [1]), and individual atoms can be located on the lattice sites after image processing.

Protocol. The imaging sequence involves the following steps.

- At the end of the experimental sequence, the lattice depth is suddenly increased to a very large value, of the order of 1 mK, which freezes the atom distribution: the tunneling time becomes much longer than the imaging time.
- The atoms are illuminated by near-resonant light during several hundred milliseconds, in a configuration that also provides laser cooling (optical molasses or Raman sideband cooling), maintaining the temperature in the range 1–20 μK. This temperature remains much smaller than the lattice depth, so that neither thermally activated hopping nor tunneling occurs during imaging, while each atom scatters enough photons to be detected.

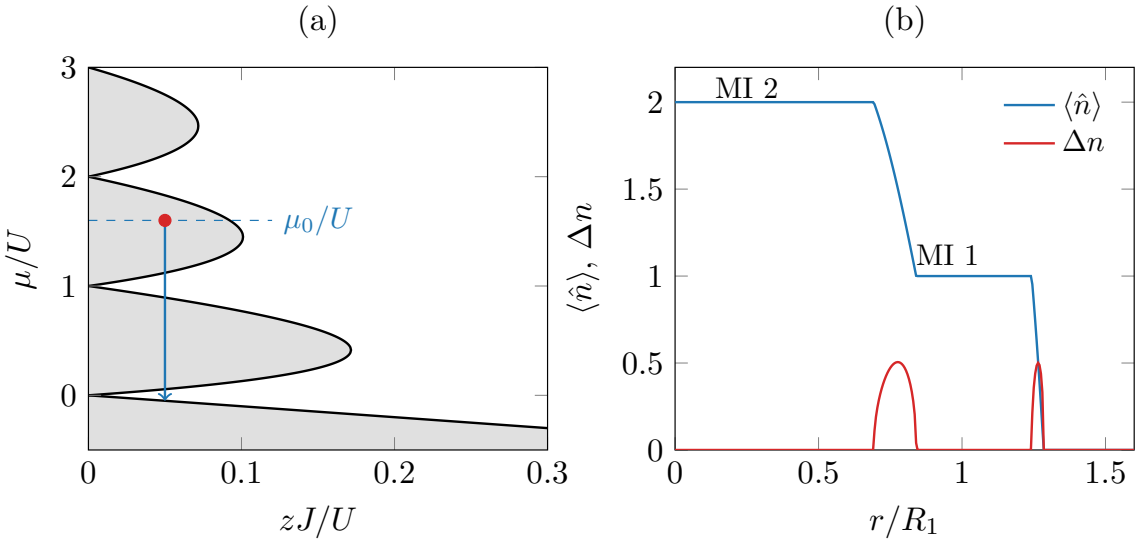


Figure 49: Shell structure of a trapped Bose gas in the local density approximation. (a) The local state follows the blue arrow in the phase diagram, from the central chemical potential $\mu_0 = 1.6\,U$ (red dot) down to the edge of the cloud, here for $zJ/U = 0.05$. (b) Mean filling $\langle\hat{n}\rangle$ and number fluctuations Δn calculated with the Gutzwiller approach, as a function of the distance r to the trap center, in units of $R_1 = (2U/m\Omega^2)^{1/2}$. Mott plateaus with $n_0 = 2$ and $n_0 = 1$ are separated by thin superfluid shells.

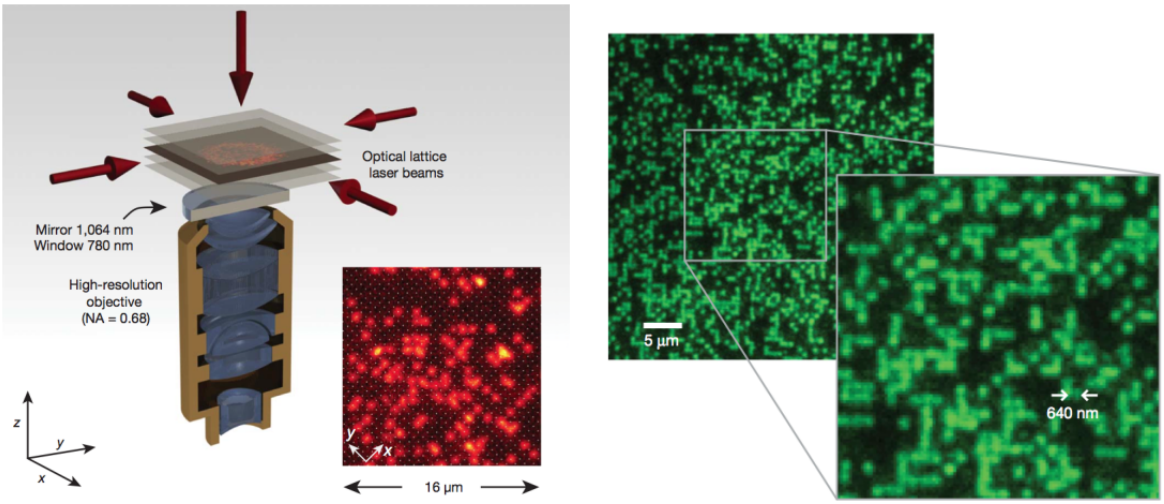


Figure 50: Single-atom imaging in optical lattices. Left: setup of Ref. [52], in which a two-dimensional gas in an optical lattice is imaged through a high-resolution objective; inset: fluorescence image of a dilute cloud, with the lattice sites indicated. Right: fluorescence image of a dilute cloud obtained in Ref. [1], the zoom showing individual atoms on a lattice of spacing 640 nm. Figures taken from Ref. [52] (left) and Ref. [1] (right).

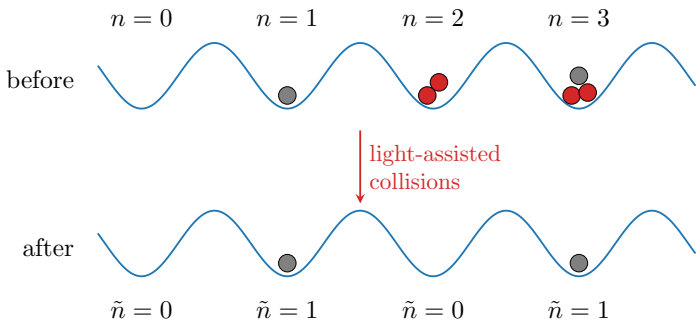


Figure 51: Parity projection during fluorescence imaging: light-assisted collisions eject pairs of atoms (red), so that the detected occupation is $\tilde{n} = n \bmod 2$.

- The fluorescence is collected by the microscope objective and imaged on a camera.
- Atoms sitting on the same site undergo light-assisted inelastic collisions during the illumination, which expel pairs of atoms from the trap within a short time. As a consequence, a site initially containing n atoms ends up with $n \bmod 2$ atoms (Fig. 51): the imaging only measures the parity of the site occupation.

4.6.4 In situ imaging of a Mott insulator

Observation of the transition. Fig. 52 shows in situ images of a two-dimensional ^{87}Rb gas in the central region of the trap, at unit filling, for increasing lattice depths [53]. In the superfluid regime ($V_0 = 6\,E_\mathrm{r}$), the atom number fluctuates strongly from site to site, and many sites appear empty because doubly occupied sites are detected as empty after parity projection. When the lattice depth increases, the fluctuations of the occupation are suppressed, and for $V_0 = 16\,E_\mathrm{r}$ almost all sites are singly occupied, as expected for a Mott insulator with $n_0 = 1$. The corresponding time-of-flight images show the loss of the interference peaks across the transition.

Wedding cake structure. Fig. 53 shows in situ images of entire clouds [52]. The superfluid cloud (a) exhibits strong fluctuations of the parity of the occupation. In the Mott regime, for increasing atom numbers (b to e), one observes first a homogeneous disk with one atom per site, then a structure with a dark core: the central region forms a Mott insulator with $n_0 = 2$, detected as empty after parity projection, surrounded by a ring with $n_0 = 1$. This is a direct observation of the wedding cake structure.

The radial profiles of the detected occupation $\bar{n}_\mathrm{det}$ and of its variance $\sigma^2_\mathrm{det} = \bar{n}_\mathrm{det}(1-\bar{n}_\mathrm{det})$ are shown in Fig. 54. The Mott regions correspond to plateaus with $\bar{n}_\mathrm{det} \simeq 1$ ($n_0 = 1$) or $\bar{n}_\mathrm{det} \simeq 0$ ($n_0 = 2$) and small fluctuations, separated by narrow regions with large fluctuations. The profiles are well fitted by the atomic-limit model at finite temperature introduced in section 4.2, combined with the local density approximation, which gives a temperature $T \simeq 0.09\,U/k_\mathrm{B}$. In contrast, in the superfluid regime (grey points), the detected occupation is close to 1/2 with maximal fluctuations $\sigma^2_\mathrm{det} \simeq 1/4$, as expected for a broad number distribution.

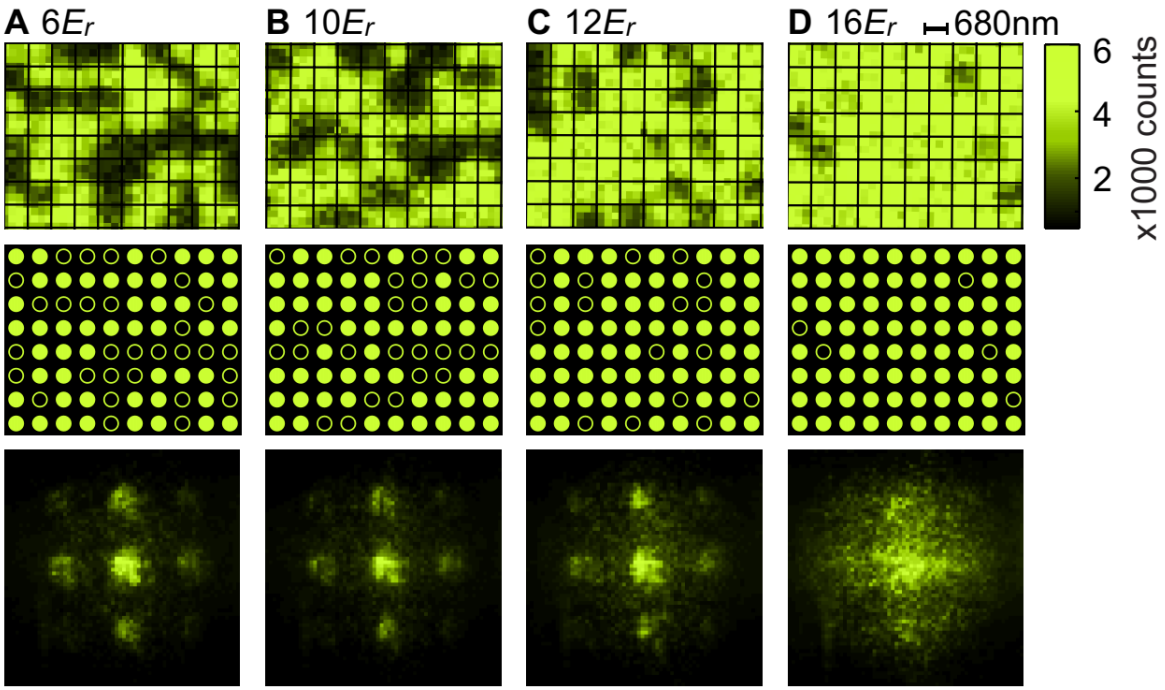


Figure 52: Single-site resolved imaging across the superfluid-Mott insulator transition in two dimensions, for lattice depths $V_0 = 6$, 10, 12 and 16 E_r. Top: fluorescence images of the central region of the cloud. Middle: reconstructed occupations (filled circles: occupied sites; open circles: sites detected as empty). Bottom: corresponding time-of-flight images. Figure taken from Ref. [53].

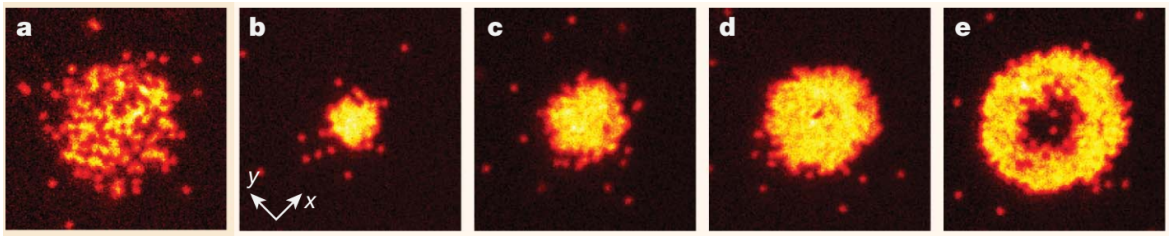


Figure 53: In situ fluorescence images of a two-dimensional ^{87}Rb gas in an optical lattice. (a) Superfluid. (b–e) Mott insulators for increasing atom numbers, exhibiting a shell structure; in (e), the central region with two atoms per site appears dark due to parity projection. Figure taken from Ref. [52].

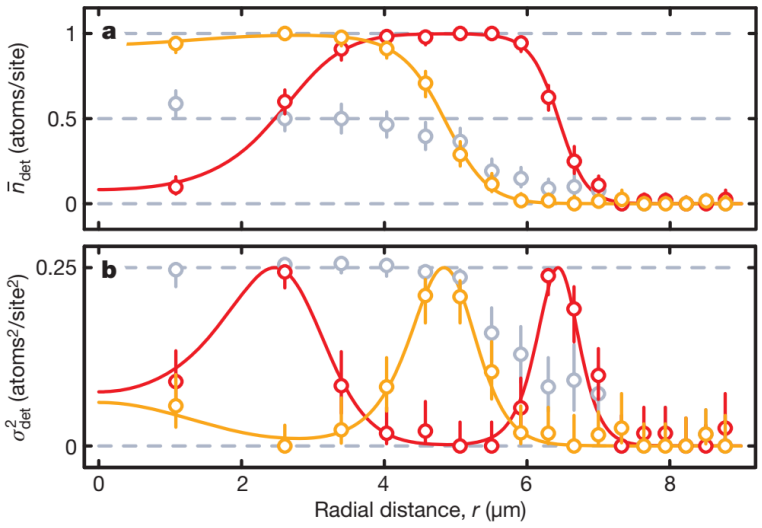


Figure 54: Radial profiles of the detected mean occupation $\bar{n}_{\rm det}$ (a) and of its variance $\sigma^2_{\rm det}$ (b), for a superfluid (grey), a Mott insulator with $n_0 = 1$ (orange) and a Mott insulator with a central $n_0 = 2$ region (red). The solid lines are fits with the atomic-limit model at finite temperature, which give $T \simeq 0.09\,U/k_{\rm B}$. Figure taken from Ref. [52].

4.7 Low-energy excitations

Single-atom imaging also gives access to the microscopic structure of the ground state and of its low-energy excitations. We discuss here two examples: the particle-hole pairs that dress the Mott insulator, and the amplitude (Higgs) mode of the superfluid close to the transition.

4.7.1 In situ observation of particle-hole pairs

As shown in section 4.4, a Mott insulator with finite J/U contains virtual particle-hole pairs on neighbouring sites, see (4.53). After parity projection, both a doubly occupied site and an empty site are detected as empty, so that a particle-hole pair appears as two neighbouring empty sites in a unit-filling Mott insulator. These correlated pairs were observed in Ref. [54], by measuring the correlations between the parities of neighbouring sites in one- and two-dimensional Mott insulators, as J/U is increased towards the superfluid (Fig. 55). The measured correlations agree with numerical calculations, and the pairs are found to be bound in the Mott phase.

In one dimension, the presence of bound particle-hole pairs gives rise to a non-local order parameter, the string order

$$\mathcal{O}_P = \lim_{\ell\to\infty} \left\langle \prod_{k=1}^{\ell} \mathrm{e}^{\mathrm{i}\pi(\hat{n}_k - n_0)} \right\rangle , \tag{4.63}$$

which measures the parity of the number of atoms in a segment of length ℓ. Since the particle-hole pairs are bound, they contribute to this parity only when they straddle the boundaries of the segment, and $\mathcal{O}_P$ remains non-zero in the Mott phase, while it vanishes in the superfluid phase. This string order, directly accessible from the parity images, was measured in one dimension in Ref. [54].

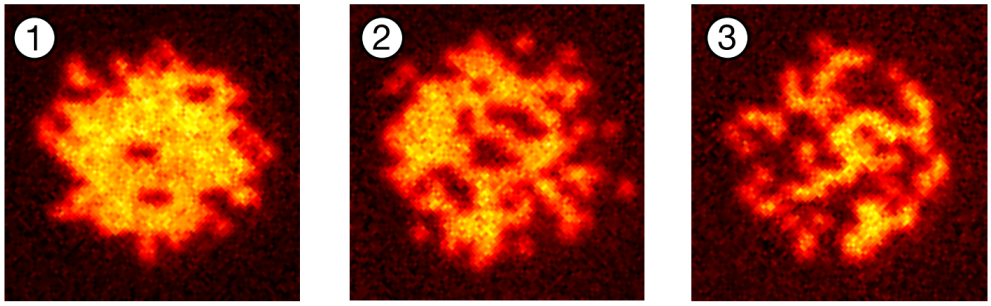


Figure 55: In situ parity images of a two-dimensional ^{87}Rb gas, from a Mott insulator (1) towards the superfluid regime (3), as J/U is increased. Particle-hole pairs appear as pairs of neighbouring empty sites in the unit-filling Mott region; their number increases with J/U. Figure taken from Ref. [54].

4.7.2 Higgs amplitude mode

Landau description. We come back to the Gutzwiller description in the particle-hole approximation at commensurate filling, using the parametrization (4.28) with $\chi = \pi/4$ and $\phi_+ = -\phi_- = \varphi$,

$$c(n_0 - 1) = \frac{\sin\theta\, \mathrm{e}^{-\mathrm{i}\varphi}}{\sqrt{2}}, \qquad c(n_0) = \cos\theta, \qquad c(n_0 + 1) = \frac{\sin\theta\, \mathrm{e}^{\mathrm{i}\varphi}}{\sqrt{2}}. \tag{4.64}$$

We introduce the complex order parameter

$$\psi = \rho\, \mathrm{e}^{\mathrm{i}\varphi}, \qquad \rho = \frac{1}{2}\sin(2\theta), \tag{4.65}$$

which is proportional to $\langle \hat{a} \rangle$ according to (4.31). Using $\sin^2(2\theta) = 4|\psi|^2$ and $\sin^2\theta = (1 - \sqrt{1 - 4|\psi|^2})/2$ (for $\theta \leq \pi/4$), the energy (4.34) reads

$$F[\psi] = \frac{U}{4}\left(1 - \sqrt{1 - 4|\psi|^2}\right) - \frac{U_\mathrm{c}}{2}|\psi|^2. \tag{4.66}$$

Expanding at fourth order in ψ, using $\sqrt{1-x} \simeq 1 - x/2 - x^2/8$, we obtain the Landau free energy

$$F[\psi] \simeq \frac{U - U_\mathrm{c}}{2}|\psi|^2 + \frac{U}{2}|\psi|^4. \tag{4.67}$$

For $U > U_\mathrm{c}$, the energy is minimum for $\psi = 0$: this is the Mott phase. For $U < U_\mathrm{c}$, the quadratic coefficient becomes negative and the energy is minimum on the circle $|\psi|^2 = (U_\mathrm{c} - U)/(2U)$: this is the superfluid phase, in which the phase φ of the order parameter is chosen spontaneously. The energy landscape then takes the form of a Mexican hat (Fig. 56).

Goldstone and Higgs modes. The low-energy collective modes of the superfluid correspond to oscillations of the order parameter around the minimum of the Mexican hat. Oscillations of the phase φ along the bottom of the hat cost no energy at long wavelength: they correspond to the gapless sound mode, i.e. the Goldstone mode

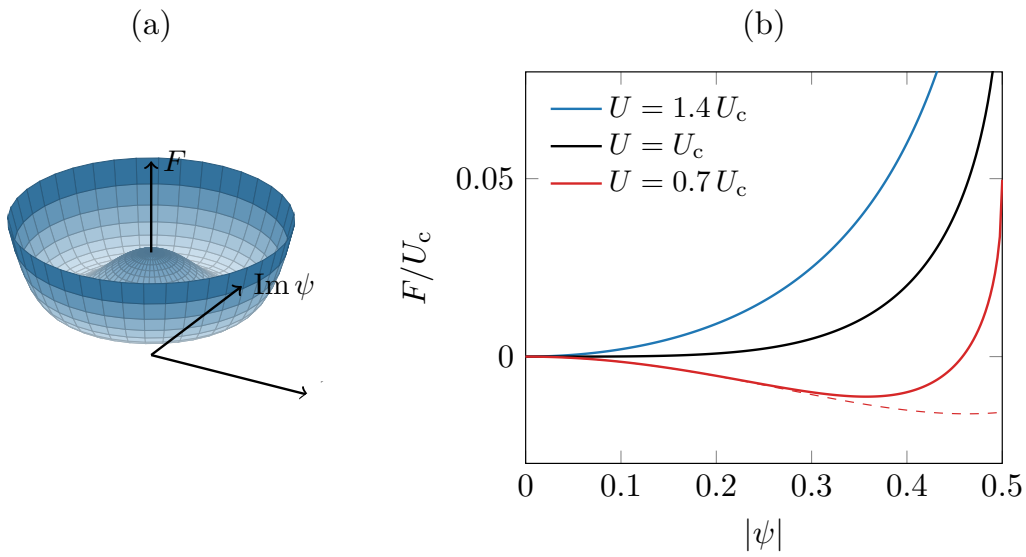


Figure 56: (a) Landau free energy (4.67) in the superfluid phase ($U = U_c/2$), as a function of the complex order parameter ψ: Mexican-hat potential. (b) Energy F in the particle-hole approximation as a function of $|\psi|$, for $U = 1.4\,U_c$ (Mott insulator), $U = U_c$ (critical point) and $U = 0.7\,U_c$ (superfluid); the dashed line is the fourth-order expansion (4.67) for $U = 0.7\,U_c$.

associated with the broken $U(1)$ symmetry. Oscillations of the modulus $|\psi|$, in the radial direction, have a finite frequency set by the curvature of the potential at its minimum: this is the amplitude mode, called Higgs mode by analogy with particle physics. As the transition is approached, the Mexican hat flattens and the frequency of the Higgs mode decreases to zero. The dynamics of the order parameter can be described by the time-dependent version of the Gutzwiller approach, $\mathrm{i}\hbar\,\mathrm{d}|\phi\rangle/\mathrm{d}t = \hat{h}_{\mathrm{MF}}|\phi\rangle$, where $\hat{h}_{\mathrm{MF}}$ is the mean-field Hamiltonian of (4.24) [55]. We linearized these equations numerically around the ground state at unit filling: the Higgs mode energy is well approximated, for $2 \lesssim U/zJ < U_c/zJ$, by $\hbar\omega_{\mathrm{H}} \simeq (U_c/2)\,[1 - (U/U_c)^2]^{1/2}$, which vanishes at the critical point as $(U_c - U)^{1/2}$. On the Mott side, the corresponding gapped excitation is the particle-hole pair, of energy $\Delta = \mu_+ - \mu_-$ given by (4.43), which also vanishes at the tip of the lobe. The Higgs mode is well defined only close to the tip of the Mott lobe, where the particle-hole symmetry of the low-energy theory makes amplitude and phase oscillations decoupled.

Experimental observation. The softening of the Higgs mode was observed in a two-dimensional gas in Ref. [56]. The lattice depth was weakly modulated at a frequency ν_{mod}, which modulates the ratio J/U and thus the amplitude of the order parameter, without changing its phase. The energy absorbed by the system was detected by measuring the temperature increase, using single-atom imaging (Fig. 57b). The absorption spectrum exhibits a threshold at a frequency ν_0, which corresponds to the gap of the amplitude mode. As shown in Fig. 57a, the gap $h\nu_0$ decreases when approaching the critical point j_c (with $j = J/U$, and $j_c \simeq 0.06$ in two dimensions) from the superfluid side, in agreement with theoretical predictions. On the Mott side, the threshold corresponds to

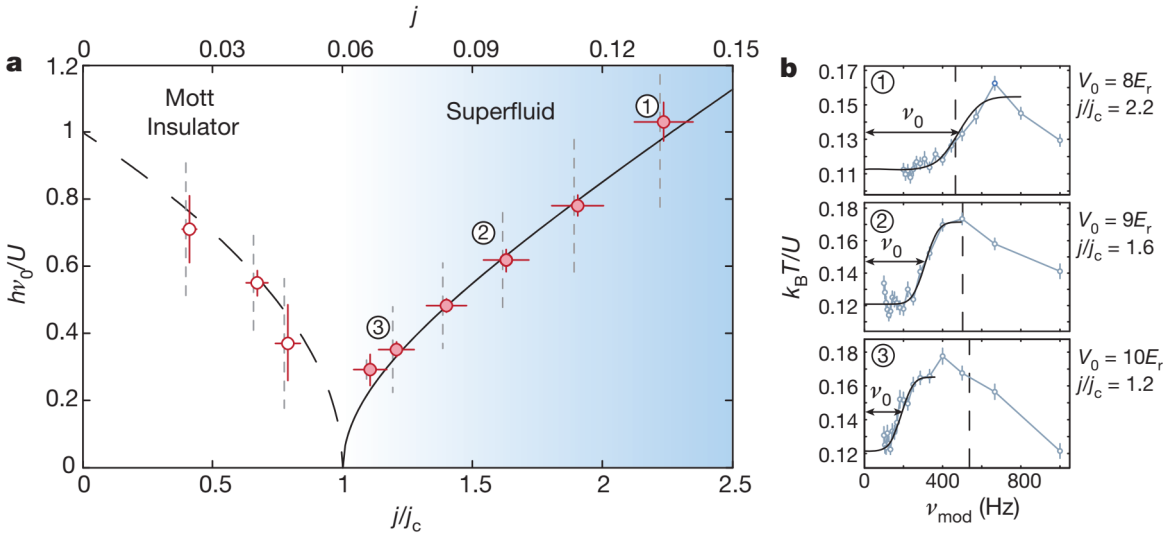


Figure 57: (a) Gap $h\nu_0$ of the low-energy excitations probed by lattice amplitude modulation, as a function of j/j_c with $j = J/U$, in the Mott insulator (open circles) and in the superfluid (filled circles). The lines are theoretical predictions, showing the softening of the gap at the critical point. (b) Temperature increase as a function of the modulation frequency for three lattice depths in the superfluid regime, from which the threshold frequency ν_0 is extracted. Figure taken from Ref. [56].

the particle-hole gap, which also softens at the transition.

5 Fermi-Hubbard model and quantum magnetism

In section 4 we studied bosons in optical lattices and the superfluid to Mott insulator transition of the Bose-Hubbard model. We now consider spin-1/2 fermions, described by the Fermi-Hubbard model. This model plays a central role in condensed matter physics, as the simplest model capturing the competition between the kinetic energy of electrons and their Coulomb repulsion in narrow energy bands [57]. Despite its apparent simplicity, its phase diagram in two dimensions remains largely unknown, and it is believed to contain key ingredients of high-temperature superconductivity in cuprate materials.

Compared to bosons, the spin degree of freedom brings in a new ingredient, magnetism. In the Mott insulating regime, the charge dynamics is frozen, but the spins remain coupled by a weak antiferromagnetic 'superexchange' interaction, which leads to magnetic ordering at low temperature. We first introduce the Fermi-Hubbard model and its main regimes. We then discuss the attractive case, related to the BEC-BCS crossover, the repulsive case and its Mott insulator, and finally quantum magnetism in fermionic Mott insulators, with emphasis on the experiments performed with quantum gas microscopes.

5.1 The Fermi-Hubbard model

We first write down the model, discuss its parameters and the simple limit of non-interacting particles, and give an overview of the different regimes that will be discussed in the rest of the section.

5.1.1 Hamiltonian

We consider fermionic atoms in two internal states, denoted $\sigma = \uparrow, \downarrow$, loaded in the lowest band of a deep optical lattice. As for bosons, the derivation of the tight-binding Hamiltonian from the Wannier functions of the lowest band (see sections 2 and 4) leads to the Fermi-Hubbard model

$$\hat{H} = -J \sum_{\langle j,j' \rangle, \sigma} \left(\hat{a}^\dagger_{j',\sigma} \hat{a}_{j,\sigma} + \hat{a}^\dagger_{j,\sigma} \hat{a}_{j',\sigma} \right) + U \sum_j \hat{n}_{j,\uparrow} \hat{n}_{j,\downarrow} - \mu \sum_{j,\sigma} \hat{n}_{j,\sigma}, \tag{5.1}$$

where $\langle j, j' \rangle$ denotes pairs of nearest-neighbour sites, $\hat{a}_{j,\sigma}$ annihilates a fermion of spin σ in the Wannier orbital of site j, $\hat{n}_{j,\sigma} = \hat{a}^\dagger_{j,\sigma} \hat{a}_{j,\sigma}$, J is the tunneling amplitude and μ the chemical potential. The two spin components have the same tunneling amplitude, as the lattice potential is in general spin independent.

Because of the Pauli principle, a given site can host at most one fermion per spin state, so that the occupation of a site is 0, 1 or 2. The on-site interaction U only concerns doubly-occupied sites, with one fermion in each spin state. It is given by the overlap of Wannier functions as for bosons, $U = g \int |w(\mathbf{r})|^4 \, \mathrm{d}^3 r$, where $g = 4\pi\hbar^2 a_{\uparrow\downarrow}/m$ involves the scattering length $a_{\uparrow\downarrow}$ between the two spin states. Its sign and magnitude can thus be adjusted using a Feshbach resonance, which makes it possible to explore both the repulsive ($U > 0$) and attractive ($U < 0$) Fermi-Hubbard models. We denote the mean filling (number of fermions per site) as

$$n = \langle \hat{n}_{j,\uparrow} + \hat{n}_{j,\downarrow} \rangle \in [0, 2]. \tag{5.2}$$

The particular point $n = 1$, i.e. one fermion per site on average, is called half filling, since the lowest band can host two fermions per site.

5.1.2 Non-interacting fermions: metal and band insulator

In the absence of interactions, the eigenstates are Slater determinants of Bloch states. In a cubic lattice of spacing d in dimension D, the dispersion relation of the lowest band reads

$$\varepsilon_{\mathbf{q}} = -2J \sum_{i=1}^{D} \cos(q_i d), \tag{5.3}$$

of total width $4DJ$. At zero temperature, the Bloch states are filled up to the Fermi energy μ, independently for each spin state. Two situations can occur (see Fig. 58):

- For a partially filled band ($0 < n < 2$), the Fermi level lies within the band. Low-energy excitations exist at the Fermi surface, and the system is a metal (or, in the language of cold atoms, a compressible Fermi liquid).
- For a filled band ($n = 2$, i.e. one fermion of each spin per site), all states of the band are occupied: the system is a band insulator, incompressible, with a gap given by the band gap to the second band. In a band insulator each site is doubly occupied, so that the density is uniform and does not fluctuate.

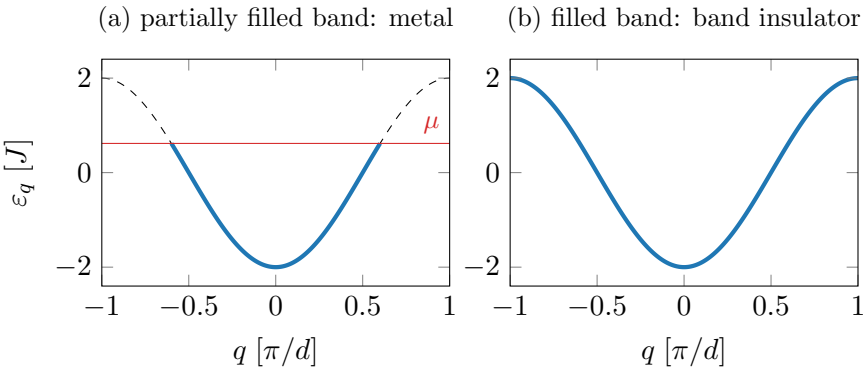


Figure 58: Lowest band of a one-dimensional lattice, $\varepsilon_q = -2J\cos(qd)$. The occupied states of each spin component at zero temperature are shown with thick lines. (a) Partially filled band: metal. (b) Filled band ($n = 2$): band insulator.

5.1.3 Overview of the interacting regimes

Interactions considerably enrich this simple picture. We will discuss the two cases separately:

- For attractive interactions ($U < 0$), fermions of opposite spins tend to pair. The attractive Hubbard model shares many features with the BEC-BCS crossover in the continuum, with a superfluid phase at low temperature.
- For repulsive interactions ($U > 0$), double occupancy is penalized. At half filling and for strong interactions $U \gg J$, the fermions localize with one atom per site, forming a Mott insulator, whose spins exhibit antiferromagnetic correlations at low temperature. Away from half filling, the nature of the ground state (metal, superfluid with d-wave pairing, stripe phases…) is still debated.

On bipartite lattices (such as the square or cubic lattices), the two cases are related by an exact mapping. The particle-hole transformation on a single spin component, $\hat{a}_{j,\downarrow} \to (-1)^j \hat{a}^\dagger_{j,\downarrow}$ (with $(-1)^j = \pm 1$ on the two sublattices), leaves the hopping term unchanged, but transforms $\hat{n}_{j,\downarrow}$ into $1 - \hat{n}_{j,\downarrow}$ and thus changes the sign of U. It maps the attractive model at filling n and zero magnetization onto the repulsive model at half filling with a magnetization $(n-1)/2$ per site. In particular, the attractive model at half filling is equivalent to the repulsive model at half filling, the superfluid and charge-density-wave orders of the former being mapped onto the in-plane and out-of-plane antiferromagnetic orders of the latter.

5.2 Attractive Fermi-Hubbard model and BEC-BCS crossover

In this section we show that the attractive Hubbard model reproduces, in the dilute limit, the physics of the BEC-BCS crossover, and we discuss the new features brought by the lattice.

5.2.1 Two-body bound state and mapping to the continuum

In the dilute limit $n \ll 1$, the fermions mostly occupy states near the bottom of the band, where the dispersion relation is quadratic, $\varepsilon_{\mathbf{q}} \simeq -2DJ + \hbar^2 q^2/2m^*$, with an effective mass $m^* = \hbar^2/(2Jd^2)$. The lattice structure then becomes irrelevant, and the attractive Hubbard model maps onto a continuum gas with a short-range attractive interaction, characterized by a scattering length that we now determine.

Bound state. We consider two fermions of opposite spins with zero total quasi-momentum in a cubic lattice ($D = 3$) of N_s sites, in the state

$$|\psi\rangle = \sum_{\mathbf{q}} c_{\mathbf{q}}\, \hat{a}^\dagger_{\mathbf{q},\uparrow}\hat{a}^\dagger_{-\mathbf{q},\downarrow}|0\rangle, \qquad \hat{a}_{\mathbf{q},\sigma} = \frac{1}{\sqrt{N_s}}\sum_j \mathrm{e}^{-\mathrm{i}\mathbf{q}\cdot\mathbf{r}_j}\hat{a}_{j,\sigma}. \tag{5.4}$$

The interaction term reads $U\sum_j \hat{n}_{j\uparrow}\hat{n}_{j\downarrow} = (U/N_s)\sum_{\mathbf{q},\mathbf{q}',\mathbf{k}} \hat{a}^\dagger_{\mathbf{q}+\mathbf{k},\uparrow}\hat{a}^\dagger_{\mathbf{q}'-\mathbf{k},\downarrow}\hat{a}_{\mathbf{q}',\downarrow}\hat{a}_{\mathbf{q},\uparrow}$, so that the Schrödinger equation $\hat{H}|\psi\rangle = E|\psi\rangle$ gives

$$(2\varepsilon_{\mathbf{q}} - E)\, c_{\mathbf{q}} + \frac{U}{N_s}\sum_{\mathbf{q}'} c_{\mathbf{q}'} = 0. \tag{5.5}$$

The solution is $c_{\mathbf{q}} = -UC/[N_s(2\varepsilon_{\mathbf{q}} - E)]$, with $C = \sum_{\mathbf{q}'} c_{\mathbf{q}'}$, and the self-consistency condition on C yields the bound-state equation. We write the energy of the bound state relative to the bottom of the two-particle continuum, $E = -4DJ - E_{\mathrm{m}}$, where $E_{\mathrm{m}} > 0$ is the binding energy, and we use $2\varepsilon_{\mathbf{q}} + 12J = 4J[3 - \cos(q_x d) - \cos(q_y d) - \cos(q_z d)]$. For $U = -|U| < 0$ we obtain

$$\frac{1}{|U|} = \frac{1}{N_s}\sum_{\mathbf{q}} \frac{1}{4J\,[3 - \cos(q_x d) - \cos(q_y d) - \cos(q_z d)] + E_{\mathrm{m}}}. \tag{5.6}$$

The right-hand side is a decreasing function of E_{m}, which takes its maximal value for $E_{\mathrm{m}} \to 0$. This value is finite in three dimensions (the sum is related to a Watson integral), and its numerical evaluation gives

$$\frac{1}{N_s}\sum_{\mathbf{q}} \frac{1}{4J\,[3 - \sum_i \cos(q_i d)]} \simeq \frac{0.1264}{J}. \tag{5.7}$$

A bound state thus exists only for an attraction exceeding a threshold,

$$|U| > |U_c| \simeq 7.91\, J. \tag{5.8}$$

This threshold is a consequence of the three-dimensional nature of the problem, as for a square well potential in the continuum. The binding energy, computed by solving (5.6) numerically, is shown in Fig. 59.

Scattering length and unitarity. The appearance of a bound state at threshold corresponds to a divergence of the scattering length, i.e. to the unitary limit of the BEC-BCS crossover. To see this, we consider the low-energy scattering amplitude of two particles in the lattice. Summing the Born series of the contact interaction (as for the renormalization of the pseudo-potential in the continuum), the zero-energy T-matrix

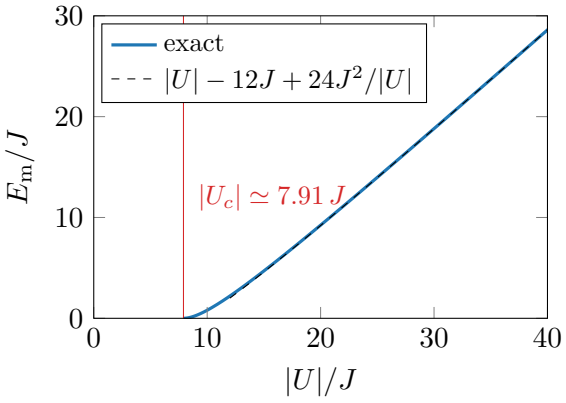


Figure 59: Binding energy E_m of two fermions of opposite spins with an attractive on-site interaction $U = -|U|$ in a cubic lattice, obtained by solving (5.6) numerically. A bound state appears for $|U| > |U_c| \simeq 7.91\,J$. The dashed line shows the strong-coupling expansion $E_\mathrm{m} \simeq |U| - 12J + 24J^2/|U|$.

reads $1/T = 1/U + (1/N_s)\sum_{\mathbf{q}} 1/(2\varepsilon_{\mathbf{q}} + 12J)$. Identifying T with the coupling constant $4\pi\hbar^2 a/m^*$ (times the volume per site d^3) of particles of mass m^*, i.e. $T = 8\pi J a/d$, we obtain

$$\frac{a}{d} = \frac{1}{8\pi J}\,\frac{1}{1/U + 1/|U_c|}. \tag{5.9}$$

For weak interactions $|U| \ll |U_c|$, this reduces to the Born approximation $a = Ud/(8\pi J)$. When the attraction increases, the scattering length becomes large and negative, and it diverges for $U = -|U_c|$, where the bound state appears. For stronger attraction, a is positive and the binding energy approaches the universal value $E_\mathrm{m} \simeq \hbar^2/(m^* a^2)$ in the regime $a \gg d$. In the dilute limit, varying U from 0 to $-\infty$ thus explores the whole BEC-BCS crossover, the threshold U_c playing the role of the unitary point.

5.2.2 New features brought by the lattice

Strong attraction: tightly bound pairs. For a strong attraction $|U| \gg J$, the two fermions of a pair sit on the same site, and the pair is much smaller than the lattice spacing. At variance with the continuum, where the mass of a deeply bound molecule is simply $2m$, the motion of such an on-site pair requires to break it virtually: one fermion first tunnels to a neighbouring site, at an energy cost $|U|$, and the second one follows. In second-order perturbation theory, the effective tunneling amplitude of the pair is thus

$$J_\mathrm{p} = \frac{2J^2}{|U|}, \tag{5.10}$$

where the factor 2 accounts for the two possible orders in which the fermions hop. The same virtual processes lower the energy of an isolated pair by $2zJ^2/|U|$, where z is the number of neighbours; for a pair at rest, adding the pair kinetic energy $-zJ_\mathrm{p}$, one recovers the expansion $E_\mathrm{m} \simeq |U| - 12J + 24J^2/|U|$ shown in Fig. 59. Moreover, two pairs on neighbouring sites block each other's virtual hopping because of the Pauli principle, which results in an effective nearest-neighbour repulsion $V = 4J^2/|U|$ between

pairs. The pairs thus behave as hard-core bosons with a small tunneling amplitude, and the critical temperature for superfluidity scales as

$$T_{\mathrm{c}} \sim \frac{J^2}{k_{\mathrm{B}}|U|}, \tag{5.11}$$

which decreases with the interaction strength. Since on the weak-coupling (BCS) side T_{c} is exponentially small, the critical temperature reaches its maximum for an intermediate interaction, of the order of the bandwidth. This is in contrast with the continuum, where T_{c} saturates to the BEC value on the BEC side of the crossover.

Half filling. At half filling ($\langle \hat{n}_{j,\uparrow} \rangle = \langle \hat{n}_{j,\downarrow} \rangle = 1/2$), the attractive model on a bipartite lattice has an additional particle-hole symmetry. For strong attraction, it appears in the effective model of pairs, in which the pair tunneling J_{p} and the repulsion $V = 2J_{\mathrm{p}}$ have exactly the ratio required for an SU(2) (pseudo-spin) symmetry. As a result, the superfluid order and a charge-density-wave order, in which pairs occupy every other site, are degenerate. This enhanced degeneracy suppresses the superfluid transition temperature at half filling, which vanishes in two dimensions.

5.2.3 Phase diagram and experiments

The phase diagram of the two-dimensional attractive Hubbard model is sketched schematically in Fig. 60 for an intermediate interaction strength. At high temperature, pairs form below a temperature scale set by the binding energy, without long-range coherence (pseudogap regime). A superfluid phase, of the Berezinskii-Kosterlitz-Thouless type in two dimensions, appears at lower temperatures, with a critical temperature reaching about $0.15\,J$, except at half filling where it is suppressed by the degeneracy with the charge-density wave. The limits $n = 0$ and $n = 2$ correspond respectively to the vacuum and to the band insulator.

This physics was explored with a quantum gas microscope in Ref. [58], using a two-dimensional gas of ^{6}Li atoms with attractive interactions. Site-resolved images allowed the measurement of pair and charge-density-wave correlations, which were compared to quantum Monte Carlo simulations. The temperatures reached so far are not low enough to observe superfluidity in the lattice.

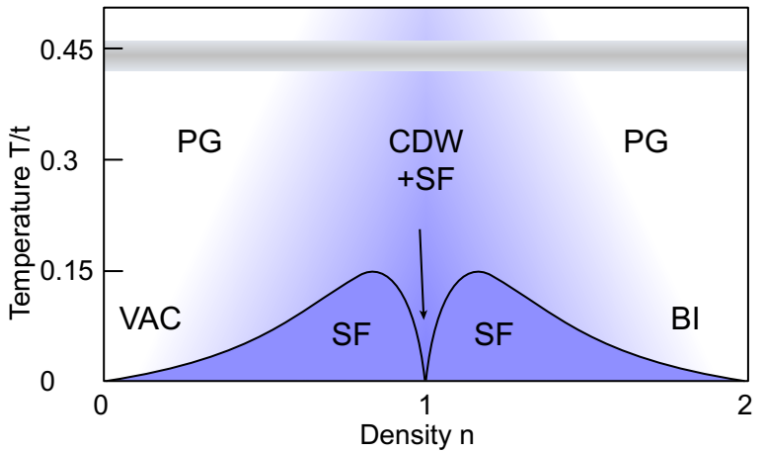


Figure 60: Schematic phase diagram of the two-dimensional attractive Fermi-Hubbard model as a function of the density n and temperature T (in units of the tunneling, denoted t in the figure). SF: superfluid; CDW: charge-density wave; PG: pseudogap (preformed pairs); VAC: vacuum; BI: band insulator. The grey band indicates the temperature range explored in the experiment. Figure taken from Ref. [58].

5.3 Repulsive Fermi-Hubbard model and Mott insulator

We now consider repulsive interactions $U > 0$. We first describe the Mott insulator in the simple limit of vanishing tunneling, then its observation with ultracold atoms, and finally its generalization to atoms with an SU(N) symmetry.

5.3.1 Atomic limit and Mott gap

At half filling and for strong repulsion $U \gg J$, a state with one fermion per site minimizes the interaction energy, each doubly-occupied site costing an energy U. The motion of a fermion necessarily creates a doubly-occupied site and an empty site, which costs an energy U: the system is an insulator, called a Mott insulator, with a charge gap of order U (reduced by the kinetic energy of the doublon and hole excitations, of order the bandwidth). Contrary to the band insulator, it is not due to the band structure, but to interactions.

Atomic limit. The incompressibility of the Mott insulator can be understood in the atomic limit $J = 0$, in which the sites are independent. The grand-canonical partition function of a single site, whose four states $|0\rangle$, $|\uparrow\rangle$, $|\downarrow\rangle$ and $|\uparrow\downarrow\rangle$ have the energies 0, $-\mu$, $-\mu$ and $U - 2\mu$, reads

$$\mathcal{Z} = 1 + 2\mathrm{e}^{\beta\mu} + \mathrm{e}^{\beta(2\mu-U)}, \qquad \beta = \frac{1}{k_\mathrm{B}T}, \tag{5.12}$$

from which we deduce the filling and the probability of double occupancy

$$n = \frac{2\mathrm{e}^{\beta\mu} + 2\mathrm{e}^{\beta(2\mu-U)}}{\mathcal{Z}}, \qquad P_\mathrm{d} = \frac{\mathrm{e}^{\beta(2\mu-U)}}{\mathcal{Z}}. \tag{5.13}$$

At low temperature $k_\mathrm{B}T \ll U$, the filling exhibits a plateau $n = 1$ for $0 < \mu < U$, as shown in Fig. 61: the system is incompressible, $\partial n/\partial\mu \simeq 0$. At half filling ($\mu = U/2$),

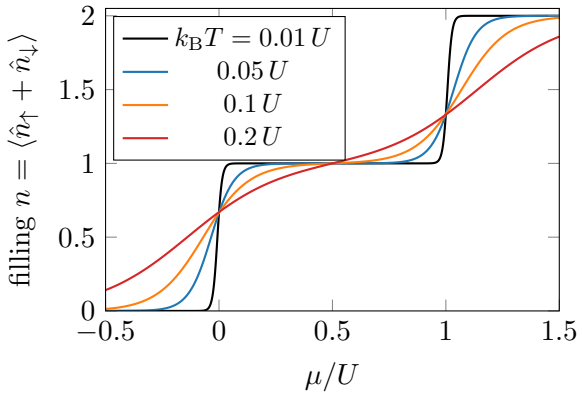


Figure 61: Filling n as a function of the chemical potential in the atomic limit $J = 0$, computed from (5.13) for different temperatures. The plateau at $n = 1$ for $0 < \mu < U$ is the Mott insulator, the plateau at $n = 2$ the band insulator.

the double occupancy is thermally activated, $P_\mathrm{d} = 1/(2 + 2\mathrm{e}^{\beta U/2}) \simeq \frac{1}{2}\mathrm{e}^{-U/2k_\mathrm{B}T}$. The Mott plateau is thus well defined for temperatures $k_\mathrm{B}T \lesssim U/10$. In this regime the spin of each site is free: the Mott insulator carries an entropy $k_\mathrm{B} \ln 2$ per site, and its spins are disordered. We will see that spin correlations only appear at a much lower temperature scale.

Mott insulator in a trap. In a harmonic trap, the local density approximation assigns a local chemical potential $\mu(\mathbf{r}) = \mu_0 - V_\mathrm{trap}(\mathbf{r})$ to each region of the cloud. Depending on the central chemical potential, the cloud may thus exhibit a metallic region, a Mott plateau at $n = 1$, and even a band-insulating core at $n = 2$. The first evidence for fermionic Mott insulators was obtained in three-dimensional lattices from the suppression of double occupancy and of the compressibility [59, 60].

Site-resolved imaging of a fermionic Mott insulator. Quantum gas microscopes give a direct view of the Mott insulator, as shown in Fig. 62 [61]. In this experiment, a two-dimensional gas of ^{6}Li atoms in two hyperfine states was loaded in a square lattice, and imaged with single-site resolution for different values of U/J. The imaging is sensitive only to the parity of the occupation: doubly occupied sites are lost by light-assisted collisions and appear empty. For weak interactions ($U/8J = 1.1$, where $8J$ is the bandwidth of the square lattice), the occupation fluctuates strongly from site to site, as expected for a metal. For intermediate interactions, a band insulator with $n \simeq 2$ forms in the center of the trap and appears as an empty region, surrounded by a Mott-insulating ring. For strong interactions ($U/8J = 15.3$), a large Mott plateau with almost one atom per site and strongly suppressed fluctuations is observed.

5.3.2 Mott insulators with SU(N) symmetry

Alkaline-earth atoms (such as Sr) and atoms with a similar electronic structure (such as Yb) have a ground state $^1S_0$ with zero electronic angular momentum, $J = 0$ (here J denotes the electronic angular momentum, not the tunneling). For fermionic isotopes, the nuclear spin $I \neq 0$ provides $N = 2I + 1$ internal states (for instance $N = 6$ for

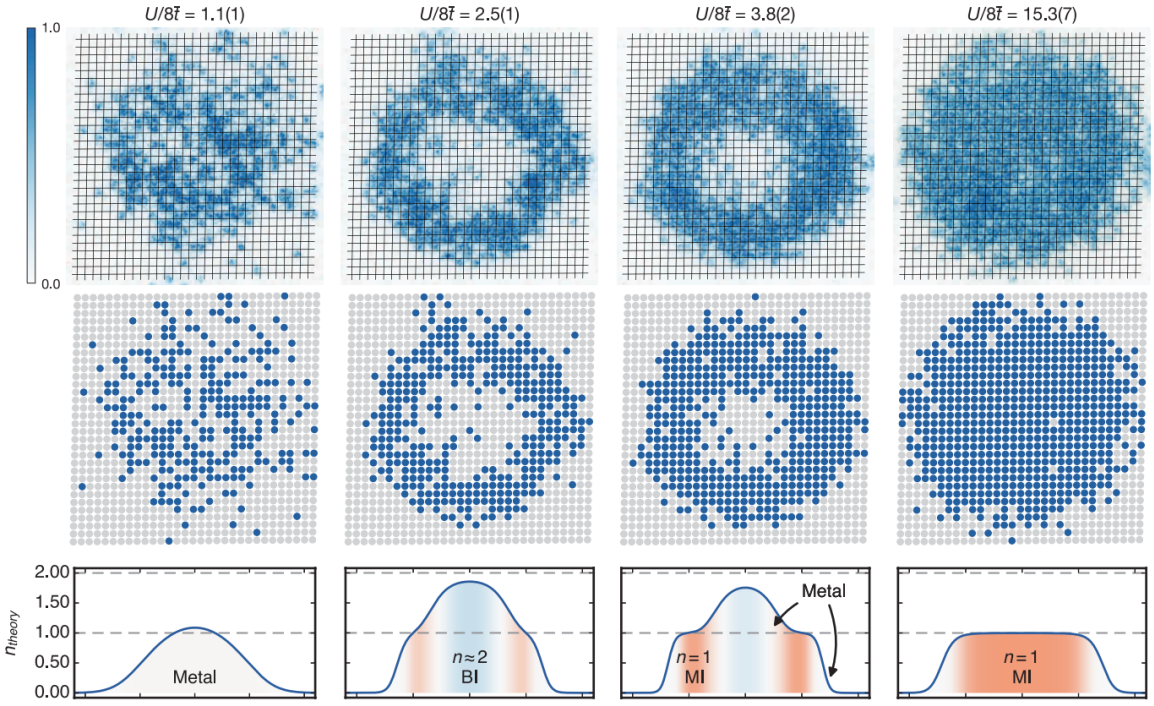


Figure 62: Site-resolved imaging of a two-dimensional Fermi-Hubbard system for increasing interactions $U/8J$ (the tunneling is denoted $\bar{t}$ in the figure). Top: raw fluorescence images. Middle: reconstructed parity-projected occupations. Bottom: density profiles predicted by theory, showing metallic (M), band-insulating (BI) and Mott-insulating (MI) regions. Doubly-occupied sites appear empty because of parity projection. Figure taken from Ref. [61].

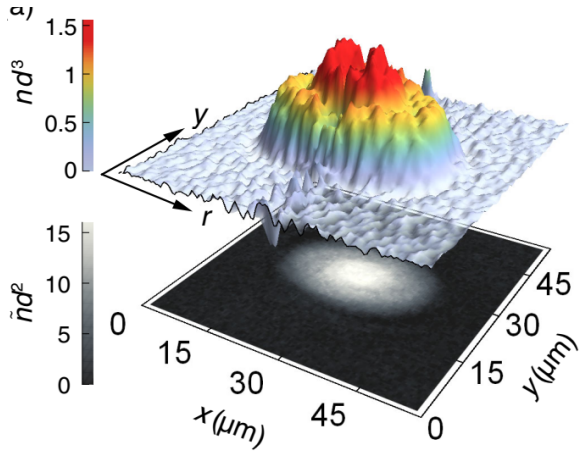


Figure 63: Density distribution of an SU(N) Fermi gas of ^{173}Yb atoms in a three-dimensional optical lattice. Bottom: measured column density $\tilde{n}$. Top: three-dimensional density n reconstructed by an inverse Abel transform, in units of the lattice site volume d^3. Figure taken from Ref. [64].

^{173}Yb, with $I = 5/2$, and $N = 10$ for ^{87}Sr). Since the nuclear spin is decoupled from the electrons, the scattering length does not depend on the nuclear spin states, and the interactions are invariant under any unitary transformation among the N spin states. The Hubbard model then acquires an SU(N) symmetry, which generalizes the SU(2) spin-rotation symmetry of spin-1/2 fermions [62].

A Mott insulator with one atom per site can be formed for any N. In the paramagnetic regime, each site carries a spin entropy $k_B \ln N$, larger than for spin-1/2 fermions. This property allows one to reach lower temperatures by adiabatically loading the atoms into the lattice: at fixed total entropy, entropy is transferred from the motional degrees of freedom to the spin degree of freedom, and the temperature decreases when the Mott insulator forms. This is analogous to Pomeranchuk cooling in ^{3}He, where the solid phase, in which nuclear spins are disordered, has a larger entropy than the liquid phase. An SU(6) Mott insulator was realized with this method [63], and the Mott crossover was characterized for various N by measuring the in-situ density distribution in a three-dimensional lattice, as shown in Fig. 63 [64].

5.4 Quantum magnetism

In a Mott insulator, the charge degree of freedom is frozen, but the spin degree of freedom remains. How do the spins order at low temperature? In the atomic limit $J = 0$ all spin configurations are degenerate, as in Fig. 64a. This degeneracy is lifted by virtual tunneling processes, which generate an effective interaction between neighbouring spins. We first derive it in a simple double-well model, and then describe experiments probing this interaction and the resulting antiferromagnetic correlations.

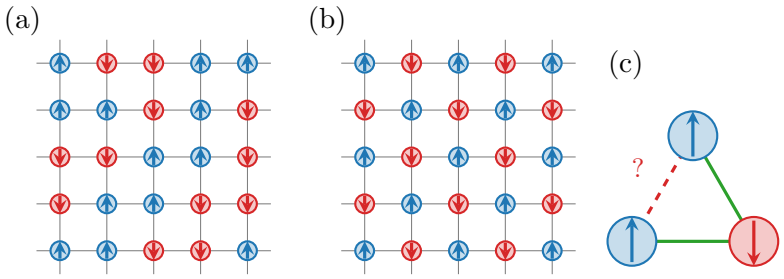


Figure 64: (a) In a Mott insulator at temperatures above the superexchange energy, the spins are disordered. (b) At low temperature, an antiferromagnetic (Néel) order develops on the square lattice. (c) On a triangular plaquette, the antiferromagnetic interactions cannot be satisfied on all bonds simultaneously (frustration).

5.4.1 Toy model: superexchange in a double well

We consider two fermions of opposite spins in a double well with sites L and R, described by the Hubbard Hamiltonian

$$\hat{H} = -J \sum_{\sigma} \left(\hat{a}^\dagger_{L,\sigma} \hat{a}_{R,\sigma} + \hat{a}^\dagger_{R,\sigma} \hat{a}_{L,\sigma} \right) + U \left(\hat{n}_{L\uparrow} \hat{n}_{L\downarrow} + \hat{n}_{R\uparrow} \hat{n}_{R\downarrow} \right). \tag{5.14}$$

With one fermion of each spin, the Hilbert space is spanned by four states, which we define with a fixed ordering of the creation operators:

$$\begin{aligned} |\uparrow\downarrow, \emptyset\rangle &= \hat{a}^\dagger_{L\uparrow} \hat{a}^\dagger_{L\downarrow} |0\rangle, & |\emptyset, \uparrow\downarrow\rangle &= \hat{a}^\dagger_{R\uparrow} \hat{a}^\dagger_{R\downarrow} |0\rangle, \\ |\uparrow, \downarrow\rangle &= \hat{a}^\dagger_{L\uparrow} \hat{a}^\dagger_{R\downarrow} |0\rangle, & |\downarrow, \uparrow\rangle &= \hat{a}^\dagger_{L\downarrow} \hat{a}^\dagger_{R\uparrow} |0\rangle. \end{aligned} \tag{5.15}$$

The two first states contain a doubly-occupied site, the two last ones one fermion per site.

Matrix of the Hamiltonian. The action of the tunneling operator is computed with the anticommutation relations. For instance,

$$\hat{a}^\dagger_{L\downarrow} \hat{a}_{R\downarrow}\, \hat{a}^\dagger_{L\uparrow} \hat{a}^\dagger_{R\downarrow} |0\rangle = -\hat{a}^\dagger_{L\downarrow} \hat{a}^\dagger_{L\uparrow} |0\rangle = +|\uparrow\downarrow, \emptyset\rangle, \tag{5.16}$$

$$\hat{a}^\dagger_{L\uparrow} \hat{a}_{R\uparrow}\, \hat{a}^\dagger_{L\downarrow} \hat{a}^\dagger_{R\uparrow} |0\rangle = -\hat{a}^\dagger_{L\uparrow} \hat{a}^\dagger_{L\downarrow} |0\rangle = -|\uparrow\downarrow, \emptyset\rangle, \tag{5.17}$$

and similarly for the transfer to the right site. In the basis $\{|\uparrow\downarrow, \emptyset\rangle, |\emptyset, \uparrow\downarrow\rangle, |\uparrow, \downarrow\rangle, |\downarrow, \uparrow\rangle\}$, the Hamiltonian then reads

$$\hat{H} = \begin{pmatrix} U & 0 & -J & J \\ 0 & U & -J & J \\ -J & -J & 0 & 0 \\ J & J & 0 & 0 \end{pmatrix}. \tag{5.18}$$

The opposite signs of the couplings of $|\uparrow, \downarrow\rangle$ and $|\downarrow, \uparrow\rangle$ to the doubly-occupied states are a direct consequence of the fermionic statistics. For bosons, all four couplings would have the same sign, which leads to very different magnetic properties, as discussed below.

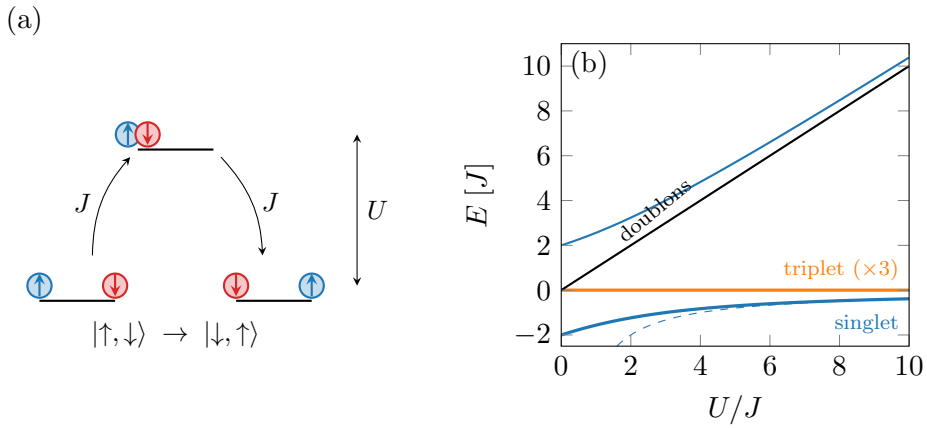


Figure 65: (a) Superexchange mechanism: the configuration $|\uparrow,\downarrow\rangle$ is coupled to $|\downarrow,\uparrow\rangle$ via a virtual doubly-occupied state of energy U. (b) Exact spectrum of two fermions of opposite spins in a double well as a function of U/J. The singlet ground state (thick blue line) is lowered below the triplet states (orange line, energy 0) by the superexchange energy $J_{\rm ex} \simeq 4J^2/U$ (dashed line: $-4J^2/U$). The upper levels correspond to doubly-occupied states.

Exact spectrum. The Hamiltonian is block diagonal in the basis of the spin singlet and triplet states

$$|s\rangle = \frac{|\uparrow,\downarrow\rangle - |\downarrow,\uparrow\rangle}{\sqrt{2}}, \qquad |t_0\rangle = \frac{|\uparrow,\downarrow\rangle + |\downarrow,\uparrow\rangle}{\sqrt{2}}, \tag{5.19}$$

and of the symmetric and antisymmetric doublon states $|D_\pm\rangle = (|\uparrow\downarrow,\emptyset\rangle \pm |\emptyset,\uparrow\downarrow\rangle)/\sqrt{2}$. One finds $\hat{H}|t_0\rangle = 0$ and $\hat{H}|D_-\rangle = U|D_-\rangle$: the triplet state does not couple to doubly-occupied states, since two fermions in a symmetric spin state must be in an antisymmetric orbital state, which excludes double occupancy (Pauli blocking). The same holds for the two other triplet states $\hat{a}^\dagger_{L\uparrow}\hat{a}^\dagger_{R\uparrow}|0\rangle$ and $\hat{a}^\dagger_{L\downarrow}\hat{a}^\dagger_{R\downarrow}|0\rangle$, which have zero energy. On the contrary, the singlet couples to $|D_+\rangle$, with $\hat{H}|s\rangle = -2J|D_+\rangle$, and the 2×2 block

$$\begin{pmatrix} 0 & -2J \\ -2J & U \end{pmatrix} \tag{5.20}$$

has the eigenvalues

$$E_\pm = \frac{U}{2} \pm \sqrt{\frac{U^2}{4} + 4J^2}. \tag{5.21}$$

The ground state is thus a spin singlet, with an energy E_- that tends to $-4J^2/U$ for $U \gg J$. The full spectrum is shown in Fig. 65.

Effective spin Hamiltonian. In the limit $J \ll U$, the low-energy dynamics takes place in the subspace $\mathcal{E}_0$ spanned by the states with one fermion per site, separated by an energy gap U from the doubly-occupied states. We describe it by an effective Hamiltonian obtained by degenerate perturbation theory. Denoting $\hat{P}$ the projector on

$\mathcal{E}_0$, $\hat{Q} = 1 - \hat{P}$, and $\hat{T}$ the tunneling operator, the first-order term vanishes, $\hat{P}\hat{T}\hat{P} = 0$, and the second-order term reads

$$\hat{H}_{\rm mag} = \hat{P}\hat{T}\hat{Q}\,\frac{1}{0-U}\,\hat{Q}\hat{T}\hat{P} = -\frac{1}{U}\,\hat{P}\hat{T}\hat{Q}\hat{T}\hat{P}. \tag{5.22}$$

Using the matrix elements of (5.18), we find in the basis $\{|\uparrow,\downarrow\rangle, |\downarrow,\uparrow\rangle\}$

$$\hat{H}_{\rm mag} = \begin{pmatrix} -2J^2/U & 2J^2/U \\ 2J^2/U & -2J^2/U \end{pmatrix}. \tag{5.23}$$

The diagonal terms describe the energy lowering due to virtual hopping to the doubly-occupied states and back, and the off-diagonal terms an exchange of the two spins via the virtual doubly-occupied state (Fig. 65a). The ground state is the singlet $|s\rangle$, of energy $-4J^2/U$, while the triplet state $|t_0\rangle$ has zero energy. Their splitting defines the superexchange energy

$$J_{\rm ex} \equiv \frac{4J^2}{U}. \tag{5.24}$$

Heisenberg model. Introducing the spin-1/2 operators $\hat{\mathbf{S}}_L$ and $\hat{\mathbf{S}}_R$ of the two sites, the singlet and triplet states are eigenstates of $\hat{\mathbf{S}}_L \cdot \hat{\mathbf{S}}_R$ with eigenvalues $-3/4$ and $1/4$, respectively. The effective Hamiltonian can thus be written as

$$\hat{H}_{\rm mag} = J_{\rm ex}\left(\hat{\mathbf{S}}_L \cdot \hat{\mathbf{S}}_R - \frac{1}{4}\right), \tag{5.25}$$

an antiferromagnetic Heisenberg coupling. The same derivation on a lattice, at half filling and for $U \gg J$, leads to the antiferromagnetic Heisenberg model

$$\hat{H}_{\rm mag} = J_{\rm ex} \sum_{\langle j,j'\rangle} \hat{\mathbf{S}}_j \cdot \hat{\mathbf{S}}_{j'}, \tag{5.26}$$

up to a constant. The superexchange energy is much smaller than the tunneling amplitude, which sets a low temperature scale for magnetic phenomena: with typical values $U \simeq 10\,J$, one has $J_{\rm ex} \simeq 0.4\,J$, and for $J/h \sim 100\,$Hz, $J_{\rm ex}/h \sim 40\,$Hz, i.e. $J_{\rm ex}/k_{\rm B} \sim 2\,$nK.

For bosons in two internal states with equal interactions, the couplings of $|\uparrow,\downarrow\rangle$ and $|\downarrow,\uparrow\rangle$ to the doubly-occupied states have the same sign. The superexchange then lowers the triplet state $|t_0\rangle$ instead of the singlet. The polarized states $|\uparrow,\uparrow\rangle$ and $|\downarrow,\downarrow\rangle$ are also lowered by $4J^2/U$, since double occupancy by two bosons in the same state is allowed, so that the three triplet states remain degenerate for equal interactions. One obtains a ferromagnetic Heisenberg coupling, $J_{\rm ex} = -4J^2/U$.

5.4.2 Probing superexchange interactions

Superexchange interactions were observed directly in isolated double wells realized with an optical superlattice (see section 3), using bosonic ^{87}Rb atoms in two hyperfine states [65]. The experiment starts with an array of double wells, each containing one atom in the left well with spin $\uparrow$ and one atom in the right well with spin $\downarrow$, i.e. the state $|\uparrow,\downarrow\rangle$. This state is a superposition of the eigenstates $|t_0\rangle$ and $|s\rangle$ (for bosons, the triplet is now

the ground state), so that the system oscillates between $|\uparrow,\downarrow\rangle$ and $|\downarrow,\uparrow\rangle$ at the frequency $|J_{\rm ex}|/h$. The spin imbalance between the two wells evolves as

$$N_z(t) = -\frac{1}{2}\cos\left(\frac{J_{\rm ex}t}{\hbar}\right), \tag{5.27}$$

while the population imbalance remains zero: the atoms exchange their spins without net transfer of particles.

The readout relies on a site-resolved band-mapping technique: the double wells are deformed so that the left well is raised above the right one, the atom of the left well being transferred to an excited band of the right well (see Fig. 66). A band-mapping sequence combined with a Stern-Gerlach separation of the two spin states then gives the spin populations in each well. The measured spin imbalance oscillates while the population imbalance remains zero, as expected. Depending on the barrier height, which sets J and U/J, the oscillation frequency ranges from about 20 Hz to about 1 kHz, in agreement with the expected value of $|J_{\rm ex}|$. For moderate values of U/J, the fast oscillations superimposed on the superexchange dynamics reveal the virtual population of doubly-occupied states. The experiment also demonstrated a control of the superexchange coupling by an energy offset Δ between the two wells: the two virtual doubly-occupied states then have energies $U \pm \Delta$, and the superexchange coupling becomes $|J_{\rm ex}| = 2J^2/(U+\Delta) + 2J^2/(U-\Delta) = 4J^2U/(U^2-\Delta^2)$.

5.4.3 Short-range antiferromagnetic correlations

According to (5.26), antiferromagnetic correlations between neighbouring spins develop when the temperature becomes comparable to $J_{\rm ex}$. Short-range antiferromagnetic correlations in fermionic Mott insulators were first detected in dimerized and anisotropic lattices [66] and by Bragg scattering of light in a three-dimensional lattice [67]. Quantum gas microscopes allow a direct measurement of the spin correlations with single-site resolution.

Spin-resolved imaging. The fluorescence imaging used in quantum gas microscopes does not distinguish the spin states. To measure the spin, one spin component is removed with a resonant laser pulse before imaging (see Fig. 67), so that the image only shows the atoms of the remaining spin state. The experiment is repeated many times, removing either the $\uparrow$ or the $\downarrow$ component, or none of them.

Spin correlation function. The magnetic correlations are characterized by the connected correlation function

$$C_{\mathbf{d}} = 4\left(\langle \hat{S}^z_{\mathbf{r}+\mathbf{d}}\hat{S}^z_{\mathbf{r}}\rangle - \langle \hat{S}^z_{\mathbf{r}+\mathbf{d}}\rangle\langle \hat{S}^z_{\mathbf{r}}\rangle\right), \tag{5.28}$$

where $\hat{S}^z_{\mathbf{r}} = (\hat{n}_{\mathbf{r},\uparrow} - \hat{n}_{\mathbf{r},\downarrow})/2$, and the prefactor 4 normalizes the correlation of two perfectly correlated spins to ± 1. It can be obtained from the different types of images, using the identity

$$4\hat{S}^z_{\mathbf{r}'}\hat{S}^z_{\mathbf{r}} = 2\left(\hat{n}_{\mathbf{r}',\uparrow}\hat{n}_{\mathbf{r},\uparrow} + \hat{n}_{\mathbf{r}',\downarrow}\hat{n}_{\mathbf{r},\downarrow}\right) - \hat{n}_{\mathbf{r}'}\hat{n}_{\mathbf{r}}, \tag{5.29}$$

with $\hat{n}_{\mathbf{r}} = \hat{n}_{\mathbf{r},\uparrow} + \hat{n}_{\mathbf{r},\downarrow}$, which involves only density correlations of single spin components and of the total density.

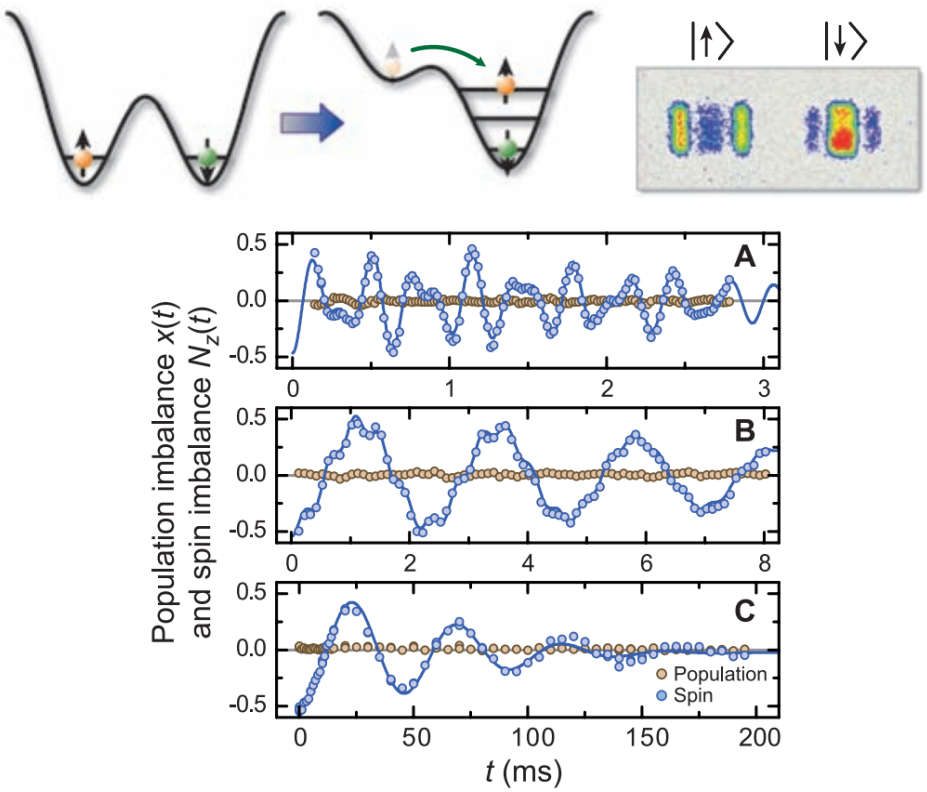


Figure 66: Observation of superexchange dynamics in double wells. Top: site-resolved detection, in which the left well is raised so that its atom is transferred to an excited band, before band mapping and Stern-Gerlach separation of the two spin states. Bottom: evolution of the population imbalance $x(t)$ and of the spin imbalance $N_z(t)$ between the two wells, for three different settings of the double wells. Figures taken from Ref. [65].

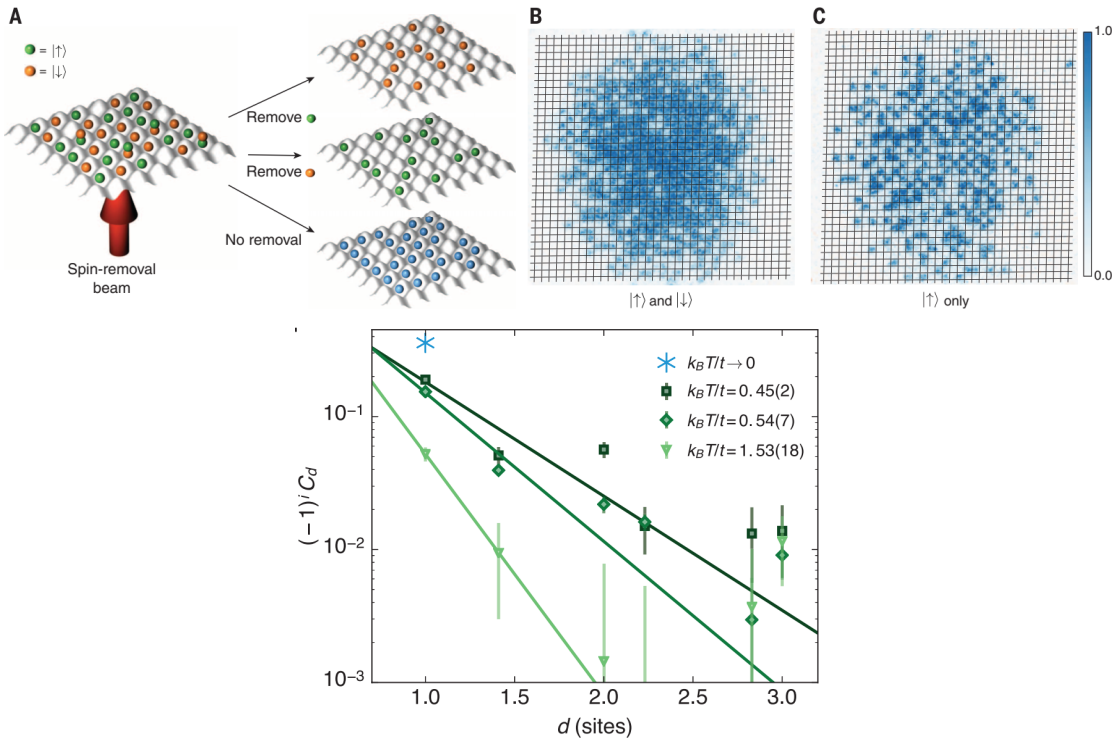


Figure 67: Spin-resolved imaging of a fermionic Mott insulator. Top: (A) one spin component can be removed before imaging; (B) image of both components; (C) image of the ↑ component only. Bottom: staggered spin correlation function $(-1)^i C_{\mathbf{d}}$ versus distance d, for different temperatures (the tunneling is denoted t in the figure). The star indicates the nearest-neighbour correlation expected at zero temperature. Figures taken from Ref. [68].

The correlation function measured in Ref. [68] with ^{6}Li atoms at half filling is shown in Fig. 67. It alternates in sign, with negative correlations between nearest neighbours and positive correlations between next-nearest neighbours, as expected for antiferromagnetic correlations. The staggered correlation $(-1)^i C_{\mathbf{d}}$ (where $(-1)^i = \pm 1$ depending on the sublattice of $\mathbf{d}$) decays exponentially with the distance, with a correlation length of the order of the lattice spacing at the temperatures $k_{\mathrm{B}}T \simeq 0.5\,J$ reached in this experiment. The nearest-neighbour correlation is about half of its zero-temperature value, indicated by the star.

5.4.4 Potential shaping to 'remove' entropy

Observing long-range antiferromagnetic order requires an entropy per particle well below the spin entropy $k_{\mathrm{B}} \ln 2$ of the paramagnetic Mott insulator. Since evaporative cooling cannot be performed efficiently in the lattice, one can instead redistribute the entropy within the cloud. In a trapped system, the low-density metallic regions at the edges of the cloud have a large density of low-energy states and can store most of the entropy, acting as a reservoir, while the central region reaches a much lower entropy per particle.

This idea was pushed further in Ref. [69] by shaping the trapping potential with a digital micromirror device (DMD) projecting a repulsive optical potential. A dimple

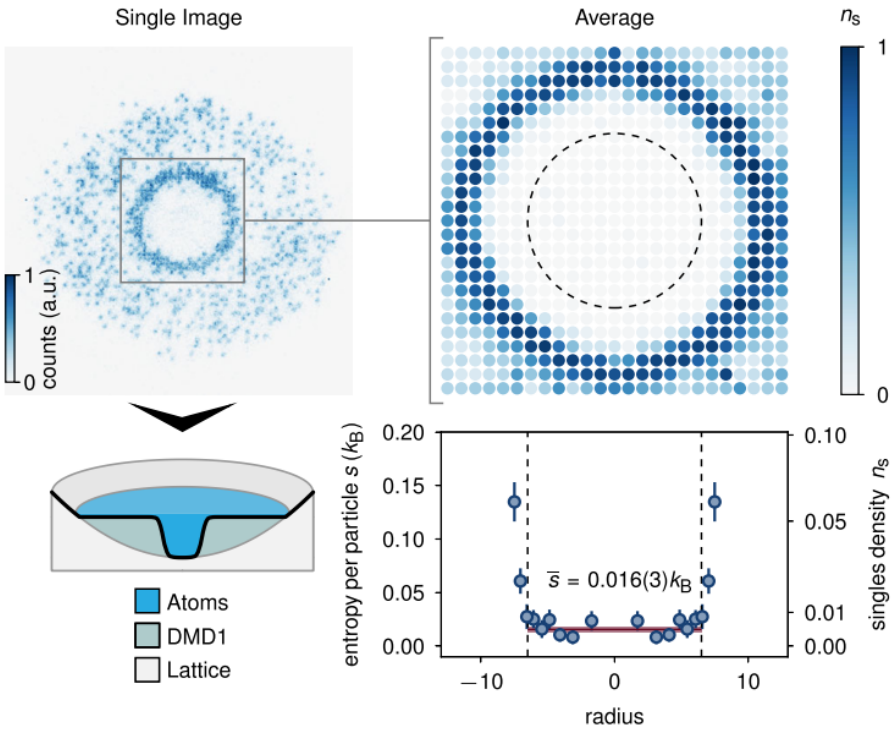


Figure 68: Potential shaping to reduce the entropy of a Hubbard system. A central dimple, created by a DMD on top of the lattice and harmonic potentials, is filled with a band insulator (which appears empty in parity-projected images, i.e. with a low density n_s of singly-occupied sites), surrounded by a metallic reservoir. Bottom right: entropy per particle measured across the central region. Figure taken from Ref. [69].

created in the center of the cloud is filled with a band insulator, while the surrounding atoms form a metallic reservoir that absorbs the entropy. The entropy per particle measured in the band insulator was as low as $0.016(3)\,k_B$ (see Fig. 68). Such a low-entropy state can then serve as a starting point to engineer other low-entropy many-body states, for instance by adiabatically changing the potential.

5.4.5 Observation of a long-range antiferromagnet

Combining these techniques (a flat-bottom potential shaped with a DMD and an entropy reservoir), a two-dimensional antiferromagnet with correlations extending over the whole system was observed in Ref. [70], see Fig. 69. Spin-resolved images (after removal of one spin component) reveal a checkerboard pattern, and the spin correlation map exhibits an alternating pattern extending to the edges of the system, of about 80 sites. The staggered correlation function decays rapidly over the first sites, and then remains finite up to the largest distances.

In two dimensions, the Mermin-Wagner theorem forbids true long-range order at non-zero temperature for the Heisenberg model, which has a continuous symmetry. However, the correlation length of the two-dimensional antiferromagnet grows exponentially when the temperature decreases below J_{ex}, and quickly exceeds the size of the system: for finite systems, the antiferromagnetic correlations then extend over the whole sample.

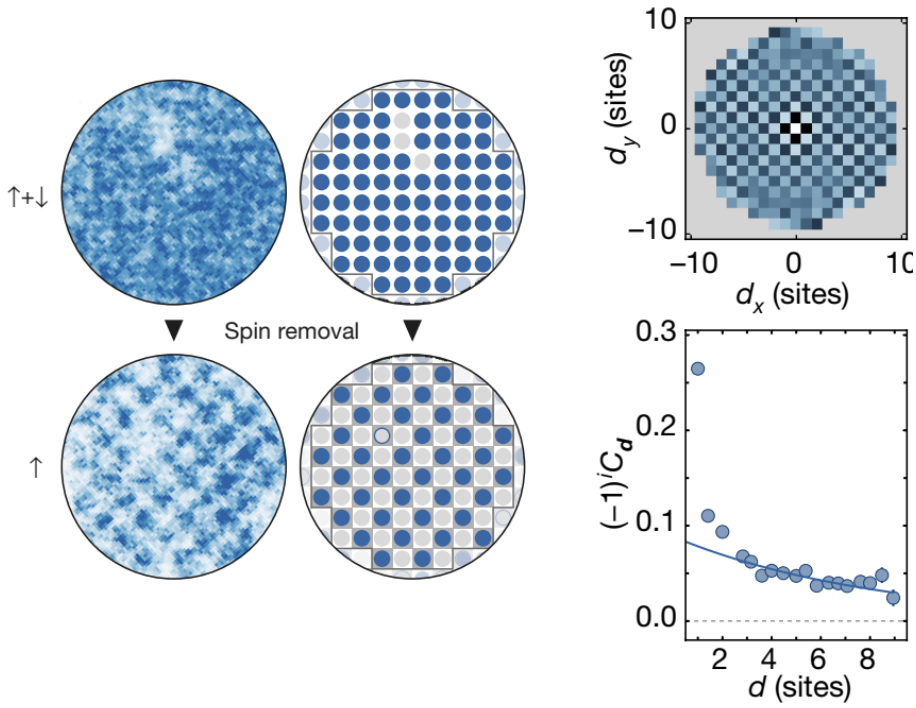


Figure 69: Observation of a long-range antiferromagnet. Left: single-shot images of the total density (top) and of the ↑ component only (bottom), raw and reconstructed. Top right: spin correlation map $C_{\mathbf{d}}$ as a function of $\mathbf{d} = (d_x, d_y)$. Bottom right: staggered correlation function versus distance. Figure taken from Ref. [70].

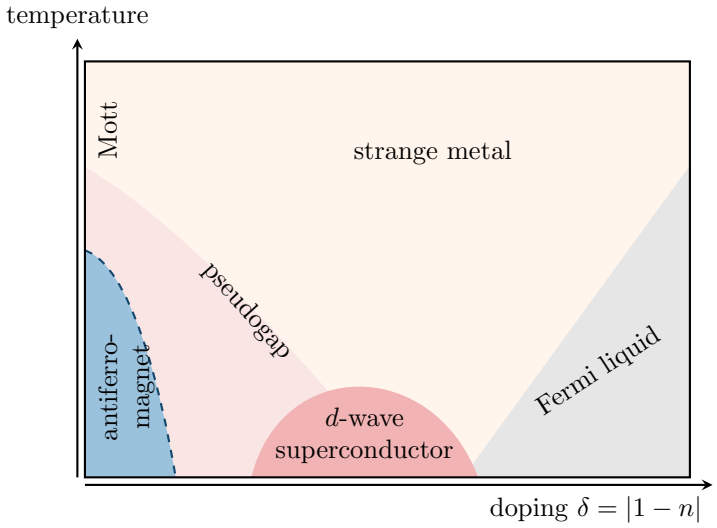


Figure 70: Schematic phase diagram expected for the two-dimensional repulsive Fermi-Hubbard model as a function of doping and temperature, inspired by the phase diagram of cuprate superconductors. The antiferromagnetic Mott insulator at half filling ($\delta = 0$) has been observed with ultracold atoms, while the existence of d-wave superconductivity remains an open question.

5.4.6 Expected phase diagram

The antiferromagnetic Mott insulator observed at half filling is the starting point of the rich phase diagram of the two-dimensional repulsive Hubbard model as a function of doping $\delta = |1 - n|$, sketched in Fig. 70. This phase diagram is expected to resemble the one of cuprate superconductors, which consist of weakly coupled CuO_2 planes. When doping the antiferromagnet, the motion of the added holes (or particles) frustrates the antiferromagnetic order, which disappears at a small doping. At larger doping, the system is expected to become a Fermi liquid. Intermediate dopings host a pseudogap phase and a strange metal, whose properties are poorly understood, and possibly a superconducting phase with d-wave symmetry of the order parameter. The existence of a d-wave superfluid in the Hubbard model itself is a major open question, related to the understanding of high-T_c superconductivity [71], which cold-atom quantum simulators aim to address.

5.4.7 Quantum magnetism with frustration

In the square lattice, the classical Néel configuration minimizes the energy of every bond simultaneously. This is not possible in lattices containing loops with an odd number of sites, such as the triangular or kagome lattices. As illustrated in Fig. 64c, on a triangle, once two spins are antiparallel, the third one cannot be antiparallel to both: at least one bond is 'frustrated'. In the classical Heisenberg model, the energy of a triangle $J_{\text{ex}}(\mathbf{S}_1 \cdot \mathbf{S}_2 + \mathbf{S}_2 \cdot \mathbf{S}_3 + \mathbf{S}_3 \cdot \mathbf{S}_1) = \frac{J_{\text{ex}}}{2}[(\mathbf{S}_1 + \mathbf{S}_2 + \mathbf{S}_3)^2 - 3S^2]$ is minimized by any configuration with $\mathbf{S}_1 + \mathbf{S}_2 + \mathbf{S}_3 = \mathbf{0}$, i.e. three coplanar spins at 120°, a compromise in which no bond is fully satisfied.

In strongly frustrated lattices, such as the kagome lattice, a massive degeneracy of

classical ground states remains. Quantum fluctuations can then select complex ground states without magnetic order, such as resonating valence bond states or quantum spin liquids, characterized by long-range entanglement and fractionalized excitations [71, 72]. The realization of frustrated lattices with fermionic Mott insulators is a promising direction for cold-atom quantum simulation.

References

[1] W. S. Bakr, J. I. Gillen, A. Peng, S. Fölling, and M. Greiner. A quantum gas microscope for detecting single atoms in a Hubbard-regime optical lattice. *Nature*, 462:74, 2009.

[2] R. P. Feynman. Simulating physics with computers. *Int. J. Theor. Phys.*, 21:467, 1982.

[3] I. Bloch, J. Dalibard, and W. Zwerger. Many-body physics with ultracold gases. *Rev. Mod. Phys.*, 80:885, 2008.

[4] C. Gross and I. Bloch. Quantum simulations with ultracold atoms in optical lattices. *Science*, 357:995, 2017.

[5] A. H. Castro Neto, F. Guinea, N. M. R. Peres, K. S. Novoselov, and A. K. Geim. The electronic properties of graphene. *Rev. Mod. Phys.*, 81:109, 2009.

[6] D. Jaksch, C. Bruder, J. I. Cirac, C. W. Gardiner, and P. Zoller. Cold bosonic atoms in optical lattices. *Phys. Rev. Lett.*, 81:3108, 1998.

[7] M. Greiner, O. Mandel, T. Esslinger, T. W. Hänsch, and I. Bloch. Quantum phase transition from a superfluid to a Mott insulator in a gas of ultracold atoms. *Nature*, 415:39, 2002.

[8] B. Keimer, S. A. Kivelson, M. R. Norman, S. Uchida, and J. Zaanen. From quantum matter to high-temperature superconductivity in copper oxides. *Nature*, 518:179, 2015.

[9] R. Grimm, M. Weidemüller, and Yu. B. Ovchinnikov. Optical dipole traps for neutral atoms. *Adv. At. Mol. Opt. Phys.*, 42:95, 2000.

[10] F. Bloch. Über die Quantenmechanik der Elektronen in Kristallgittern. *Z. Phys.*, 52:555, 1929.

[11] P. L. Kapitza and P. A. M. Dirac. The reflection of electrons from standing light waves. *Proc. Cambridge Philos. Soc.*, 29:297, 1933.

[12] P. L. Gould, G. A. Ruff, and D. E. Pritchard. Diffraction of atoms by light: the near-resonant Kapitza-Dirac effect. *Phys. Rev. Lett.*, 56:827, 1986.

[13] J. Hecker Denschlag, J. E. Simsarian, H. Häffner, C. McKenzie, A. Browaeys, D. Cho, K. Helmerson, S. L. Rolston, and W. D. Phillips. A Bose-Einstein condensate in an optical lattice. *J. Phys. B*, 35:3095, 2002.

[14] M. Greiner, I. Bloch, O. Mandel, T. W. Hänsch, and T. Esslinger. Exploring phase coherence in a 2D lattice of Bose-Einstein condensates. *Phys. Rev. Lett.*, 87:160405, 2001.

[15] M. Kozuma, L. Deng, E. W. Hagley, J. Wen, R. Lutwak, K. Helmerson, S. L. Rolston, and W. D. Phillips. Coherent splitting of Bose-Einstein condensed atoms with optically induced Bragg diffraction. *Phys. Rev. Lett.*, 82:871, 1999.

[16] J. Steinhauer, R. Ozeri, N. Katz, and N. Davidson. Excitation spectrum of a Bose-Einstein condensate. *Phys. Rev. Lett.*, 88:120407, 2002.

[17] T. D. Lee, K. Huang, and C. N. Yang. Eigenvalues and eigenfunctions of a Bose system of hard spheres and its low-temperature properties. *Phys. Rev.*, 106:1135, 1957.

[18] R. Lopes, C. Eigen, N. Navon, D. Clément, R. P. Smith, and Z. Hadzibabic. Quantum depletion of a homogeneous Bose-Einstein condensate. *Phys. Rev. Lett.*, 119:190404, 2017.

[19] L. Fallani, L. De Sarlo, J. E. Lye, M. Modugno, R. Saers, C. Fort, and M. Inguscio. Observation of dynamical instability for a Bose-Einstein condensate in a moving 1D optical lattice. *Phys. Rev. Lett.*, 93:140406, 2004.

[20] M. Ben Dahan, E. Peik, J. Reichel, Y. Castin, and C. Salomon. Bloch oscillations of atoms in an optical potential. *Phys. Rev. Lett.*, 76:4508, 1996.

[21] Z. A. Geiger, K. M. Fujiwara, K. Singh, R. Senaratne, S. V. Rajagopal, M. Lipatov, T. Shimasaki, R. Driben, V. V. Konotop, T. Meier, and D. M. Weld. Observation and uses of position-space Bloch oscillations in an ultracold gas. *Phys. Rev. Lett.*, 120:213201, 2018.

[22] N. Poli, F.-Y. Wang, M. G. Tarallo, A. Alberti, M. Prevedelli, and G. M. Tino. Precision measurement of gravity with cold atoms in an optical lattice and comparison with a classical gravimeter. *Phys. Rev. Lett.*, 106:038501, 2011.

[23] L. Morel, Z. Yao, P. Cladé, and S. Guellati-Khélifa. Determination of the fine-structure constant with an accuracy of 81 parts per trillion. *Nature*, 588:61, 2020.

[24] C. Zener. Non-adiabatic crossing of energy levels. *Proc. R. Soc. Lond. A*, 137:696, 1932.

[25] B. P. Anderson and M. A. Kasevich. Macroscopic quantum interference from atomic tunnel arrays. *Science*, 282:1686, 1998.

[26] W. Kohn. Analytic properties of Bloch waves and Wannier functions. *Phys. Rev.*, 115:809, 1959.

[27] F. W. J. Olver, D. W. Lozier, R. F. Boisvert, and C. W. Clark, editors. *NIST Handbook of Mathematical Functions*. Cambridge University Press, Cambridge, 2010.

[28] W. P. Su, J. R. Schrieffer, and A. J. Heeger. Solitons in polyacetylene. *Phys. Rev. Lett.*, 42:1698, 1979.

[29] S. Trotzky, Y.-A. Chen, A. Flesch, I. P. McCulloch, U. Schollwöck, J. Eisert, and I. Bloch. Probing the relaxation towards equilibrium in an isolated strongly correlated one-dimensional Bose gas. *Nature Phys.*, 8:325, 2012.

[30] J. Zak. Berry's phase for energy bands in solids. *Phys. Rev. Lett.*, 62:2747, 1989.

[31] Di Xiao, Ming-Che Chang, and Qian Niu. Berry phase effects on electronic properties. *Rev. Mod. Phys.*, 82:1959, 2010.

[32] M. Atala, M. Aidelsburger, J. T. Barreiro, D. Abanin, T. Kitagawa, E. Demler, and I. Bloch. Direct measurement of the Zak phase in topological Bloch bands. *Nature Phys.*, 9:795, 2013.

[33] L. Tarruell, D. Greif, T. Uehlinger, G. Jotzu, and T. Esslinger. Creating, moving and merging Dirac points with a Fermi gas in a tunable honeycomb lattice. *Nature*, 483:302, 2012.

[34] D. Jaksch and P. Zoller. Creation of effective magnetic fields in optical lattices: the Hofstadter butterfly for cold neutral atoms. *New J. Phys.*, 5:56, 2003.

[35] M. Aidelsburger, M. Atala, S. Nascimbène, S. Trotzky, Y.-A. Chen, and I. Bloch. Experimental realization of strong effective magnetic fields in an optical lattice. *Phys. Rev. Lett.*, 107:255301, 2011.

[36] M. Aidelsburger, M. Atala, M. Lohse, J. T. Barreiro, B. Paredes, and I. Bloch. Realization of the Hofstadter Hamiltonian with ultracold atoms in optical lattices. *Phys. Rev. Lett.*, 111:185301, 2013.

[37] H. Miyake, G. A. Siviloglou, C. J. Kennedy, W. C. Burton, and W. Ketterle. Realizing the Harper Hamiltonian with laser-assisted tunneling in optical lattices. *Phys. Rev. Lett.*, 111:185302, 2013.

[38] D. R. Hofstadter. Energy levels and wave functions of Bloch electrons in rational and irrational magnetic fields. *Phys. Rev. B*, 14:2239, 1976.

[39] M. Aidelsburger, M. Lohse, C. Schweizer, M. Atala, J. T. Barreiro, S. Nascimbène, N. R. Cooper, I. Bloch, and N. Goldman. Measuring the Chern number of Hofstadter bands with ultracold bosonic atoms. *Nature Phys.*, 11:162, 2015.

[40] D. J. Thouless, M. Kohmoto, M. P. Nightingale, and M. den Nijs. Quantized Hall conductance in a two-dimensional periodic potential. *Phys. Rev. Lett.*, 49:405, 1982.

[41] M. P. A. Fisher, P. B. Weichman, G. Grinstein, and D. S. Fisher. Boson localization and the superfluid-insulator transition. *Phys. Rev. B*, 40:546, 1989.

[42] B. Capogrosso-Sansone, N. V. Prokof'ev, and B. V. Svistunov. Phase diagram and thermodynamics of the three-dimensional Bose-Hubbard model. *Phys. Rev. B*, 75:134302, 2007.

[43] M. Greiner. *Ultracold quantum gases in three-dimensional optical lattice potentials*. PhD thesis, Ludwig-Maximilians-Universität München, 2003.

[44] D. S. Rokhsar and B. G. Kotliar. Gutzwiller projection for bosons. *Phys. Rev. B*, 44:10328, 1991.

[45] B. Capogrosso-Sansone, Ş. G. Söyler, N. Prokof'ev, and B. Svistunov. Monte Carlo study of the two-dimensional Bose-Hubbard model. *Phys. Rev. A*, 77:015602, 2008.

[46] F. Gerbier, A. Widera, S. Fölling, O. Mandel, T. Gericke, and I. Bloch. Phase coherence of an atomic Mott insulator. *Phys. Rev. Lett.*, 95:050404, 2005.

[47] S. Trotzky, L. Pollet, F. Gerbier, U. Schnorrberger, I. Bloch, N. V. Prokof'ev, B. Svistunov, and M. Troyer. Suppression of the critical temperature for superfluidity near the Mott transition. *Nature Phys.*, 6:998, 2010.

[48] J. Mun, P. Medley, G. K. Campbell, L. G. Marcassa, D. E. Pritchard, and W. Ketterle. Phase diagram for a Bose-Einstein condensate moving in an optical lattice. *Phys. Rev. Lett.*, 99:150604, 2007.

[49] E. Altman, A. Polkovnikov, E. Demler, B. I. Halperin, and M. D. Lukin. Superfluid-insulator transition in a moving system of interacting bosons. *Phys. Rev. Lett.*, 95:020402, 2005.

[50] S. Fölling, A. Widera, T. Müller, F. Gerbier, and I. Bloch. Formation of spatial shell structure in the superfluid to Mott insulator transition. *Phys. Rev. Lett.*, 97:060403, 2006.

[51] G. K. Campbell, J. Mun, M. Boyd, P. Medley, A. E. Leanhardt, L. G. Marcassa, D. E. Pritchard, and W. Ketterle. Imaging the Mott insulator shells by using atomic clock shifts. *Science*, 313:649, 2006.

[52] J. F. Sherson, C. Weitenberg, M. Endres, M. Cheneau, I. Bloch, and S. Kuhr. Single-atom-resolved fluorescence imaging of an atomic Mott insulator. *Nature*, 467:68, 2010.

[53] W. S. Bakr, A. Peng, M. E. Tai, R. Ma, J. Simon, J. I. Gillen, S. Fölling, L. Pollet, and M. Greiner. Probing the superfluid-to-Mott insulator transition at the single-atom level. *Science*, 329:547, 2010.

[54] M. Endres, M. Cheneau, T. Fukuhara, C. Weitenberg, P. Schauß, C. Gross, L. Mazza, M. C. Bañuls, L. Pollet, I. Bloch, and S. Kuhr. Observation of correlated particle-hole pairs and string order in low-dimensional Mott insulators. *Science*, 334:200, 2011.

[55] E. Altman and A. Auerbach. Oscillating superfluidity of bosons in optical lattices. *Phys. Rev. Lett.*, 89:250404, 2002.

[56] M. Endres, T. Fukuhara, D. Pekker, M. Cheneau, P. Schauß, C. Gross, E. Demler, S. Kuhr, and I. Bloch. The 'Higgs' amplitude mode at the two-dimensional superfluid/Mott insulator transition. *Nature*, 487:454, 2012.

[57] J. Hubbard. Electron correlations in narrow energy bands. *Proc. R. Soc. Lond. A*, 276:238, 1963.

[58] D. Mitra, P. T. Brown, E. Guardado-Sanchez, S. S. Kondov, T. Devakul, D. A. Huse, P. Schauß, and W. S. Bakr. Quantum gas microscopy of an attractive Fermi-Hubbard system. *Nature Phys.*, 14:173, 2018.

[59] R. Jördens, N. Strohmaier, K. Günter, H. Moritz, and T. Esslinger. A Mott insulator of fermionic atoms in an optical lattice. *Nature*, 455:204, 2008.

[60] U. Schneider, L. Hackermüller, S. Will, Th. Best, I. Bloch, T. A. Costi, R. W. Helmes, D. Rasch, and A. Rosch. Metallic and insulating phases of repulsively interacting fermions in a 3D optical lattice. *Science*, 322:1520, 2008.

[61] D. Greif, M. F. Parsons, A. Mazurenko, C. S. Chiu, S. Blatt, F. Huber, G. Ji, and M. Greiner. Site-resolved imaging of a fermionic Mott insulator. *Science*, 351:953, 2016.

[62] A. V. Gorshkov, M. Hermele, V. Gurarie, C. Xu, P. S. Julienne, J. Ye, P. Zoller, E. Demler, M. D. Lukin, and A. M. Rey. Two-orbital SU(N) magnetism with ultracold alkaline-earth atoms. *Nature Phys.*, 6:289, 2010.

[63] S. Taie, R. Yamazaki, S. Sugawa, and Y. Takahashi. An SU(6) Mott insulator of an atomic Fermi gas realized by large-spin Pomeranchuk cooling. *Nature Phys.*, 8:825, 2012.

[64] C. Hofrichter, L. Riegger, F. Scazza, M. Höfer, D. R. Fernandes, I. Bloch, and S. Fölling. Direct probing of the Mott crossover in the SU(N) Fermi-Hubbard model. *Phys. Rev. X*, 6:021030, 2016.

[65] S. Trotzky, P. Cheinet, S. Fölling, M. Feld, U. Schnorrberger, A. M. Rey, A. Polkovnikov, E. A. Demler, M. D. Lukin, and I. Bloch. Time-resolved observation and control of superexchange interactions with ultracold atoms in optical lattices. *Science*, 319:295, 2008.

[66] D. Greif, T. Uehlinger, G. Jotzu, L. Tarruell, and T. Esslinger. Short-range quantum magnetism of ultracold fermions in an optical lattice. *Science*, 340:1307, 2013.

[67] R. A. Hart, P. M. Duarte, T.-L. Yang, X. Liu, T. Paiva, E. Khatami, R. T. Scalettar, N. Trivedi, D. A. Huse, and R. G. Hulet. Observation of antiferromagnetic correlations in the Hubbard model with ultracold atoms. *Nature*, 519:211, 2015.

[68] M. F. Parsons, A. Mazurenko, C. S. Chiu, G. Ji, D. Greif, and M. Greiner. Site-resolved measurement of the spin-correlation function in the Fermi-Hubbard model. *Science*, 353:1253, 2016.

[69] C. S. Chiu, G. Ji, A. Mazurenko, D. Greif, and M. Greiner. Quantum state engineering of a Hubbard system with ultracold fermions. *Phys. Rev. Lett.*, 120:243201, 2018.

[70] A. Mazurenko, C. S. Chiu, G. Ji, M. F. Parsons, M. Kanász-Nagy, R. Schmidt, F. Grusdt, E. Demler, D. Greif, and M. Greiner. A cold-atom Fermi-Hubbard antiferromagnet. *Nature*, 545:462, 2017.

[71] P. W. Anderson. The resonating valence bond state in La_2CuO_4 and superconductivity. *Science*, 235:1196, 1987.

[72] L. Balents. Spin liquids in frustrated magnets. *Nature*, 464:199, 2010.